Cross-plane thermal transport in graphene-based structures

by

Meng Han

A dissertation submitted to the graduate faculty

in partial fulfillment of the requirements for the degree of

DOCTOR OF PHILOSOPHY

Major: Mechanical Engineering

Program of Study Committee:
Xinwei Wang, Major Professor
Daniel Attinger
Shan Hu
Kejin Wang
Yue Wu

The student author, whose presentation of the scholarship herein was approved by the program of study committee, is solely responsible for the content of this dissertation. The Graduate College will ensure this dissertation is globally accessible and will not permit alterations after a degree is conferred.

Iowa State University

Ames, Iowa

2018

TABLE OF CONTENTS

Page

LIST OF FIGURES

Page

LIST OF TABLES

Page

ACKNOWLEDGMENTS

I would like to thank my committee chair, Dr. Xinwei Wang, and my committee members, Dr. Daniel Attinger, Dr. Shan Hu, Dr. Kejin Wang, and Dr. Yue Wu, for their guidance and support throughout my research.

In addition, I would also like to thank my friends and my families. Their support from the other side of the world gives me the strength to overcome all the difficulties I encountered in my daily life and research. I also want to offer my appreciation to my colleagues and the department faculty and staff for making my time at Iowa State University a wonderful experience.

Also, the funding support from National Science Foundation (CBET1235852, CMMI1264399), Department of Energy (DENE0000671, DEEE0007686), and Iowa Energy Center (MG-16-025, OG-17-005) is gratefully acknowledged.

ABSTRACT

Thermal transport properties in graphene and graphene-based materials have been extensively studied due to the extremely high intrinsic thermal conductivity of graphene and its broad applications. However, most of the research is focused on the mass production and thermal transport improvement, while the layered structure and the corresponding large anisotropy in thermal transport are lack of attention. In this work, several graphene-based structures are investigated to uncover the energy coupling between graphene and substrate and between graphene layers. The thermal conductance induced by few-layered graphene (Gr) sandwiched between β-phase tungsten (β-W) films is first studied. Our differential method is able to distinguish the thermal conductance induced by the β-W film and the β-W/Gr interface. The β-W/Gr interface thermal conductance ($G_{W/Gr}$) features strong variation from sample to sample and has a lower-limit of 84 $MWm^{-2}K^{-1}$ at room temperature (RT). This is attributed to possible graphene structure damage and variation during graphene transfer and W sputtering. Compared to up-to-date reported graphene interface thermal conductance, the β-W/Gr interface is at the high end in terms of local energy coupling. Then the cross-plane thermal conductivity (k_c) of highly reduced and ordered graphene paper (GP) is characterized from 295 K down to 12.3 K. k_c is 6.08 ± 0.6 $Wm^{-1}K^{-1}$ at RT, close to the well-accepted value of graphite along the *c*-axis. An anisotropic specific heat model is developed to identify the specific heat that sustains heat conduction along the *c*-axis, based on the phonon propagation direction. This model predicts a *c*-axis mean free path (*c*-MFP) of 165 nm for graphite at RT, very close to the value of 146 nm from molecular dynamics (MD) modeling. For widely studied normal graphite materials, this model combined with the residual thermal reffusivity theory, predicts a structural domain size of 375 nm, close to the 404 nm grain size uncovered by transmission

electron microscopy. The *c*-MFP induced by defect in the GP sample is evaluated at 234 nm based on the low-momentum phonon scattering uncovered by the 0 K limit residual thermal reffusivity. This structural domain size significantly exceeds the graphene flake thickness (1.68~2.01 nm) in our GP, uncovering excellent *c*-direction atomic structure order. By subtracting the residual thermal reffusivity, the defect-free k_c and *c*-MFP of GP are obtained. At RT, the defect-free k_c is 9.67 $Wm^{-1}K^{-1}$ at RT, close to 11.6 $Wm^{-1}K^{-1}$ of graphite from the recent MD simulations. The thermal transport properties of partially reduced graphene paper (PRGP) and graphene oxide paper (GOP) are then studied and compared to that of GP. For PRGP, the determined k_c varies from 0.14 $Wm^{-1}K^{-1}$ at 295 K to 1.2×10^{-3} $Wm^{-1}K^{-1}$ at 12 K. For GOP, k_c decreases from 0.16 $Wm^{-1}K^{-1}$ at 295 K down to 9.6×10^{-3} $Wm^{-1}K^{-1}$ at 12.5 K. We eliminate the influence of heat capacity of different structures, and further study the thermal diffusivity (α_c) of these two structures. In contrary to k_c, α_c of PRGP increases from $(1.02 \pm 0.09) \times 10^{-7}$ m^2/s at 295 K to $(2.31 \pm 0.18) \times 10^{-7}$ m^2/s at 12 K. Such small α_c is mainly attributed to the small crystallite size (4.8 nm from XRD) in the cross-plane direction and the relatively larger interlayer spacing (3.68 Å compared with 3.35Å of GP and graphite). For GOP, α_c varies from $(1.52 \pm 0.05) \times 10^{-7}$ m^2/s at 295 K to $(2.28 \pm 0.08) \times 10^{-7}$ m^2/s at 12.5 K. The cross-plane thermal transport of GOP is attributed to the high density of functional groups between carbon layers which provide weak thermal transport tunnels across the layers. This work sheds light on the understanding and optimizing of nanostructure of graphene-based materials for desired thermal performance.

CHAPTER 1. INTRODUCTION

1.1 Phonon transport and phonon mean free path in graphene and graphite

Since its first discovery in 2004 [1], graphene has seen promising applications in devices like photodetectors [2], solar cells [3], flexible touch screen [4], sea water desalination [5] li ion battery electrode [6, 7] and thermal interface materials [8], due to its intriguing properties such as extremely high electrical [9] and thermal conductivity [10], large specific surface area [11], and large mechanical strength [12]. Understanding the mechanisms underlying these remarkable properties help broaden the applications of graphene and graphene-based materials.

Among the remarkable properties of graphene, the extremely high thermal conductivity is of great interest. In metals, thermal transport is dominated by electrons due to their larger concentration, while in dielectric materials, thermal transport is controlled by phonons induced by lattice vibrations. Especially in graphene, the strong covalent intralayer sp^2 bonding leads to high values of in-plane phonon group velocities and phonon density [13, 14]. With the honeycomb crystal lattice of graphene, the rhombic unit cell contains two atoms, which corresponds to six phonon polarization branches: longitudinal acoustic (LA) and longitudinal optical (LO) phonons, corresponding to the lattice vibrations along the wave propagation direction within the basal plane; transverse acoustic (TA) and transverse optical (TO), corresponding to the lattice vibrations perpendicular to the wave propagation direction within the basal plane; flexural transverse acoustic (ZA) and optical (ZO), corresponding to the lattice vibrations in the out-of-plane direction [15]. Figure 1.1 (a) shows the phonon dispersion of graphene [16]. The phonon group velocities of each phonon branches can be directly calculated

from the phonon dispersion relation. Further with the phonon density of state, heat capacity of each phonon branch and the corresponding intrinsic in-plane (basal plane or *a*-axis) thermal conductivity (k_a) of graphene (dominated by the acoustic phonon branches) can be calculated. Thermal transport in single layered graphene is two dimensional (2D) as there is no energy coupling apart from the basal plane. With an infinite flake size, phonons occupied in thermal transport start from zero frequency up to the cutoff frequency, related to the Debye temperature. While with a finite lateral size, there is a size-dependent low-bound cutoff frequency, which are determined from the condition that the phonon mean free path (MFP) cannot exceed the physical size of the flakes.

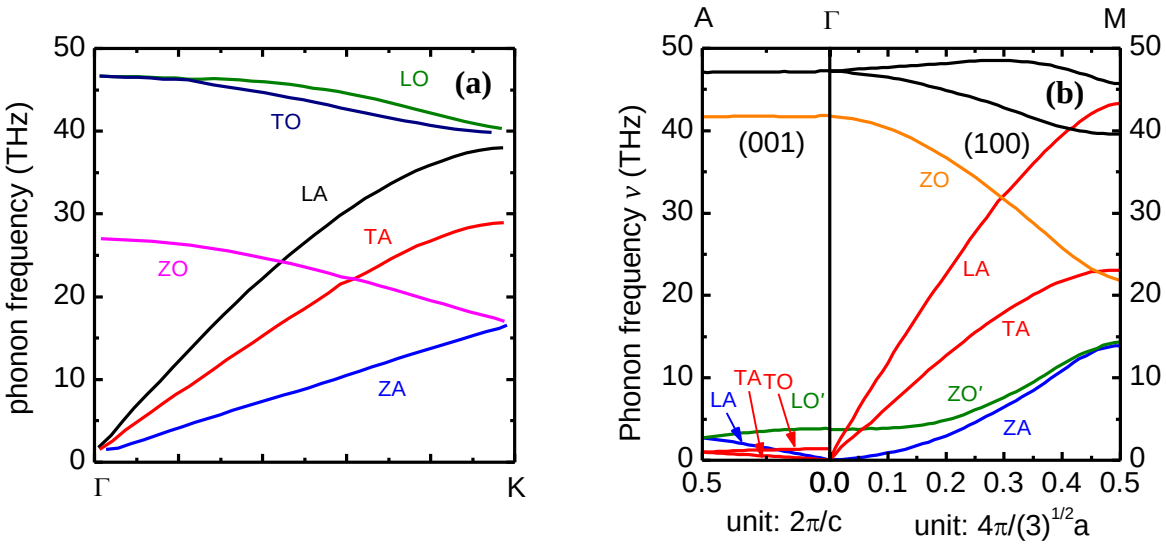

Figure 1.1 (a) Phonon dispersion of graphene calculated using the valence force model [16]. (b) phonon dispersion in graphite [17].

For graphite or few layered graphene, the unit cell contains 4 atoms from two carbon layers which corresponds to 12 phonon branches. The phonon dispersion relation has large anisotropy as shown in Fig. 1.1 (b) [17]. Not like the phonon dispersion relation of monolayer graphene, most of the phonon branches shown in the Fig. 1.1 (b) are overlaps of two branches

except for the ZA and ZO' branches, counting to the 12 phonon branches. Also, we can see that most of the phonon branches in the (001) plane (cross-plane or *c*-axis) are long-wavelength phonons due to the weak van der Walls force between monolayers. This modification of phonon energy spectrum in few layer graphene and graphite compared with that in monolayer graphene lead to the reduction of intrinsic k_a. In few layer graphene or graphite, the 2D thermal transport is valid till some low-bound cut-off frequency. But not like that in the single layer graphene which is limited by lateral size, a specific low-bound cutoff frequency (ω_{min}) comes from strong energy coupling among monolayers. Below ω_{min}, the contributions from phonons to the thermal transport in the basal plane are reduced to negligible value [15]. ω_{min} can be reasonably taken from the phonon dispersion spectrum, which is about 4 THz from the ZO' branches. That is, in other words, only low-energy phonon modes with frequency under 4 THz are occupied in thermal transport along the *c*-axis. This can also help explain the large anisotropic and much smaller *c*-axis thermal conductivity (k_c) in graphite.

Compared with the extensive investigations of k_a and *a*-axis phonon MFP (*a*-MFP) in graphene and graphite, k_c and the *c*-axis phonon MFP (*c*-MFP) are lack of attention. Direct characterization of k_c of graphite can be dated back to several decades [18, 19], leaving the underlying mechanism for the two to three orders of magnitude lower values (5.7-6.8 $Wm^{-1}K^{-1}$) than k_a not clearly uncovered [19, 20]. Early work employed a classic kinetic theory to describe the thermal transport along the *c*-axis [21]. The estimated *c*-MFP is just a few nanometers, seemingly consistent with the small value of k_c. However, several recent theoretical calculations and experimental measurements suggested that *c*-MFP can be much longer. Wei *et al*. [22] performed molecular dynamics (MD) simulations on graphite thin films

and found that k_c does not converge even when the film thickness is increased to 15 nm. Harb *et al*. [23] performed time resolved x-ray diffraction (XRD) on a graphite thin film with a thickness of 35 nm and reported a value of only 0.7 $Wm^{-1}K^{-1}$, much lower than the well-accepted value of bulk graphite. These relatively lower values of k_c indicate that the actual *c*-MFP of bulk graphite are longer than 15 nm and 35 nm. Later work by Sadeghia *et al*. [24] estimated an average *c*-MFP of 20 nm at 300 K with a theoretical calculation based on the full phonon dispersions. Recent MD simulations of Wei *et al*. [25] observed the contribution of phonons to the *c*-axis thermal transport with a long *c*-MFP in the order of hundred nanometers. Most recent experimental work by Fu *et al*. [26] measured k_c of graphite films with different thicknesses by employing the 3ω method and gave strong evidence that the average *c*-MFP at room temperature (RT) can be more than 100 nm. Similar work by Zhang *et al*. [27] conducted the time-domain thermoreflectance (TDTR) measurements on graphite films within a larger range of sample thicknesses and ambient temperatures. They found that the *c*-MFP is in the order of 100-200 nm at RT. With these progressive work, it starts to be accepted that the *c*-MFP of graphite is comparable to or not much smaller than that in the *a*-axis direction.

1.2 Interface thermal resistance induced by few-layered graphene

In the last decades, different approaches have been used to characterize the thermal transport properties of graphene. The first experimental approach was made at the University of California Riverside through development of the optothermal Raman measurement technique [10, 16, 28, 29]. The extracted k_a varies in a large range and can be as high as 5000 $Wm^{-1}K^{-1}$ at RT [10]. This value exceeds that of bulk graphite in the in-plane direction (~2000 $Wm^{-1}K^{-1}$ at RT) [30]. Following experimental work reported values ranging from hundreds to thousands of $Wm^{-1}K^{-1}$ [31-33]. The large discrepancy among these experimental results is

attributed to many factors including the sample lateral size, the defect level, the grain size and orientation and the strain distributions, *etc*.

Despite the large k_a of graphene, interface thermal resistance (R) or conductance (G) induced by graphene is another key parameter that suppress heat dissipation from graphene to the substrate in its applications. Early work by Freitage *et al*. [34] characterized the heat dissipation from graphene to substrate for the first time, but didn't explore graphene-substrate interface thermal resistance. Following work by Chen *et al*. [35] employed the differential 3ω method on the graphene (Gr)/SiO_2 interface and reported a R range from 5.6×10^{-9} to 1.2×10^{-8} Km^2W^{-1} at RT. Mak *et al*. [36] employed the ultrafast pump-probe method and obtained a G of the single-layered and multilayered Gr/SiO_2 interface varying from 2000 to 11000 $Wcm^{-2}K^{-1}$. Koh *et al.* [37] performed the TDTR measurement on the Au/Ti/Gr/SiO_2 and Au/Ti/SiO_2 sandwiches (graphene layers $1\leq n\leq10$) and reported a G of ~25 $MWm^{-2}K^{-1}$ at RT for the Au/Ti/Gr/SiO_2 interface. Similarly, Guzman *et al*. [38] performed the TDTR measurements on the variable metals/single-layered Gr/SiO_2 structures and gave a G range of 15-60 $MWm^{-2}K^{-1}$. Hopkins *et al*. [39] determined the thermal boundary conductance across the Al/single-layered Gr/Si interface from the TDTR measurement and found a two-fold increase with the oxygen functionalization of the graphene.

Along with the extensive studies of metal/Gr/SiO_2 interfaces, the metal/Gr/metal interfaces with metal substrates like Cu, Pd and W started to get attraction in recent years [40, 41]. Huang *et al*. [42] performed the TDTR measurements on the Pd/transferred Gr/Pd interface and reported a G of 300 $MWm^{-2}K^{-1}$ at RT for the sample with radiofrequency (rf)

magnetron sputtering top Pd. This value is seven times larger than that with thermal evaporation top Pd (42 $MWm^{-2}K^{-1}$). The large enhancement of thermal conductance is attributed to the electronic heat transport via atomic scale pinholes formed in the graphene during the sputtering process. W, as an excellent radiation tolerance material, [43-45] is a promising containment materials in nuclear reactors. Graphene, because of its impermeability to all standard gases (including He), [46] has also been regarded as an effective material in retarding radiation damages during nuclear reaction [47]. These remarkable properties of W and graphene motivate me to fabricate the W/Gr multilayered system and study the ability of its radiation tolerance [48] and the resulting thermal transport capacity [49].

1.3 Thermal transport in paper-like graphene-based materials

In recent years, free-standing graphene-based materials like Graphene aerogel, graphene foam and graphene-based paper have also seen promising applications in the industry. Among these, graphene nanoplates or graphene-based paper such as graphene oxide paper (GOP) and reduced graphene oxide paper (rGOP) are of great interest [50, 51].

To produce GOP or rGOP, graphite oxide is first prepared from graphite by using the modified Hummer's Method [52, 53]. Then a suspension of graphene oxide (GO) sheets is obtained by sonication of the prepared graphite oxide [51]. Due to the oxidation functional groups like hydroxyl, epoxy, and carboxyl, [54, 55] GO can be steady dispersed in water with PH higher than 9, which make the mass production less cost and much easier. GOP is assembled from GO dispersion, typically in a direct flow with a vacuum membrane filter [56, 57] or by self-assembling at the liquid air interfaces by heating to a higher temperature [58, 59]. The obtained GOP are reduced to get rGOP, typically through chemical reduction [60, 61]

or thermal reduction [62, 63]. In chemical reduction, the reduction level depends on the chemical identity and concentration of the reductants [54, 64, 65]. While in thermal reduction, the reduction level is dominated by the annealing temperature and the ambient atmosphere [55]. The reduction level and the future restoration of sp^2 domains determine the recovery or healing of the electrical and thermal transport capacities in the products. In GO or rGOP, the interlayer spacing varies from 3.35 Å [66] (same as high-quality graphite) to 9.5 Å [67]. This large range of interlayer spacing is mainly attributed to the different levels of residual functional groups in the basal plane [54].

In GOP and rGOP, the thermal transport properties also vary in a large range, due to the structure differences upon different reduction and restoration levels. Highly reduced and ordered graphene paper (GP) can reach a thermal conductivity of 1000 $Wm^{-1}K^{-1}$ [62] and an electrical conductivity of 1.57×10^5 Sm^{-1} [63] at RT, much larger than those of other graphene-based materials. To better understand the relations between thermal transport properties and the inner structure of GP, many approaches have been made. Xin *et al*. [63] reported the fabrication of GP by direct electro-spray of graphene films with a continuous roll-to-roll process. Then thermal annealing process was applied to remove functional groups and healing the structure defects. The reported k_a can reach 1238.3 $Wm^{-1}K^{-1}$ at RT after annealing at 2200 ^oC. Song *et al*. [62] investigated the structural evolution of a thermally reduced graphene oxide film by annealing at different temperatures. It is reported that ultrahigh k_a of 1043.5 $Wm^{-1}K^{-1}$ is obtained after annealing at 1200 ^oC and a critical temperature of 1000 ^oC is required for high improvement of k_a. Our recent work [66] reported measurements on k_a of GP from RT down

to very low temperatures. k_a shows an interesting jump from 529 $Wm^{-1}K^{-1}$ at 270K to 3013 $Wm^{-1}K^{-1}$ at 245 K, even exceeds that of graphite (~ 2000 $Wm^{-1}K^{-1}$ at RT) [30].

In contrary to the remarkable k_a of GP, partially reduced graphene paper (PRGP) often reported much smaller k_a, due to the residual oxygen-contained functional groups. Xiang *et al*. [57] prepared graphite nanoplatelet paper from exfoliated graphite nanoplatelet (GNPs) and reported a k_a of 178 $Wm^{-1}K^{-1}$ after mechanically compressed. Similarly, Wu *et al*. [68] fabricated a binder free, self-standing flexible paper from GNPs, and reported a k_a of 313 $Wm^{-1}K^{-1}$ after thermal annealing process. Yu *et al*. [69] modified the GP with alkaline earth metal ions (Mg, Ca) and reported an improvement of k_a from the 100.4 $Wm^{-1}K^{-1}$ to 147.7 $Wm^{-1}K^{-1}$ and 331.8 $Wm^{-1}K^{-1}$ for Mg and Ca modified GP, respectively. Malekpour *et al*. [70] employed an optothermal Raman technique on a set of graphene laminate with thickness from 9 to 44 μm deposited on PET and reported k_a ranges from 40 to 90 $Wm^{-1}K^{-1}$ at RT. Despite the extensive approaches to produce and characterize the thermal conductivity of GOP or rGOP, the layered structure and the corresponding large anisotropy in thermal transport are lack of attention. Recent work by Renteria *et al*. [71] characterized both k_a and k_c of prepared GOP after thermal reduction at different temperature. The results showed that after annealing at 1000 ^oC, k_a increases from 3 to 61 $Wm^{-1}K^{-1}$ at RT. k_c revealed an interesting decrease from 0.2 $Wm^{-1}K^{-1}$ to only 0.09 $Wm^{-1}K^{-1}$. The increase of k_a was attributed to the reduction of functional groups while the decrease of k_c was not clearly explained. This motivates me to investigate the behind mechanism of the anisotropy in thermal transport and its relationship with the layered structure.

CHAPTER 2. INTERFACE ENERGY COUPLING BETWEEN β-TUNGSTEN NANOFILM AND FEW-LAYERED GRAPHENE

In this chapter, we investigated the thermal conductance induced by few-layered graphene (Gr) sandwiched between β-W films of 15, 30 and 40 nm thicknesses by using the PT technique. Our differential characterization is able to distinguish the thermal conductance induced by β-W film and β-W/Gr interface. The determined thermal conductivity of β-W films is much smaller than that of α-W, which is however consistent with the large electrical resistivity of β-W. The β-W/β-W and β-W/Gr interface thermal conductance ($G_{W/W}$ and $G_{W/Gr}$) were characterized and compared by performing the PT measurement on multilayered β-W films with and without sandwiched graphene layers. The average $G_{W/W}$ is 280 MW $m^{-2}K^{-1}$. $G_{W/Gr}$ features strong variation from sample to sample and has a lower-limit of 84 MW $m^{-2}K^{-1}$, taking into consideration of the uncertainties. The relatively large $G_{W/Gr}$ and variation were attributed to possible graphene structure damage and variation during graphene transfer and tungsten sputtering process.

2.1 Sample preparation and characterization

2.1.1 Sample preparation

The β-W/Gr multilayered films are synthesized by depositing tungsten films and transferring graphene layers to the tungsten films. Monolayer graphene films are grown on 25-μm thick Cu foils (Alfa Aesar, item No. 46365) through chemical vapor deposition (CVD). The graphene transfer process is as follows. First, a PMMA (polymethyl methacrylate) layer is spin-coated on the Cu foils and covered the graphene sheet. Then, the Cu foil is etched by $FeCl_3$ solution. The remained Gr/PMMA is floated on the surface of $FeCl_3$ solution and is then cleaned by DI-water. The cleaned Gr/PMMA is transferred onto the surface of the tungsten

film which is produced in an ultra-high vacuum magnetron sputtering system (ULVAC, ACS-4000-C4) at RT. Finally, the PMMA layer is dissolved by acetone to form the contact between tungsten and graphene. Through repeating the above process, the tungsten-graphene multilayered film can be obtained. It is worth noting that in one tungsten-graphene stacking cycle, the thickness of each tungsten layer is kept the same. For convenience, in the following discussion, at the present of graphene, we name the samples with different tungsten sublayer thicknesses (which is 15, 30, 40 nm) as 'A', 'B', 'D', respectively [see Fig. 2.1 (a)]. For comparison study, a group of multilayered tungsten samples without graphene are also prepared, where the tungsten sublayers share the same thicknesses as those with graphene sandwiched. While there is no graphene, the samples are named as 'a', 'b', 'd', respectively [see Fig.2.1 (b)]. In addition, a group of single-layered tungsten samples are prepared and named as Aa, Bb and Dd [see Fig. 2.1 (c)]. In this work, A1, A2, A3 mean that the number of the cycles of tungsten-graphene system is 3, 5, 7. The lateral dimensions of all the samples are about 1 cm×1 cm and the detailed information are listed in Table 2.1. To mention that, during the sample preparation, the samples are kept in the vacuum chamber all through the several sputtering processes, which makes sure that no tungsten oxide forms between the tungsten sublayers. Even for the multi-layered tungsten/graphene films, where the samples are taken out for graphene transfer, tungsten oxide is not likely to form. As we know, tungsten belongs to inert metal which is very stable in normal environment. Anna Warren *et al*. [72] had ever placed a 1-mm-thick tungsten film in an oxygenated environment and investigated the oxidation behavior of tungsten under different temperature. It is found that the tungsten oxide was less than 1 nm even the sample was exposed to air and heated to 100 ^{o}C for hours. While during our sample preparation, the samples are immediately sent back to the vacuum chamber

for the tungsten sputtering after the graphene transfer process. The XRD patterns [see Fig. 2.2 (a)] also show that there is no tungsten oxide formed.

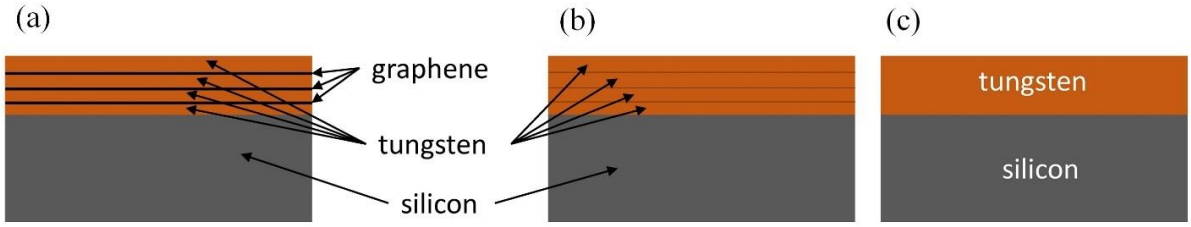

Figure 2.1 Schematic of the samples in our experiment. (a) Multilayered β-W sandwiched with graphene on 100-nm-SiO_2/Si substrate (named A, B, D). (b) Multilayered β-W on 100-nm-SiO_2/Si substrate (named a, b, d). (c) Single-layered β-W on 100-nm-SiO_2/Si substrate (named Aa, Bb, Dd).

Table 2.1 Index and geometries of all samples

Single β-W film thickness in the multilayered sample	**Multilayered β-W/Gr film**	**Multilayered β-W and the layer number**	**Single-layered β-W and the thickness**
15 nm	A1: 3×[W+G]+W	a1 (4)	Aa1 (74 nm)
	A2: 5×[W+G]+W	a2 (6)	Aa2 (110 nm)
	A3: 7×[W+G]+W	a3 (8)	Aa3 (138 nm)
30 nm	B1: 3×[W+G]+W	b1 (4)	Bb1 (128 nm)
	B2: 5×[W+G]+W	b2 (6)	Bb2 (190 nm)
	B3: 7×[W+G]+W	b3 (8)	Bb3 (247 nm)
40 nm	D1: 3×[W+G]+W	d1 (4)	Dd1 (167 nm)
	D2: 5×[W+G]+W	d2 (6)	Dd2 (252 nm)
	D3: 7×[W+G]+W	d3 (8)	Dd3 (344 nm)

"7×[W+G]" means 7 cycles of "tungsten+graphene" layer.

2.1.2 Structure characterization

The XRD technique is employed to investigate the phase, crystallite orientation and grain size of the tungsten films. In bulk tungsten, stable structure of tungsten is mainly body-centered-cubic (bcc) α-W. However, a metastable form of β-W can also appear in thin films [73-76]. The black line in Fig. 2.2 (a) shows the XRD patterns of the investigated tungsten films in a 2θ range. We can see the strongest β(200) diffraction peak of tungsten clearly, which means the sample is mostly β-W with no other crystalline or amorphous and the preferred crystalline orientation is the β(200) direction [77, 78]. The columnar structure shown in Fig. 2.3 also proves this according to the relations of microstructure and phase composition of W detailed in Shen's work [79]. The β(210), β(312) and β(400) peaks can be found in the black line but are much weaker than the β(200) peak. The blue line in Fig. 2.2 (a) shows the XRD patterns of W films coated on a stainless steel substrate by gas tunnel type plasma spraying for comparison purpose [80]. We can see that the (110) diffraction peaks of α-W is the strongest, followed by the α(211) peak and then the α(200) peak. The large difference of these two XRD patterns reveals different phase of W. The crystallite or grain size of the tungsten films is also estimated using the Scherrer equation [81] from the β(200) peak in the diffractogram, which is about 11 nm. Figure 2.2 (b) shows the schematic of the pole figure XRD measurement. This characterization is intended to determine the crystalline orientation in our samples. During this measurement, the diffraction angle (2θ) is fixed and the diffracted intensity is collected by varying two geometrical parameters, the α angle (tilt angle from sample surface normal direction) and the β angle (rotation angle around the sample surface normal direction). Figure 2.2 (c) shows the schematic of the definition of α and β angle. Figure 2.2 (d) is the pole-figure of the tungsten film, from which we can conclude that the (200) plane is parallel to the surface of the sample as the maximum pole is located in the center of the pole figure where α=0°.

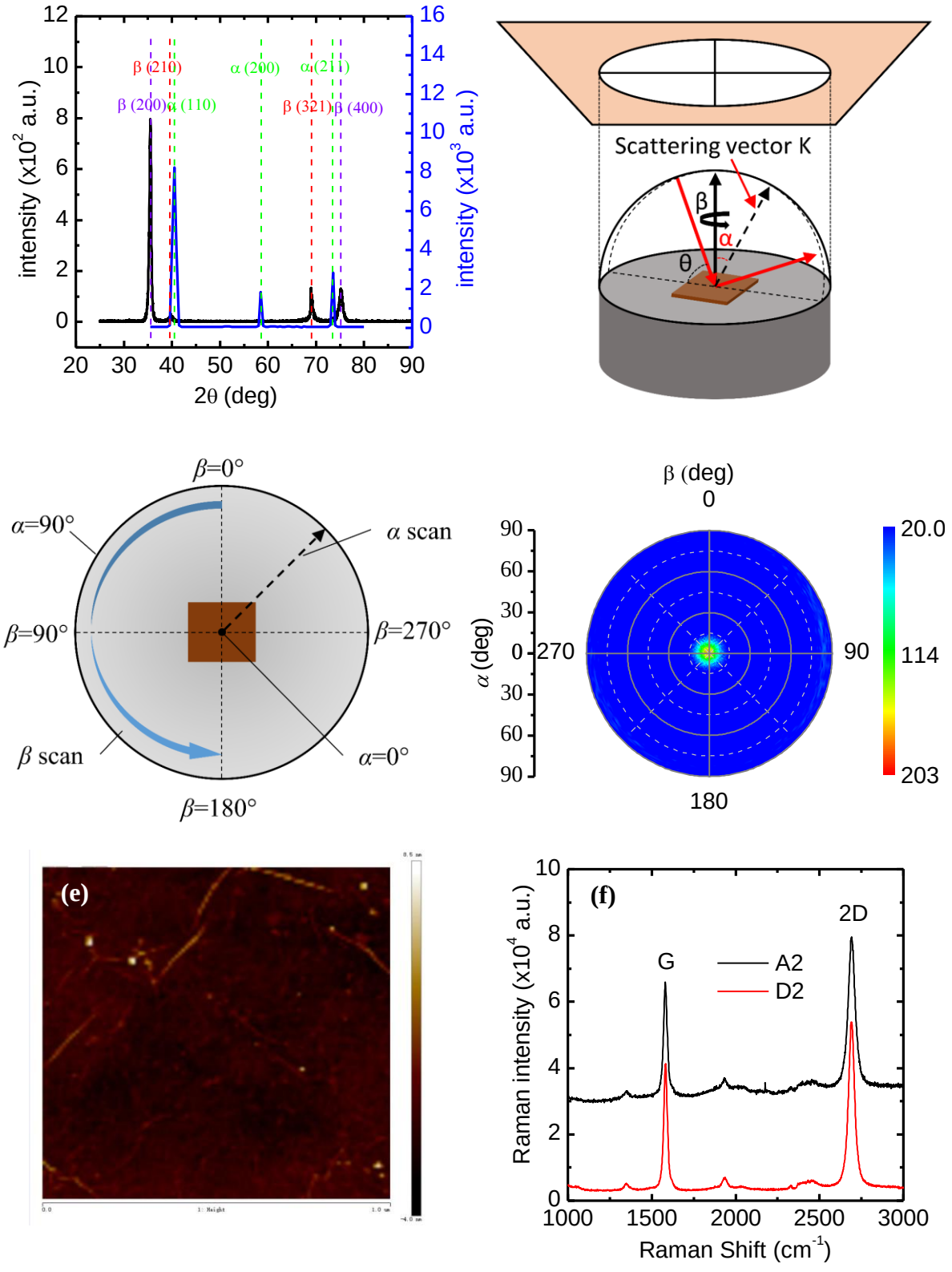

Figure 2.2 (a) XRD patterns. The black line is taken from one of our β-W films (sample Dd3: single-layered tungsten on 100-nm-SiO_2/Si substrate with a thickness of 344 nm) and the blue line is from Ref. [80], which is α-W films coated on stainless steel.

Due to the same sample preparation condition, the black line is a representative for all the samples in our experiment. This blue line serves as a comparison to show the differences of phase composition and crystal structure of tungsten films obtained under different conditions. (b) Sphere of fixed-length scattering vector and stereographic projection in pole-figure XRD. (c) Definition of α and β in the pole-figure measurement. (d) Pole-figure for sample Dd3. The maximum pole lies in the center of the pole figure, which means that β(200) plane is parallel to the sample surface. (e) AFM image of the sample surface. (f) Raman spectra of the graphene layers in the sample

Atomic force microscope (AFM) characterization is performed on the transferred graphene and the image shows kind of wrinkles in the graphene sheet while PMMA residues hardly appear [Fig. 2.2 (e)]. The structure of graphene layers is also characterized by using Raman spectroscopy. In this experiment, the Raman spectra are collected by a confocal Raman spectrometer with a spectral resolution of 1.05~1.99 cm^{-1}. A 20× objective lens is used, with an integration time of 10 s and a laser spot size of 2.01 μm. The laser energy reaching the surface of the samples is 44.7 mW. Figure 2.2 (f) shows the Raman spectra of graphene on two of our samples. The G peak and 2D peak can be seen clearly. According to the work of Graf and Molitor, [82] the ratio of the integrated intensities of the G and 2D peaks (named $I_{G/2D}$) can be used as a parameter to determine the number of layers of the graphene flake. From Fig. 2.2 (f), the G and 2D peaks for the two samples are fitted and the integrated intensities are calculated separately. The ratio of integrated intensities of the G and 2D peaks ($I_{G/2D}$) of the two samples are calculated at 0.38 and 0.42, respectively, which means the graphene used in our experiment is 1~2 layered graphene [82].

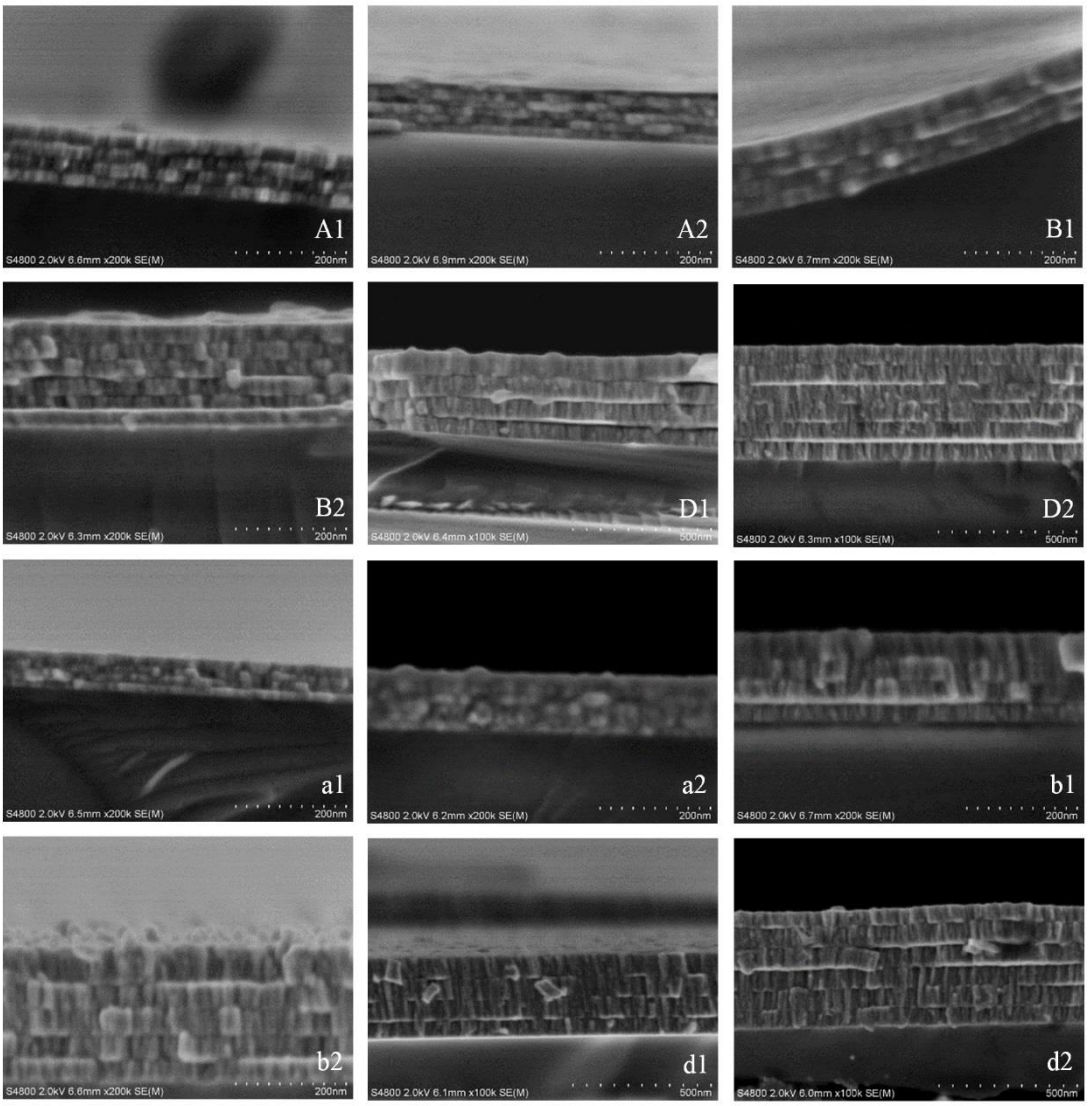

Figure 2.3 SEM image of the multilayered β-W and β-W/Gr films from which we can see the clear interface between sublayers. The layer thickness is directly measured based on the SEM image.

2.2 Experiment setup and physical model

The noncontact PT technique [83-85] is developed to characterize the thermal transport properties of a multilayer structure in the cross-plane direction. A modulated laser beam is used to irradiate the film surface which serves as a heat source and leads to a periodical temperature variation at the film surface. This temperature variation is strongly affected by the

thermal transport ability of the sample and is sensed by detecting the surface thermal radiation. As the thermal radiation are from the sample surface, we believe the detection can accurately reflect the real temperature variations of the sample surface. The phase shift of radiation to the laser beam is used to characterize the interface energy coupling properties of the samples.

Figure 2.4 (a) shows the experimental setup of the PT technique and how it is operated. A continuous infrared laser is modulated as periodic square waves by a function generator and then is directed and focused on the sample. The sample is heated to different temperatures by the laser beam under different modulation frequencies. In this experiment, the modulated laser beam is 600 mW, which assures sufficiently high radiation signal from the surface while prevents high temperature rise that may damage the sample or significantly change the sample's thermophysical properties. The laser beam has a Gaussian distribution in space and the spot size is 0.7×1.4 mm^2 in our experiment. As the dimension of the laser spot is much larger than the thermal diffusion length in the lateral direction of the sample, the Gaussian distribution has negligible influence on the measured phase shift signal. The thermal radiation signal is directed to an infrared detector which has a Ge window in front to filter out the reflection signal of the laser beam and only allows the thermal radiation signal to pass. The radiation signals are then pre-amplified and measured by a lock-in amplifier and the phase shift within a large laser frequency range is obtained for further data processing.

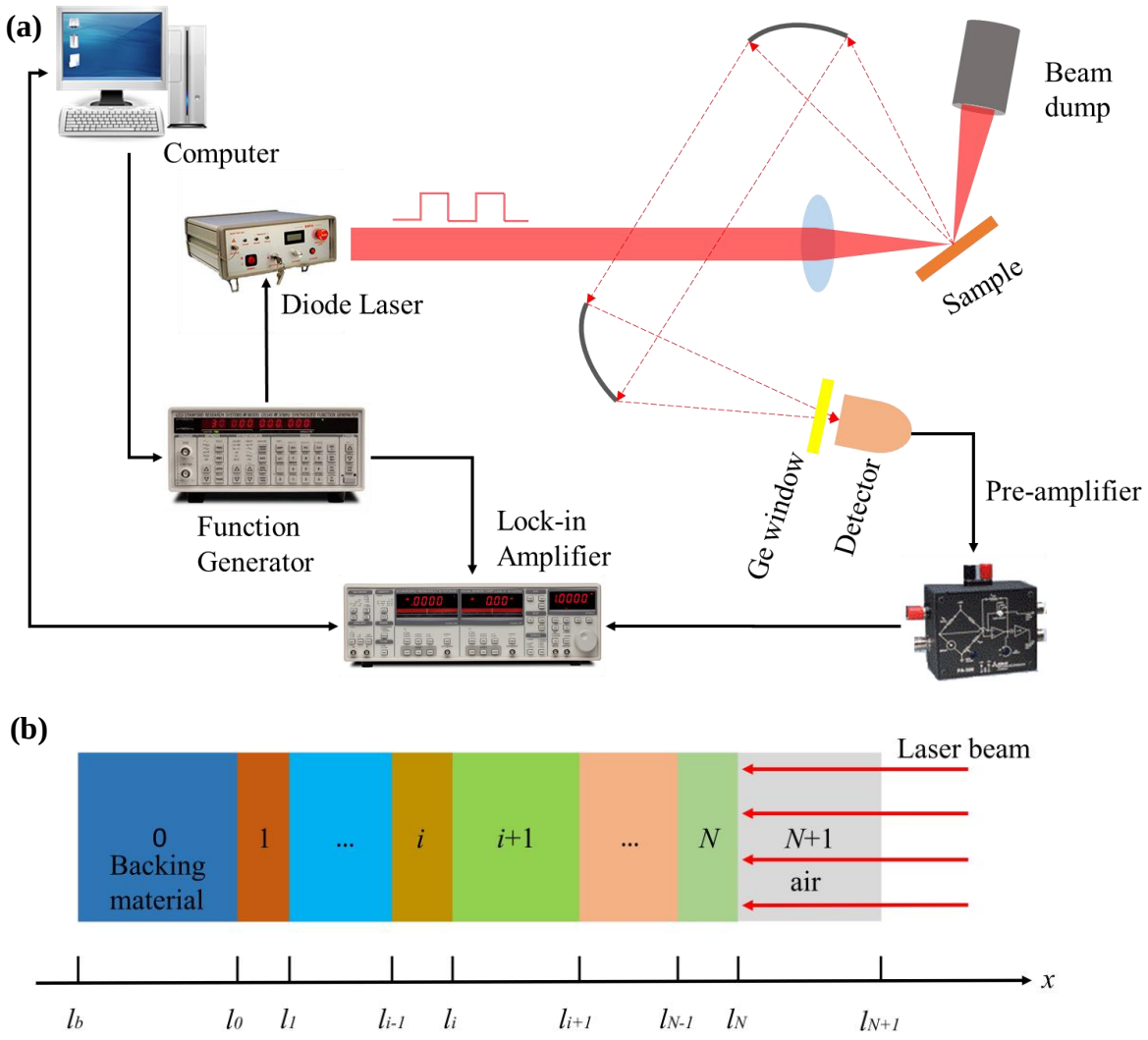

Figure 2.4 (a) Schematic of the photothermal experimental setup. (b) Schematic of an N-layer sample to show a multilayered model used in the data processing.

In this experiment, the modulation frequencies of the laser beam range from 600 Hz to 20 kHz, under which the thermal diffusion depth within one period heating is much smaller than the dimensions of the heating spot. Thus, the thermal transport process can be simplified to a one-dimensional (1D) cross-plane heat transfer model. Figure 2.4 (b) shows the cross-sectional view of the 1D multilayer model. Layers from 1 to N are the sample layers between

the substrate (layer 0) and the air (layer N+1). The governing equation for a multilayer 1D thermal conduction problem in layer *i* can be expressed as [86]:

$$\frac{\partial^2\theta_i}{\partial x^2}=\frac{1}{\alpha_i}\frac{\partial\theta_i}{\partial t}-\frac{\beta_i I_0}{2k_i}\exp\left(\sum_{m=i+1}^{N}-\beta_m L_m\right)\times e^{\beta_i(x-l_i)}\left(1+e^{j\omega t}\right). \tag{2.1}$$

Here $L_i=l_i-l_{i-1}$ is the thickness of layer *i*. Other thermophysical properties of layer *i* are thermal conductivity k_i, specific heat $c_{p,i}$ and optical absorption coefficient β_i. $\theta_i=T_i-T_{amb}$ is the temperature rise of layer *i* while T_{amb} is the ambient temperature. ω is the angular frequency ($2\pi f$). The solution to Eq. 2.1 consists of a transient component $\theta_{i,t}$, a steady DC component $\bar{\theta}_{i,s}$ and a steady AC component $\theta_{i,s}$. In this experiment, only the steady AC component $\theta_{i,s}$ is measured. The general solution to this part follows the form below:

$$\theta_{i,s}=\left[\mathrm{A}_i e^{\sigma_i(x-l_i)}+\mathrm{B}_i e^{-\sigma_i(x-l_i)}-\mathrm{E}_i e^{\beta_i(x-l_i)}\right]e^{j\omega t}. \tag{2.2}$$

In the above equation, $E_i=G_i\left(\beta_i^2-\sigma_i^2\right)$ with $G_i=\frac{\beta_i I_0}{2k_i}\exp\left(-\sum_{m=i+1}^{N}\beta_m L_m\right)$ for $i<N$, $G_N=\beta_N I_0/2k_N$, and $G_{N+1}=0$. σ_i is defined as $(1+j)\cdot a_i$ with $j=\sqrt{-1}$.

The coefficient A_i and B_i can be determined by using the interfacial conditions at $x=l_i$ as:

$$\begin{bmatrix}\mathrm{A}_i\\ \mathrm{B}_i\end{bmatrix}=U_i\begin{bmatrix}\mathrm{A}_{i+1}\\ \mathrm{B}_{i+1}\end{bmatrix}+V_i\begin{bmatrix}E_i\\ E_{i+1}\end{bmatrix}, \tag{2.3}$$

where U_i is the interfacial transmission matrix of heat and V_i is the absorption matrix of light from layer $i+1\,\text{to}\,i$ and they can be expressed as:

$$U_i=\frac{1}{2}\begin{bmatrix}u_{11,i} & u_{12,i}\\ u_{21,i} & u_{22,i}\end{bmatrix};V_i=\frac{1}{2}\begin{bmatrix}v_{11,i} & v_{12,i}\\ v_{21,i} & v_{22,i}\end{bmatrix}. \tag{2.4}$$

$$u_{1n,i} = \left(1 \pm k_{i+1}\sigma_{i+1}/k_i\sigma_i \mp k_{i+1}\sigma_{i+1}R_{i,i+1}\right) \times \exp\left[\mp\sigma_{i+1}\left(l_{i+1} - l_i\right)\right], n = 1, 2, \quad (2.5a)$$

$$u_{2n,i} = \left(1 \mp k_{i+1}\sigma_{i+1}/k_i\sigma_i \mp k_{i+1}\sigma_{i+1}R_{i,i+1}\right) \times \exp\left[\mp\sigma_{i+1}\left(l_{i+1} - l_i\right)\right], n = 1, 2, \quad (2.5b)$$

$$\nu_{n1,i} = 1 \mp \beta_i/\sigma_i, n = 1, 2\ , \quad (2.5c)$$

and $$\nu_{n2,i} = \left(-1 \mp k_{i+1}\beta_{i+1}/k_i\sigma_i \mp k_{i+1}\beta_{i+1}R_{i,i+1}\right) \times \exp\left[-\beta_{i+1}\left(l_{i+1} - l_i\right)\right], n = 1, 2\ . \quad (2.5d)$$

$R_{i,i+1}$ is the thermal contact resistance between layer i and i+1. Details of the parameters are provided in Ref. [86].

From the above solution, phase shift between the thermal radiation and the incident laser beam can be derived. Then the least square method is used to determine unknown thermophysical properties of the sample. Notice that, the optical absorption depth (τ_{opt}) is a key parameter in the PT measurement and the fitting process. In this work, τ_{opt} is taken as 22.8 nm for the β-W films. This value is larger than the thickness of top layers of several samples. The second or third layer may absorb laser energy. This has also been taken into fully consideration by given τ_{opt} of all the layers in the fitting program.

2.3 Results and discussion

2.3.1 Thermal conductivity of single-layered β-W.

The single-layered β-W films on 100-nm-SiO_2/Si substrate [see Fig. 2.1 (c)] are prepared by using the vacuum magnetron sputtering system as described before. The layer thicknesses are measured in the Digital Micrograph from the scanning electron microscopy (SEM) images. Uncertainties may come from the aspects of SEM images and the measurement operation in the Digital Micrograph.

From the physical model, we know that the phase shift is related to the physical properties of the sample such as thermal conductivity, heat capacity and density of the β-W films as well as the thermal resistance induced by the SiO_2 layer and the β-W/SiO_2 interface. Given these physical properties, the theoretical phase shift can be calculated. In the experimental measurement, we are interested in the phase shift between the thermal radiation and the modulated laser beam. However, the measurement will inevitably include time delay induced by the whole system. This time delay can be eliminated by measuring the phase shift between the reflected laser beam and the incident laser beam (noted as ϕ_{cal}). The experimental setup for the calibration process has no other difference except for detecting the reflected laser signals instead of the thermal radiation by removing the Ge window. Figure 2.5 (a) shows the phase shift of the reflected laser beam to the incident laser beam. This system phase shift shows a straight line against the modulation frequency, indicating a constant time delay of the system within the experiment frequency range. This time delay is estimated at around 1.0×10^{-6} s. The real experimental phase shift (noted as ϕ_{nor}) between the thermal radiation and the laser beam can be calculated as $\phi_{nor}=\phi_{raw}-\phi_{cal}$, with ϕ_{raw} being the raw phase shift detected in this experiment.

The fitting process is operated by using a well-developed program by our lab. With different trail values of unknown parameters, the theoretical phase shifts are calculated over the specified modulation frequency range. The value that gives the least square deviation between the theoretical phase shifts and the experimental ones is taken as the real property of materials. Here, the thermal resistance induced by the SiO_2 layer and the β-W/SiO_2 interface (noted as $R_{W/SiO_2/Si}$) and the cross-plane k of β-W films are both unknown. However, one single

measurement of the sample cannot distinguish these two properties. What we can get from the fitting of one sample measurement is the total thermal resistance (R_{total}) of the sample, which includes both the thermal resistance induced by the β-W film and $R_{W/SiO_2/Si}$. Then we measure samples of different thickness that are synthesized under the exact same conditions to vary the effect of thermal resistance of the β-W film. By studying how R_{total} varies with the W film thickness (L), k of β-W film and $R_{W/SiO_2/Si}$ can be distinguished and determined.

Figure 2.5 (b) shows the fitting result for sample Aa2 to demonstrate the fitting agreement extension. This is a β-W film of 110 nm thickness. Excellent agreement is observed between the fitting (green line) and experimental data (black circles) at all the modulation frequencies with a fitting residue of 0.30 degree. R_{total} is determined to be 2.02×10^{-7} Km^2W^{-1} for this sample. When R_{total} is taken as 1.93×10^{-7} Km^2W^{-1} and 2.10×10^{-7} Km^2W^{-1}, the fitting residue is 0.53 and 0.51, respectively, which are much larger than the experimental uncertainty of the phase shift as shown in Fig. 2.5 (b). The theoretical fitting curves of these values (blue line and the red one) also show obvious deviation from the best fitting curve (the green one) in Fig. 2.5 (b). Therefore, the uncertainty of the measured thermal resistance is estimated at $+0.08/-0.09\times10^{-7}$ Km^2W^{-1}.

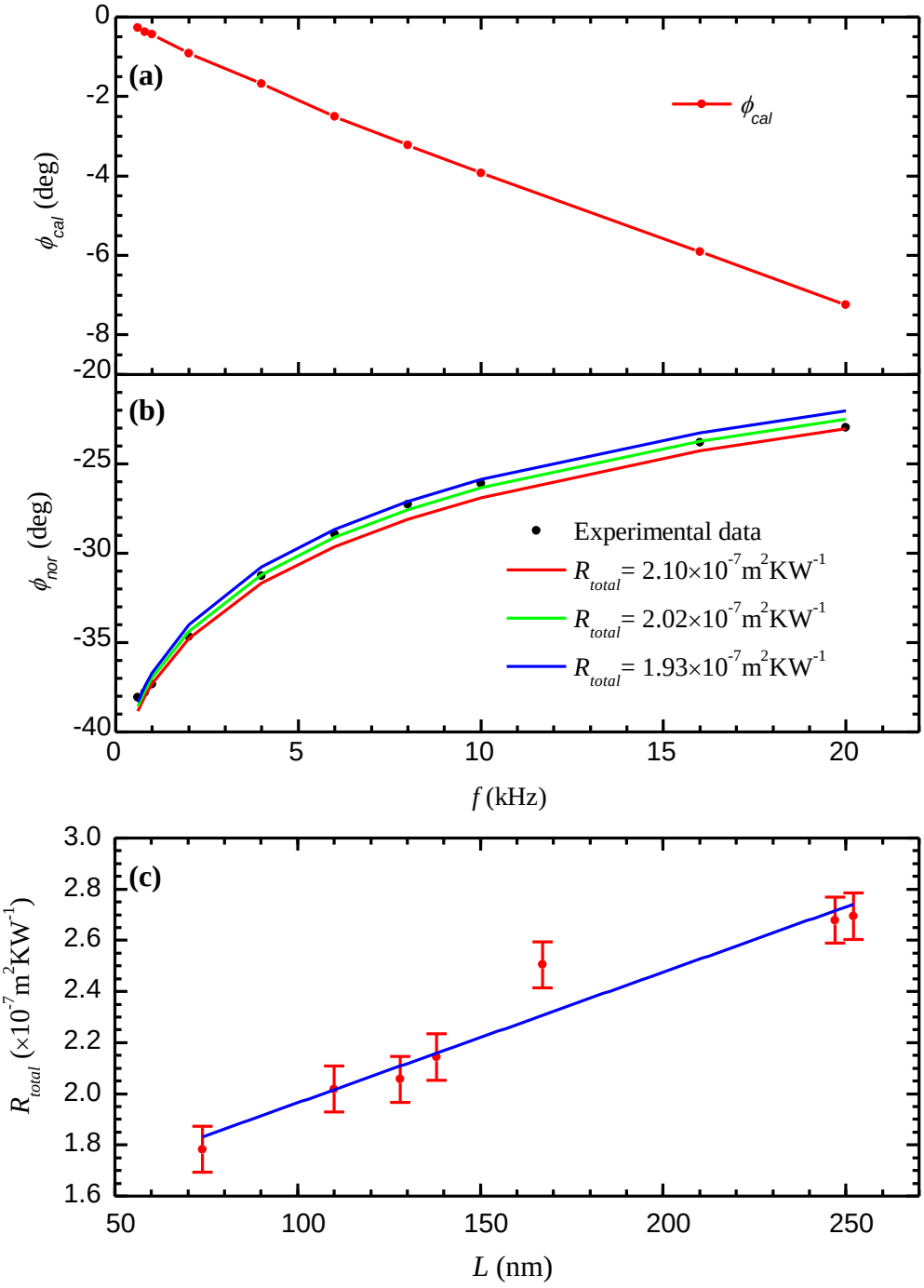

Figure 2.5 (a) Phase shift of the reflection beam that serves as a calibration of the experimental system. (b) Phase shift fitting result of sample Aa2 (single-layered β-W with a thickness of 110 nm). The total thermal resistance (R_{total}) is determined at 2.02×10^{-7} Km^{2}W^{-1} with the best fitting (green line) for this sample. The blue line and red line are theoretical curves when R_{total} takes the value of 1.93 × 10^{-7} Km^{2}W^{-1} and 2.10 × 10^{-7} Km^{2}W^{-1} to show the fitting sensitivity. (c) Linear fitting

of R_{total} versus L from where k of β-W films and $R_{W/SiO_2/Si}$ are determined at 1.98 $Wm^{-1}K^{-1}$ and 1.43 × 10^{-7} Km^2W^{-1}, respectively.

R_{total} of the samples can be expressed as the following equation:

$$R_{total} = L/k + R_{W/SiO_2/Si}. \quad (2.6)$$

Since all the β-W films are prepared using the same substrate and under the same conditions, k of β-W films and $R_{W/SiO_2/Si}$ are expected to have negligible variation among samples (despite the film size effect which will be discussed later). As a result, we expect a linear relation between R_{total} and L. Figure 2.5 (c) shows the measured R_{total} versus L for the single-layered β-W films studied in this work. An obvious linear relation is observed. Based on linear fitting, k of β-W films and $R_{W/SiO_2/Si}$ are determined at (1.98 ± 0.06) $Wm^{-1}K^{-1}$ and (1.43 ± 0.02) × 10^{-7} Km^2W^{-1}, respectively. In the range of the laser modulation frequency (600 Hz to 20 kHz), the thermal diffusion depth in one period ($\sqrt{\alpha/f}$) varies from 35 μm to 6.1 μm, which is much larger than the sample thickness. However, thermal diffusion depth in one-degree phase ($\sqrt{\alpha/f \cdot 360}$) varies from 1.9 μm to 0.32 μm, comparable to the thickness of the sample. Figure 2.5 (b) also shows that the phase shift method is sensitive in our experiment. The k value is much smaller than that of bulk α-W (174 $Wm^{-1}K^{-1}$). As there is no record for k of β-W, we will try to explain this low thermal conductivity of the metastable β-W from the Wiedemann-Franz (WF) law assuming that electrons still dominate in thermal conductance of this material.

Thermal conductivity is related to the electrical conductivity (σ) by the WF law at relatively not-very-low temperatures by the following equation:

$$L_{lorenz} = \frac{k}{\sigma T}, \quad (2.7)$$

where L_{Lorenz} is the Lorenz number and for tungsten L_{Lorenz} is 3.04×10^{-8} W·ΩK^{-2} at 300 K. [87] σ is calculated at 2.17×10^{5} Sm^{-1} based on our measured k, corresponding to an electrical resistivity (ρ) of 4.61×10^{-6} Ω·m (or 461 μΩ·cm). This value is comparable to the reported electrical resistivity for this phase of W [74, 77, 88-91]. For instance, early work by Petroff *et al*. [91] reported an electrical resistivity of β-W ranges from 150-350 μΩ·cm. Following work by O'Keefe *et al*. [74] reported an even higher electrical resistivity of as-deposited β-W (155-870 μΩ·cm) and found that even after rapid thermal annealing, it can still be as high as 478 μΩ·cm. Recent work by Hao *et al*. [90] measured the electrical resistivity of β-W with different thicknesses and extracted a value of about 195 μΩ·cm. The relatively high electrical resistivity (compared with 5.33 μΩ·cm for the bulk pure α-W [90]) will be discussed in detail below.

As the film is very thin, the cross-plane σ is not easy to measure directly. We have measured the in-plane σ of the films by using the four-probe method for comparison [92, 93]. Figure 2.6 (a) shows the schematic of the four-probe method. The two out probes (probes 1 and 4) are fed with a DC current while the voltage is measured from the two inner probes (probes 2 and 3). Figure 2.6 (b) shows the experiment setup of the four-probe method in our lab. The four probes are fixed on the 3D microstage which makes the contact between probes and the sample much flexible. The orange wires are connected with a DC current source and a multimeter while the copper piece below the four pins represents the samples that are measured in our experiment.

A current I is fed through the two outer probes and the voltage V is measured between the two inner ones. The sheet resistivity of samples can be expressed as: $R_s=F_1F_2F_3V/I$, where

F_1 is the finite shape correction factor, F_2 the probe spacing correction factor and F_3 the thickness correction factor. F_1 can be derived from the existing standard table [94]. F_2 can be calculated by the following equation [94]:

$$F_2 = 1 + 1.082 \cdot \left(1 - \frac{S_2}{S}\right), \tag{2.8}$$

where S_2 is the spacing between the two inner probes and S the average probes spacing. In our experiment, with equal spacing between adjacent probes, F_2 is taken as 1. F_3 is also taken as 1 for all the samples, as in our case the thicknesses (t) of all these films are very small which means $t/s << 0.4$.

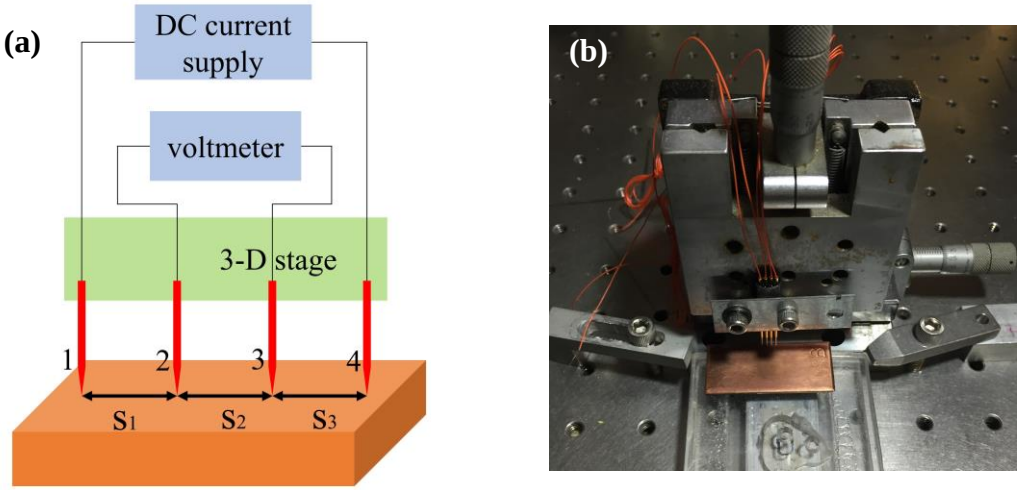

Figure 2.6 (a) Schematic of the four-probe method. (b) Experimental setup of the four-probe measurement in our lab.

The in-plane electrical conductivity of β-W is calculated as $\sigma = 1/(R_s t)$ and the results are listed in Table 2.2. The corresponding ρ varies from 258 to 316 μΩ·cm which is in the well accepted range (150-350 μΩ·cm) of β-W [91]. Typically, the relatively higher resistivity in thin metallic films is attributed to the carrier momentum loss along the current flow direction due to surface and grain boundary scattering which is commonly explained by using the Fuchs-

Sondhermer (FS) surface scattering model [95, 96] and the Mayadas-Shatzkes (MS) grain boundary model, [97, 98] respectively. However, the finite-size effect and the grain boundary scattering are not sufficient to account for the large resistivity of β-W. According to Hao's recent work, the electrical resistivity of bulk β-W is calculated at 195 ± 3 μΩ·cm with an effective MFP (l_{eff}) of only about 0.45 nm at 300 K [90]. This means l_{eff} of β-W films may be ten to hundred times smaller than the averaged grain size and the film thickness [see Fig. 2.3] of our samples. Calculations using the FS model and the MS model show that when the thickness or grain size is much larger than l_{eff}, surface scattering or grain boundary scattering has negligible influence on the resistivity of thin metallic films [96]. Other scattering mechanism must exist and dominate the electron transport property. One possible explanation is the charge carrier concentration. Recent work by Lee *et al*. [77] obtained the charge carrier concentration of different phase of W by using Hall measurement and found a much low carrier concentration of the β-phase one. Another possible reason is the impurities, where a small amount of oxygen is believed to exist and induce the β-W formation without forming a W_xO compound [73]. Such a dilute bulk of impurities may induce significant electron scattering. This also helps explain the large range of reported resistivity of β-W which may be due to the different concentration of oxygen induced impurities. The local structure may be another reason as β-W is believed to be a mixed phase consisting of ordered and stacking faulted W_3W structures [91]. Considering the relatively larger grain size, local disorders or dislocations of atoms may play an important role. So far, as there is no clear mechanism for the large resistivity, further work, particularly theoretical study, is needed.

The discrepancy in the thermal conductivity determined by the PT technique and the four-probe method is mainly attributed to the anisotropy of the β-W films. The β-W films are produced in the vacuum magnetron sputtering system, where the deposited metal films typically show kind of columnar structure. For the tungsten films prepared in this work, the columnar structure can be clearly seen from the SEM images in Fig. 2.3. This means the crystal orientation and crystallite size in the in-plane and cross-plane directions are much different. Thus, the electrical and thermal transport properties which are closely related to the structure of materials also have much difference in the two directions.

Table 2.2 In-plane electrical and thermal conductivity of single-layered β-W

Samples	V/I (A)	F_1	σ ($\times 10^5\ \Omega^{-1}m^{-1}$)	ρ ($\mu\Omega\cdot$cm)	k ($Wm^{-1}K^{-1}$)
Aa1	9.85	4.03	3.40	294	3.11
Aa2	5.79	4.05	3.87	258	3.53
Aa3	5.30	3.84	3.56	281	3.25
Bb1	5.77	3.94	3.44	291	3.14
Bb2	3.92	3.72	3.61	277	3.29
Bb3	3.12	3.92	3.31	302	3.02
Dd1	4.59	3.91	3.33	300	3.04
Dd2	3.14	3.99	3.17	316	2.89
Dd3	2.47	2.83	3.56	281	3.25

Despite this anisotropy in σ and k, the validation of WF law is also questionable. It has been widely studied that, for nanocrystalline films, the Lorenz numbers are very different from their corresponding bulk values. For example, Yoneoka *et al*. [99] reported an average Lorenz number of 3.82×10^{-8}, 2.79×10^{-8}, and 2.99×10^{-8} $W\Omega K^{-2}$ for 7.3-, 9.8-, and 12.1-nm Pt films, respectively. Experimental results of Zhang and co-workers [100, 101] showed that the

Lorenz number of 21-37 nm and 53 nm thick polycrystalline Au films are around 7.0×10^{-8} and 5.0×10^{-8} $W\Omega K^{-2}$, respectively. Calculations by Ou *et al*. [102] revealed that the Lorenz number of a 180-nm nickel nanowire is a little higher than the bulk value. Previous experimental work [103] on ultrathin iridium films (0.6-7 nm) in our lab showed that the Lorenz number ranges from 5.83×10^{-8} to 7.8×10^{-8} $W\Omega K^{-2}$. As there is no literature data for the Lorenz number of β-W nanofilms and how it will deviate from the bulk value is not clear to our knowledge, the use of WF law based on the bulk's Lorenz number may be not suitable in this work. Therefore, considering the unclear anisotropy level of the β-W nanofilms and the deviation of the Lorenz number, we intend to extract thermal conductivity directly by performing the PT measurements on this group of samples in this section.

2.3.2 Thermal conductance between β-W sublayers.

Not like the samples in the first group, the samples in this group were grown several times, that is, these samples consist of different number of sublayers [see Fig. 2.1 (b)]. The SEM images also clearly show separated layers in these films [see Fig. 2.3]. The experiments are operated under the same conditions as those of the first group. Notice that, in the fitting process of the first group for a single-layered sample, the fitting itself cannot distinguish the thermal resistance of the β-W films from other resistances. This also holds true for the multilayered β-W samples. Figure 2.7 (a) shows the fitting process, from which we can see the fitting curve matches the experimental data well. After the fitting process, R_{total} of each sample in this group is calculated. The inset in Fig. 2.7 (b) shows R_{total} versus L of both the single-layered β-W films (black rectangles) and the multilayered β-W films (red circles). We can see all these points show a linear relationship and that the differences of R_{total} between the single-

layered β-W films and the multilayered ones are not significant. This points out that $R_{W/W}$ will be small. It is determined as below.

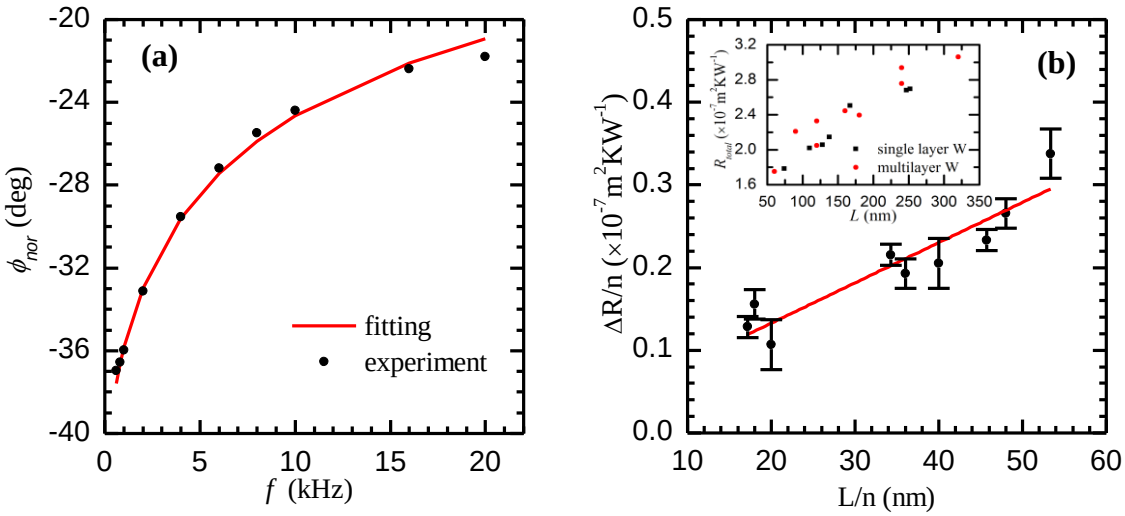

Figure 2.7 (a) Phase shift fitting of sample a3 (8 layers of β-W films with a total thickness of 120 nm). The total thermal resistance (R_{total}) is determined at 2.05 × 10^{-7} Km^2W^{-1} for this sample. (b) Linear fitting of $\Delta R/n$ versus L/n, from which the thermal resistance $R_{W/W}$ between β-W sublayers is determined at 3.57 × 10^{-9} Km^2W^{-1}. The inset shows total thermal resistance versus sample thickness of both the single-layered (black rectangles) and the multilayered (red circles) β-W films.

R_{total} of the multilayered β-W films can be expressed as the following equation:

$$R_{total} = L/k + R_{W/SiO_2/Si} + nR_{W/W} . \tag{2.9a}$$

So, we have

$$\Delta R = R_{total} - R_{W/SiO_2/Si} = L/k + nR_{W/W} . \tag{2.9b}$$

$R_{W/SiO_2/Si}$ determined in the above section can be used here for data processing since the film synthesis is under the exactly same condition. And then we have

$$\frac{\Delta R}{n} = \frac{L}{n}\frac{1}{k} + R_{W/W} . \tag{2.9c}$$

When plotting $\Delta R/n$ versus L/n, these points also show a linear relationship as shown in Fig. 2.7 (b). From Eq. 2.9 (c) we can see that the slope of the linear relation is related to the reciprocal of k and the intercept is related to $R_{W/W}$. k determined here (2.05 ± 0.36 $Wm^{-1}K^{-1}$) is a little higher than (but very close to) that of the single-layered β-W films in the first group (1.98 ± 0.06 $Wm^{-1}K^{-1}$). Considering the uncertainties of the experiment and data processing, we conclude that the samples from the two groups have negligible structure difference during sample preparation. From the linear fitting, $R_{W/W}$ is determined at $(3.57 \pm 2.67) \times 10^{-9}$ Km^2W^{-1}. This $R_{W/W}$ investigation serves as a comparison base for the $R_{W/Gr}$ study that will be described in the next section. At this point, we can conclude that the β-W/β-W interface thermal conductance ($G_{W/W}$) has an average of about 280 MW $m^{-2}K^{-1}$.

The in-plane electrical conductivity and resistivity of these multilayered β-W films has also been measured by using the four-probe method. Although there are some variations in several samples, the electrical conductivity and resistivity of the samples in this group have no significant difference with those in the first group. Considering the large thickness difference between the single-layered films and the multi-layered ones, the previous assumption that the size-effect or surface-scattering play a tiny role in the very high resistivity has also been proved. The electron thermal conductivity in the in-plane direction is also calculated using the WF law, which is larger but still comparable to that in the cross-plane direction. The calculation results are detailed in Table 2.3.

Table 2.3 In-plane electrical and thermal conductivity of multilayered β-W

samples	V/I (A)	F_1	σ ($\times 10^5$ $\Omega^{-1}m^{-1}$)	ρ ($\mu\Omega\cdot$cm)	k ($Wm^{-1}K^{-1}$)
a1	9.48	3.79	4.64	215	4.23
a2	4.66	4.05	5.89	167	5.38
a3	2.94	3.90	7.25	138	6.61
b1	6.31	3.91	3.38	296	3.08
b2	4.23	3.75	3.50	286	3.19
b3	2.67	3.83	4.07	246	3.71
d1	5.23	3.29	3.63	275	3.31
d2	3.15	3.60	3.67	272	3.34
d3	2.27	3.72	3.71	270	3.38

2.3.3 Thermal conductance between β-W and graphene.

The samples in this group have the same thicknesses as those in the second group, respectively. Compared with samples in the second group, the difference is that we have graphene layers sandwiched between tungsten sublayers [see Fig. 2.1 (a)]. The experimental setup of the PT technique is the same as those of the first two groups. What we can get is R_{total} induced by the β-W films, $R_{W/Gr}$, and $R_{W/SiO_2/Si}$. Figure 2.8 shows the fitting result of several samples from this group. We can see the theoretical phase shifts match the experimental data very well. For single-layered graphene, the graphene-induced thermal resistance is from the two β-W/Gr interfaces. For there are two-layered graphene, thermal resistance across the Gr/Gr interface ($R_{Gr/Gr}$) can be estimated as $R_{Gr/G}=l/k_{Gr}$ with l the distance between graphene layers (0.335 nm) and k_{Gr} the cross-plane thermal conductivity of graphene (5.7 $Wm^{-1}K^{-1}$). [104]

Accordingly, $R_{Gr/Gr}$ is about 5.9×10^{-11} Km^2W^{-1}, much smaller than R_{total}. Thus, the intrinsic thermal resistance of the graphene layers can be neglected in this experiment. With k of β-W films taken as 1.69~2.41 $Wm^{-1}K^{-1}$ and $R_{W/SiO_2/Si}$ taken as $(1.43 \pm 0.2) \times 10^{-7}$ Km^2W^{-1}, $R_{W/Gr}$ of all the samples in this group can be calculated by using the following equation:

$$R_{total} = L/k + R_{W/SiO_2/Si} + 2nR_{W/Gr}\,. \tag{2.10}$$

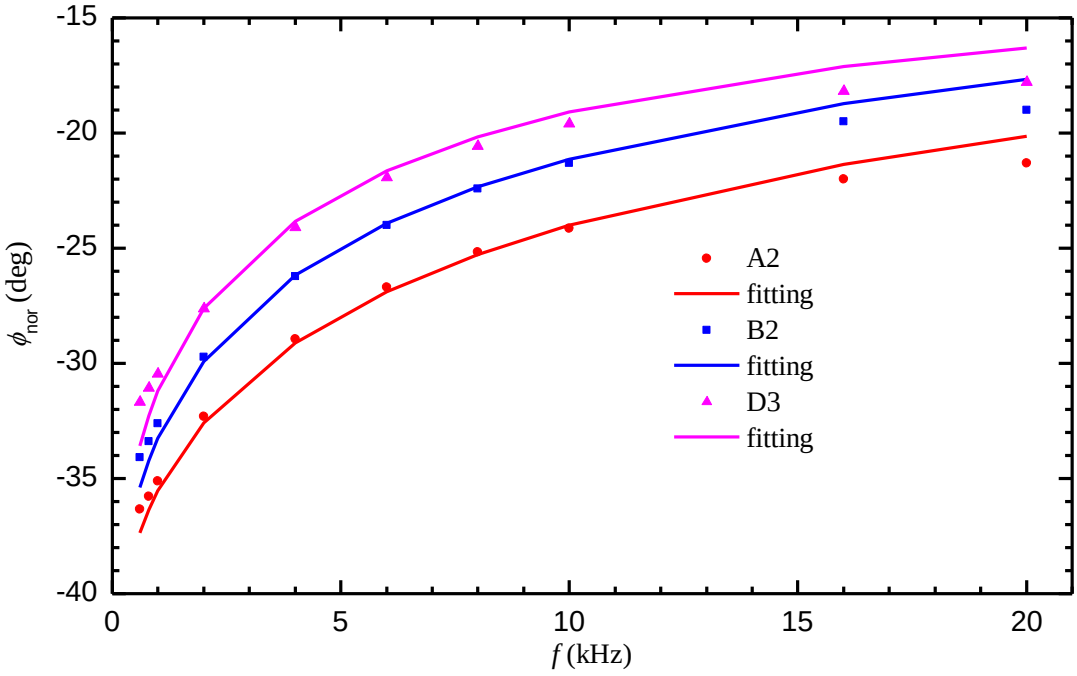

Figure 2.8 Phase shift fitting for three of our samples (A2: 6 layers β-W films one-by-one sandwiched with 5 graphene layers and have a total thickness of 90 nm; B2: 6 layers β-W films one-by-one sandwiched with 5 graphene layers and have a total thickness of 180 nm; D3: 8 layers of β-W one-by-one sandwiched with 7 graphene layers and have a total thickness of 320 nm).

The calculation results are shown in Table 2.4, from which we can see $R_{W/Gr}$ varies from sample to sample and has a maximum value of 9.67×10^{-9} Km^2W^{-1}. The lower and upper limit uncertainties are also given in Table 2.4. These uncertainties show the maximum possible variations of the calculated $R_{W/Gr}$ of each sample. We can see the uncertainties also vary from

sample to sample and has a maximum value of 2.43×10^{-9} Km^2W^{-1}. These variations are mainly attributed to the uncertainty of k of β-W films, which varies from 1.69 to 2.41 $Wm^{-1}K^{-1}$.

Table 2.4 Thermal resistance (10^{-9} Km^2W^{-1}) of β-W/Gr interfaces

Sample	A1	A2	A3	B1	B2	B3	D1	D2	D3
$R_{W/Gr}$	$1.05^{+0.97}_{-0.95}$	$5.08^{+0.82}_{-0.8}$	$3.82^{+0.78}_{-0.76}$	$-0.05^{+1.8}_{-1.78}$	$8.12^{+1.64}_{-1.62}$	$8.7^{+1.59}_{-1.56}$	$5.67^{+2.43}_{-2.35}$	$9.67^{+2.21}_{-2.19}$	$6.23^{+2.14}_{-1.86}$
$R_{2W/Gr}$	$2.10^{+1.93}_{-1.9}$	$11.6^{+1.64}_{-1.6}$	$7.64^{+1.56}_{-1.53}$	$-0.1^{+3.6}_{-3.57}$	$16.2^{+3.28}_{-3.24}$	$17.4^{+3.17}_{-3.13}$	$11.3^{+4.87}_{-4.7}$	$19.3^{+4.42}_{-4.38}$	$12.5^{+4.29}_{-3.71}$
$R_{TW/Gr}$	6.30	58.0	53.5	-0.30	81.2	122	34.0	96.7	87.2

Subscript "$_{Gr}$" represents graphene layers. "$R_{2W/Gr}$" represents thermal resistance induced by a single graphene layer while "$R_{TW/Gr}$" represents thermal resistance induced by all graphene layers in the sample.

Note that, for each graphene layer, it has two W/Gr interfaces (next to the top and bottom β-W layers). In Table 2.4, $R_{2W/Gr}$ represents thermal resistance of two W/Gr interfaces induced by each graphene layer. Also shown in Table 2.4 is the total thermal resistance (named as $R_{TW/Gr}$) induced by all β-W/Gr interfaces in one sample. Most of the $R_{TW/Gr}$ values are much larger than the experimental uncertainty ($8\sim9 \times 10^{-9}$ Km^2W^{-1}). This means the thermal resistance induced by the graphene layers is detectable in our experiment. It is clear that most $R_{2W/Gr}$ is larger than the derived $R_{W/W}$ in the last section, indicating the introduction of graphene layers indeed gives rise to a finite interface thermal resistance. Taking into consideration of the uncertainties, $R_{W/Gr}$ is no larger than 11.9×10^{-9} Km^2W^{-1}. This value is comparable to the Gr/SiO_2 interface resistance ($5.6\sim12 \times 10^{-9}$ Km^2W^{-1}) reported by Chen [35] while is much smaller than that of the epitaxial graphene and SiC interface (5.3×10^{-5} Km^2W^{-1}) reported by Yue. [105] The corresponding thermal conductance ($G_{W/Gr}$) is 84 $MWm^{-2}K^{-1}$ which is also at the high end of the Gr/SiO_2 interface ($20\sim110$ $MWm^{-2}K^{-1}$) reported by Mak and Liu [36] and that of the Au/Ti/Gr/SiO_2 interface (about 25 $MWm^{-2}K^{-1}$) reported by Koh and Bae [37]. This

$G_{W/Gr}$ value is much larger than 4~5 $MWm^{-2}K^{-1}$ reported by Jagannadham on characterizing thermal transport properties of W/Gr/Cu structure [40]. However, in his measurement, the structure was annealed at high temperature where reaction took place between W and graphene which reduces the interface thermal conductance significantly. Recent work by Huang *et al*. [41] reported measurements on thermal conductance of Al/ transferred graphene (trGr)/Cu and Al/ grown graphene (grGr)/Cu interfaces, which is a good representative of the metal/Gr/metal interfaces. The reported *G* of Al/trGr/Cu interface is about 20 $MWm^{-2}K^{-1}$, 35% lower than that of the Al/grGr/Cu interfaces (about 31 $MWm^{-2}K^{-1}$). This lower *G* of the Al/trGr/Cu interface is attributed to the lower conformity of trGr to Cu substrate, which is further confirmed by the increase of *G* after the annealing treatment. The different degree of conformity could also be a reason for the variations of our measurement results. Despite the variations, our calculated $G_{2W/Gr}$ is no smaller than 42 $MWm^{-2}K^{-1}$, still larger than 31 $MWm^{-2}K^{-1}$ of the intrinsic value of their Al/Gr/Cu interface. The relatively large interface conductance of our β-W/Gr/β-W interfaces is due to the unique structure of the samples. One possible reason is that the graphene transfer and processing will inevitably introduce functional groups or defects to the graphene surface. These functional groups or defects may enhance the energy coupling between β-W films and graphene. Another reason may be the damage of graphene during the β-W sputtering progress, where additional channels of direct heat transport between the β-W films form and significantly enhance the thermal conductance of the interfaces. This damage enhanced phenomenon has been studied in the most recent work by Huang *et al*. [42] In this work, they reported measurements on thermal conductance of Pd/trG/Pd interface with the top Pd prepared by either thermal evaporation or rf magnetron sputtering. The results shown that, *G* of the sample with the rf magnetron sputtering Pd is 300 $MWm^{-2}K^{-1}$ at RT, seven times larger

than that with the thermal evaporation Pd (42 $MWm^{-2}K^{-1}$). This enhancement is attributed to the electronic heat transport via atomic scale pinholes formed in the graphene during sputtering process, which has also been proved by the AFM characterization. This can also help explain the variations and even negative value of $R_{W/Gr}$ in Table 2.4 as the graphene transfer process is manual and the damage level from metal sputtering cannot be predicted.

The four-probe measurement is also performed on the samples in this group and the results are summarized in Table 2.5. The electrical resistivity varies from 270 to 351 μΩ·cm, a little larger than those of the first two groups due to the inserted graphene layers but still in the well-accepted range (150-350 μΩ·cm [91]). σ and correspondingly in-plane electron-induced k are also calculated (see Table 2.5). k varies around 3 $Wm^{-1}K^{-1}$ which is also comparable to those of the single-layered and multilayered β-W samples detailed in Table 2.2 and Table 2.3.

Table 2.5 In-plane electrical and thermal conductivity of multilayered β-W/Gr

Samples	V/I (A)	F_1	σ ($\times 10^5$ $\Omega^{-1}m^{-1}$)	ρ (μΩ·cm)	k ($Wm^{-1}K^{-1}$)
A1	12.9	4.00	3.24	309	2.95
A2	7.53	3.98	3.70	270	3.38
A3	5.90	4.05	3.49	287	3.18
B1	6.17	3.85	3.51	285	3.20
B2	4.24	3.86	3.40	294	3.10
B3	3.36	4.02	3.09	324	2.82
D1	4.96	3.92	3.22	311	2.93
D2	3.69	3.96	2.85	351	2.60
D3	2.79	3.91	2.86	350	2.61

CHAPTER 3. SUB-μm *c*-AXIS STRUCTURAL DOMIAN SIZE OF GRAPHNE PAPER UNCOVERED BY LOW-MONENTUM PHONON SCATTERING

In this chapter, the *c*-axis thermal conductivity of GP was measured from 295K down to 12.3 K by employing the PLTR2 technique. We developed an anisotropic specific heat model based on the phonon propagation direction and identified the specific heat that sustains heat conduction along the *c*-axis. Combined with a residual thermal reffusivity theory, this model predicted a large structural domain size for widely studied normal graphite, which is consistent with that determined from transmission electron microscopy. Based on the low-momentum phonon scattering uncovered by the 0 K limit thermal reffusivity, the *c*-MFP induced by defect in GP was evaluated, which significantly exceeds the graphene flake thickness in this material. By subtracting the residual thermal reffusivity from defects, the defect-free *c*-axis thermal conductivity and *c*-MFP were obtained and compared with those predicted by the recent MD simulation.

3.1 Experimental details

A pulsed laser-assisted thermal relaxation 2 (PLTR2) technique is developed to study the thermal transport properties of GP in the cross-plane direction. The PLTR2 technique is based on the laser flash method, which is widely used for the measurement of thermal diffusivity [106-108]. In the laser flash method, a short laser pulse is used to uniformly irradiate the front surface of the specimen and induces a local temperature rise. Then heat transfer occurs from the front surface to the back surface across the specimen. The temperature response of the back surface is detected by an infrared detector and used to extract the thermal diffusivity of the specimen. In the current work, our sample is very thin (tens of μm). Although the nanosecond laser flash method can be used to measure the thermal diffusivity of such samples

at RT, at very low temperatures, the backside radiation has a wavelength in the order of a few 0.1 mm. This makes the thermal response measurement extremely challenging and difficult using the radiation detector. In the PLTR2 technique, instead of the thermal radiation detector, an Iridium coating of the back surface is fed with a DC current and acts as the temperature sensor. The PLTR2 technique, which is an improvement on the PLTR technique developed previously in our group [109], is capable of determining thermal transport properties of films both in the in-plane and cross-plane directions [110, 111].

3.1.1 Sample preparation and characterization

The GP sample is purchased from Graphene Supermarket. Note that GP has very high electrical conductivity (4.4×10^4 Sm^{-1} [66]), so that it should be insulated from the Ir coating to make sure only the electrical resistance variation induced by the back surface temperature evolution is detected. In this work, we use a PET film as an isolator to separate Ir coating from GP. Figure 3.1 shows the schematic of the sample preparation process. A 500 nm-thick PET film is purchased from Goodfellow. A 20 nm Ir is sputtering coated on one side of the PET film within an area similar to that of the GP sample. After the coating process, a small drop of PMMA/toluene solution (1% mass percentage) is put on one side of the GP sample. The PMMA/toluene solution is prepared by dissolving PMMA particles in toluene solvent. The PMMA particles are purchased from Sigma-Alorich. 0.2 g PMMA particles are mixed with 19.8 g toluene solvent in a closed glass bottle and then stirred with a magnetic stirrer for more than 24 hours at 50 ^oC to make sure that the PMMA particles are totally dissolved in toluene. Immediately after the solution expands and covers the whole side, the GP sample is attached to the PET film with the solution facing the uncoated side of PET film. In a few hours, the toluene solvent will volatilize and good attachment among GP, PMMA and PET forms. Then

the sample is suspended between two electrodes with the Ir coating facing the electrodes and forming an electrical circuit. (The electrodes are made from Silicon wafers and coated with 180 nm Ir to provide high electrical and thermal conductance.) In this step, silver paste is used to optimize the electrical and thermal contacts between the Ir coating and the electrodes. The most challenging thing is to make sure that only the Ir coating not the GP is in the electrical circuit with such thin PET and PMMA film.

In the PLTR2 model, the thicknesses of the film layers are key parameters during the thermal relaxation process. However, in the micro/nanometer scale, the thickness is difficult to determine directly, especially for the PMMA film that forms from solution. To get a better evaluation of the thicknesses of the films, the thermalgravimetric analysis (TGA) is performed on the sample after the PLTR2 measurements. With the lateral dimensions measured under an optical microscope and the densities referred from literature, the thicknesses of GP, PMMA and PET layers are determined, respectively. In the present work, the lateral dimensions for the TGA sample is 3.7×1.9 mm^2 and the densities of GP, PMMA and PET used here are 2210, 1180 and 1350 kgm^{-3}, respectively. Figure 3.2 (a) shows the TGA results of the sample, from which we can see two clear peaks in the first derivative of the weight loss (DTG) curve (red). These two peaks represent the weight loss from the evaporation of the PMMA and PET films. From the peak areas, the total mass of the PMMA and PET films in the sample is calculated at 15.4 µg. The thickness of PET is determined as 0.58 µm by measuring the weight of a single PET film with a lateral dimension of 4.87×3.80 cm^2. This thickness value is consistent with the product description of 0.5 µm within 20% uncertainty. Thus, the thickness of the PMMA film is determined as 1.2 µm. The rest material after the TGA is only GP and the mass can be

easily determined. Assuming homogeneous thicknesses of these films in the sample, the thicknesses of the GP, PMMA and PET are 21.4, 1.2 and 0.58 μm respectively. These values will be used in the numerical calculations for data processing which will be detailed in the following section.

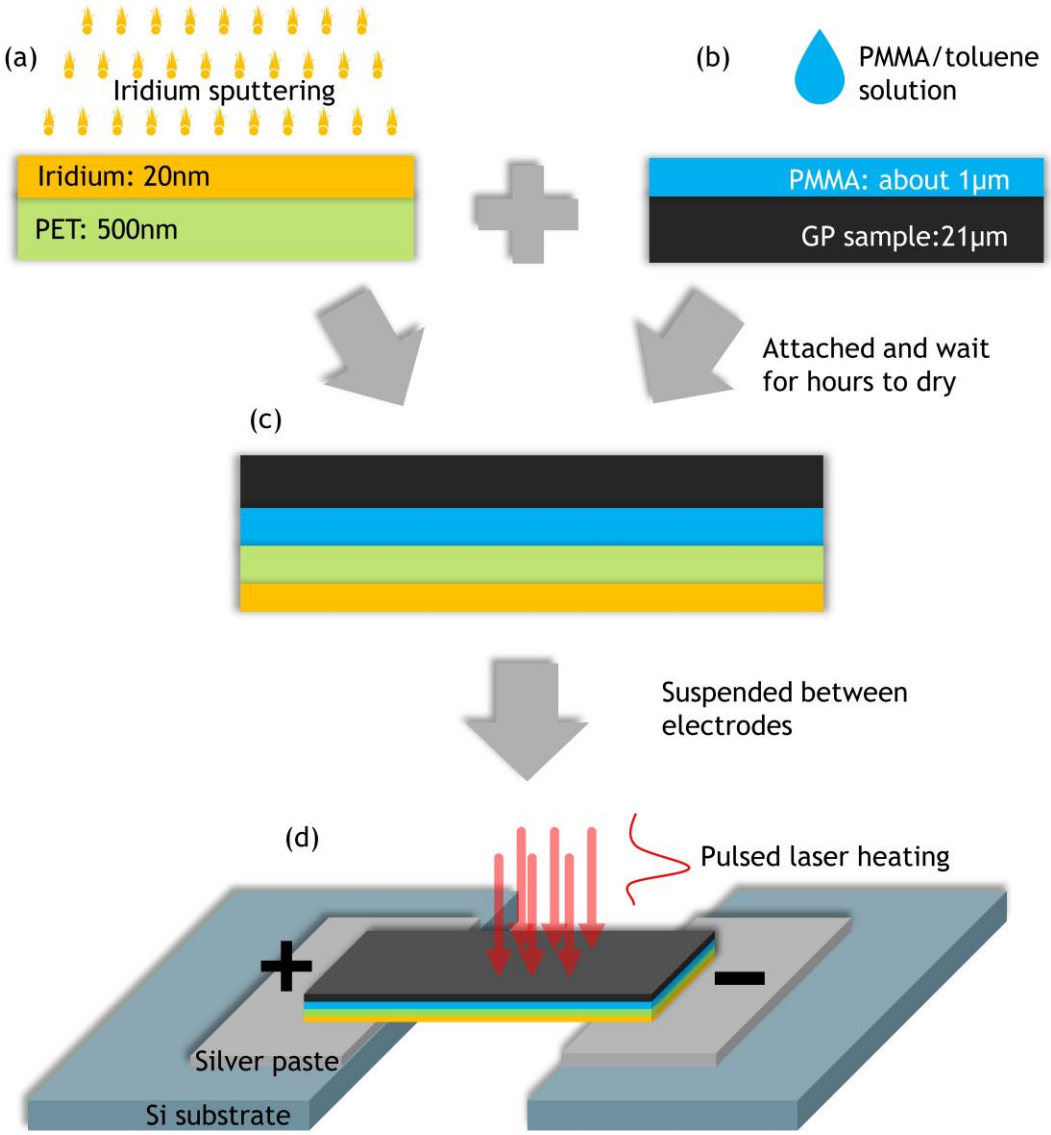

Figure 3.1 Sample preparation process. (a) Sputtering coating of 20 nm Ir on one side of the PET film; (b) A small drop of PMMA/toluene solution is putting on one side of GP and expands to cover the whole side; (c) The GP sample is attached to the PET film immediately after the expansion of the solution with the solution facing the uncoated side of PET film; (d) The multilayered sample is suspended between two

electrodes with the Ir coating facing these electrodes. Then the sample is connected to an electrical circuit through the Ir coating and exposed to the pulse laser heating for the PLTR2 measurements.

The structure of the GP sample is characterized by using XRD, Raman spectroscopy and scanning electron microscope (SEM). Figure 3.2 (b) shows the XRD spectrum of the GP sample, from which a sharp peak can be seen at 26.6 degrees of 2θ. This peak corresponds to the (002) plane of GP, from which the interlayer spacing is determined at 3.35 Å, the same as that of pristine graphite [112]. This also proves that the GP sample here has high quality and excellent ordered structure. The crystallite size cannot be determined from XRD as the peak linewidth reaches the limit of machine broadening. Figure 3.2 (c) shows the Raman spectra from different positions of the GP sample. Two clear peaks can be seen at about 1581 and 2719 cm^{-1}, which correspond to the G peak and 2D peak, respectively. The D peaks in all spectra are invisible, indicating rare defects and high crystallinity of the graphene flakes. In addition, all the spectra are almost consistent with each other, meaning the numbers of layers in the graphene flakes have high consistency. The ratio of the integrated intensities of G peak to 2D peak is estimated at 0.7, corresponding to 5~6 layers graphene in the flakes [82]. Figure 3.2 (d) shows the SEM image of GP under a 500 × magnification, from which we can see the smooth surface and clear stacking layered structure of the graphene flakes. The x-ray photoelectron spectrometer (XPS) study has also been conducted on the GP in our previous work [66]. The result shows that the elemental composition is C 1s (98.91%), O 1s (0.66%) and F 1s (0.43%), indicating that the GP is of highly pure carbon material.

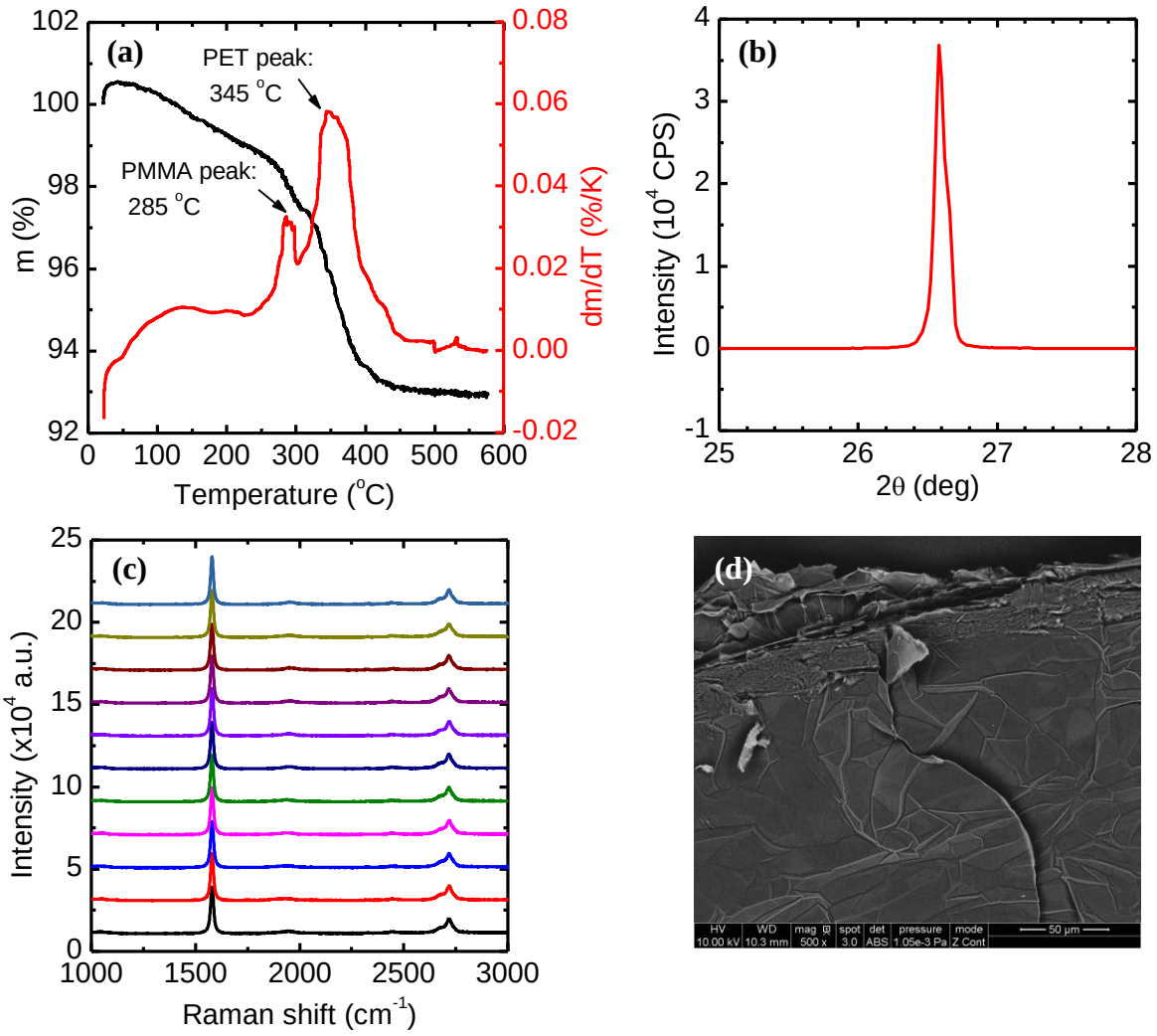

Figure 3.2 Sample characterization. (a) TGA results of the multilayered sample with the black curve as the weight loss (TGA) and red curve as the first derivative of the weight loss (DTG). (b) XRD spectrum of the GP sample, which shows a clear single peak at 26.6 degree of 2θ. (c) Raman spectra from different positions of the GP sample from which the layer number in graphene flakes is determined. (d) SEM image of the GP sample, showing smooth surface and clear stacking structure.

3.1.2 Experimental setup and physical model

The thermal conductivity of GP in the cross-plane direction is measured by using the PLTR2 technique. Figure 3.3 shows the schematic of the experimental setup. During the measurement, the sample is kept in a vacuum chamber with a pressure less than 0.6 mTorr to

eliminate the influence of heat convection from the sample surface. The environmental temperature is controlled through the cooling head under the substrate by the Janis closed cycle refrigerator (CCR) system. This CCR system can provide stable temperature from RT down to 10 K with an accuracy of 0.5 K. To make sure the sample reaches the controlled temperature, we wait for about 40 min after each set of the experimental temperature. A constant DC current (Keithley 6221) is fed to the sample and forms an electrical circuit through the back-side Ir coating. The electrical resistance and voltage variations of the Ir coating are detected by an oscilloscope (Tektronix MDO 3052). A nanosecond pulsed laser is used to irradiate the front surface of the GP and heat transfer occurs in the GP/PMMA/PET multilayer films. The temperature of the Ir coating will evolve to a maximum value and then decrease slowly as the heat dissipates to the environment. In our measured temperature range, the electrical resistance of Ir is linear related to the temperature variation, especially with a small temperature rise during a single measurement. Therefore, the temperature response can be detected by the electrical resistance or voltage changes of the Ir coating.

In this work, the laser pulse width is about 8 ns (shown in Fig. 3.3) which is more than three orders of magnitude smaller than the cross-plane thermal relaxation time (at the μs scale). In this case, the finite pulse duration effect is negligible. We use a Si photodiode connected with the oscilloscope to trigger the sample voltage evolution after a laser pulse. The position of the laser pulse in the time scale is taken as the beginning time of the thermal relaxation which is of key importance in the laser flash model. With a cover (not shown in Fig. 3.3) before the sample we can make sure that only the suspended part of the sample is irradiated. Due to the much larger original laser spot size (diameter of about 3.5 cm) compared with the sample

length (about 7 mm as suspended and irradiated), it is true that the pulse energy is uniformly absorbed by the irradiated sample within a small depth at the front surface. In practice, heat will dissipate in the in-plane and cross-plane direction simultaneously. While in this work, with a large ratio of characteristic lengths in the two directions (mm scale to μm scale), we can safely simplify the thermal transport as 1D in the cross-plane direction and then in the in-plane direction. Our recent work [66] shows that the in-plane thermal diffusivity (α_a) of the GP sample is no larger than 5.57×10^{-4} m^2s^{-1} before switch-on. The characteristic thermal relaxation time is defined as $t_c=L^2/\alpha$. With the in-plane characteristic length taken as 7 mm, the in-plane t_c is calculated as 88 ms. For comparison, the thermal relaxation time in the cross-plane direction (t_{cr}) is no longer than 100 μs [Fig. 3.4 (a)], nearly three orders of magnitude smaller than that in the in-plane direction. This means during the time of thermal transport in the cross-plane direction, thermal transport in the in-plane direction is negligible. When the temperature reaches uniform in the cross-plane direction, heat dissipation starts in the in-plane direction to the electrodes. This simplification in the PLTR2 technique has been proved in determining thermal diffusivity of thin films both in the cross-plane and in-plane directions from a single measurement [110, 111].

For multilayered films, with the 1D heat transfer model, the transient temperature rise $T(x,t)$, can be obtained by solving the governing equation for each layer: [108]

$$\frac{\partial T_i(x,t)}{\partial t} = \alpha_i \frac{\partial^2 T_i(x,t)}{\partial x^2},\ i=1, 2, 3 \tag{3.1}$$

with the initial value $T_1(x,0) = Q / A\tau_{opt}\rho_1 c_{p,1}$, for $0 < x < \tau_{opt}$, and $T_1(x,0) = 0$, for $x > \tau_{opt}$ and $T_{2,3}(x,0) = 0$. Here, i =1, 2, 3 represent the GP, PMMA, and PET layers, respectively. Q is the

absorbed pulse energy; A is the irradiated surface area of the sample; $\rho_1 c_{p,1}$ volumetric heat capacity of the irradiated layer; τ_{opt} is the optical absorption depth of the irradiated layer and is taken as 31.7 nm for GP [113].

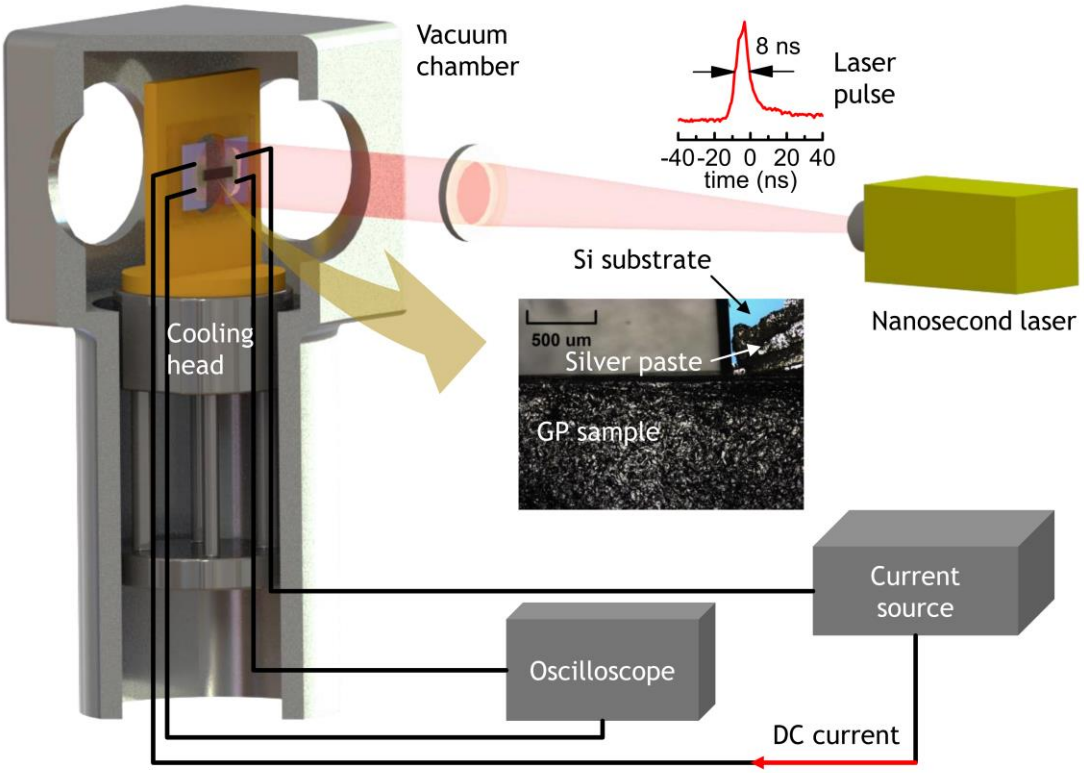

Figure 3.3 Schematic of the experimental setup of the PLTR2 technique. The sample is put into a vacuum chamber and the environmental temperature is controlled by the cooling head under the substrate. The Ir coating at the back surface is connected to a current source and an oscilloscope for the detecting of the back-surface temperature. A nanosecond pulsed laser irradiates the front surface of the sample to introduce temperature gradient and heat conduction across the sample. The insets show the laser pulse duration and part of the GP/PMMA/PET multilayered sample prepared in this work.

Analytical solutions to 1D thermal transport model in two-layered or three-layered composites have been described in detail [108, 114, 115]. However, those solutions are much complicated. In the present work, instead of solving the governing equation analytically, a

numerical method is used to simulate the 1D thermal transport across the GP/PMMA/PET three-layered film and obtain the temperature response at the back surface. In the simulation process, each layer film is assumed to be homogenous with the densities, specific heat [inset in Fig. 3.4 (c)] and thicknesses are all known parameters [116-118]. Thermal conductivities of the PMMA and PET layer are also taken from literatures [Fig. 3.4 (c)] [119, 120]. The only unknown parameter is k_c of GP. With different trial values of k_c input in the simulation process, different temperature response curves at the back surface can be obtained. Then the least square method is used to extract the value that can give the best fit of the experimental one.

3.2 Thermal conductivity variations against temperature

In the PLTR2 measurements, the GP sample is 7 × 1.9 mm^2 with a thickness of 21.4 μm. The initial electrical resistance of the Ir coating is 85.4 Ω. We feed a DC current of 11.6 mA at RT through the sample and measure its voltage to track the temperature evolution. The initial electrical resistance changes with the environmental temperature and we choose different feeding current at different temperatures to make sure the overall initial voltage does not change too much. The nanosecond laser irradiates the sample with an original laser spot size of about 3.5 cm and a frequency of 1 Hz. The pulse energy is also chosen at different environmental temperatures to give sufficient signal to noise ratio, yet small temperature rises. Figure 3.4 (a) shows the experimental data from the PLTR2 measurements and the best simulation curves under several environmental temperatures in this work. We can see the simulation curves and the experimental data match with each other very well, despite the small discrepancies at the beginning time. The discrepancies come from the electrical disturbance from the laser system when the pulse is feeding which will disappear soon and have negligible influence on the overall fitting results. The extracted k_c of GP under these temperatures are

also noted in Fig. 3.4 (a). Also shown in Fig. 3.4 (a) are the half rise times which decrease rapidly from 29.1 μs to 3.22 μs as the environmental temperatures decrease from 295 K to 30 K. This means the measurement is able to detect thermal relaxation time down to several microseconds scale which in other words proves the ability of quick response of the PLTR2 technique. The inset of Fig. 3.4 (b) shows the initial electrical resistances of the Ir coating before the laser pulses against the environmental temperatures. From linear fitting, the temperature coefficient of electrical resistance of Ir coating is determined. The red circles in the inset of Fig. 3.4 (b) are the relative maximum electrical resistance rises after the laser pulse heating. With the determined electrical resistance temperature coefficient and the maximum electrical resistance rises, the maximum temperature rises are calculated. Figure 3.4 (b) shows the maximum temperature rises at the back surface of the sample after the laser pulse. All these maximum temperature rises are smaller than 5 K (mainly around 4 K). In this case, the thermal property changes of GP during the measurement under a single environmental temperature should be negligible.

Figure 3.4 (c) shows the determined k_c of GP (blue triangles) from RT (295K) down to very low temperature (12.3K). The error bars show the measurement uncertainty in this work. It has been demonstrated that when the trial values change by ±10%, the simulation curves obviously deviate from the experimental data. Note that, at each environmental temperature, we take the measurements more than 100 times and get the average data. This also highly suppresses the high-frequency noises in the oscilloscope and reduce the uncertainties of our measurement results. The inset in Fig. 3.4 (c) shows volumetric heat capacities ($\rho \cdot c_p$) of PMMA, PET and graphite used in the calculation of simulation curves from literatures [116-118]. Here,

c_p of GP is taken from that of graphite, which should have no significant difference with the high purity GP studied here. The red circles and black rectangles in Fig. 3.4 (c) are the thermal conductivities of PET and PMMA [119, 120]. For comparison, k_c of a well-annealed pyrolytic graphite with well-oriented crystalline layer structure from literature is also shown in Fig. 3.4 (c) (green triangles) [121]. At RT, k_c of GP is determined as 6.08 ± 0.6 $Wm^{-1}K^{-1}$, consistent with the well-accepted value of 5.7 ~ 6.8 $Wm^{-1}K^{-1}$ of graphite [19, 20]. In the range of 295K to 200K, k_c of GP and graphite are close and when temperature goes below 200K, k_c of GP is getting smaller than that of graphite. At 80K, k_c of GP and graphite will reach their peak values and will decrease rapidly as temperature goes much lower. This k_c variation against temperature can be explained by the behavior of defect-phonon scattering and will be detailed latter.

It is well known that electrons have negligible contribution to the thermal transport in graphene or graphite and the thermal transport ability is governed by the occupied phonon modes and phonon scattering. At relatively high temperatures (higher than 180.5K, the *c*-axis Debye temperature corresponding to the cut-off frequency at 4 THz [122]), the density of occupied phonon modes is almost constant. The thermal conductivity is limited by the phonon scattering including Umklapp phonon-phonon scattering (U-scattering), phonon-boundary scattering and phonon-defect scattering. As temperature goes down, lattice vibrations get weaker, the U-scattering is correspondingly less activated but still dominates, which leads to the increase of k_c. When temperature is getting lower from 180.5K, the occupied phonons modes start reducing but slightly, the U-scattering keeps getting weaker, the phonon-boundary and phonon-defect scattering start to dominate. That is why k_c of GP and graphite keeps

increasing from about 295 K to 80 K but starts to deviate from each other at about 200 K due to their different domain sizes and defect levels. As temperature goes down from 80 K and approaches 0 K, k_c decreases dramatically due to the large decreasing of phonon occupation at extremely low temperatures. The behavior of the phonon transport of GP and graphite along the *c*-axis will be detailed in the following section.

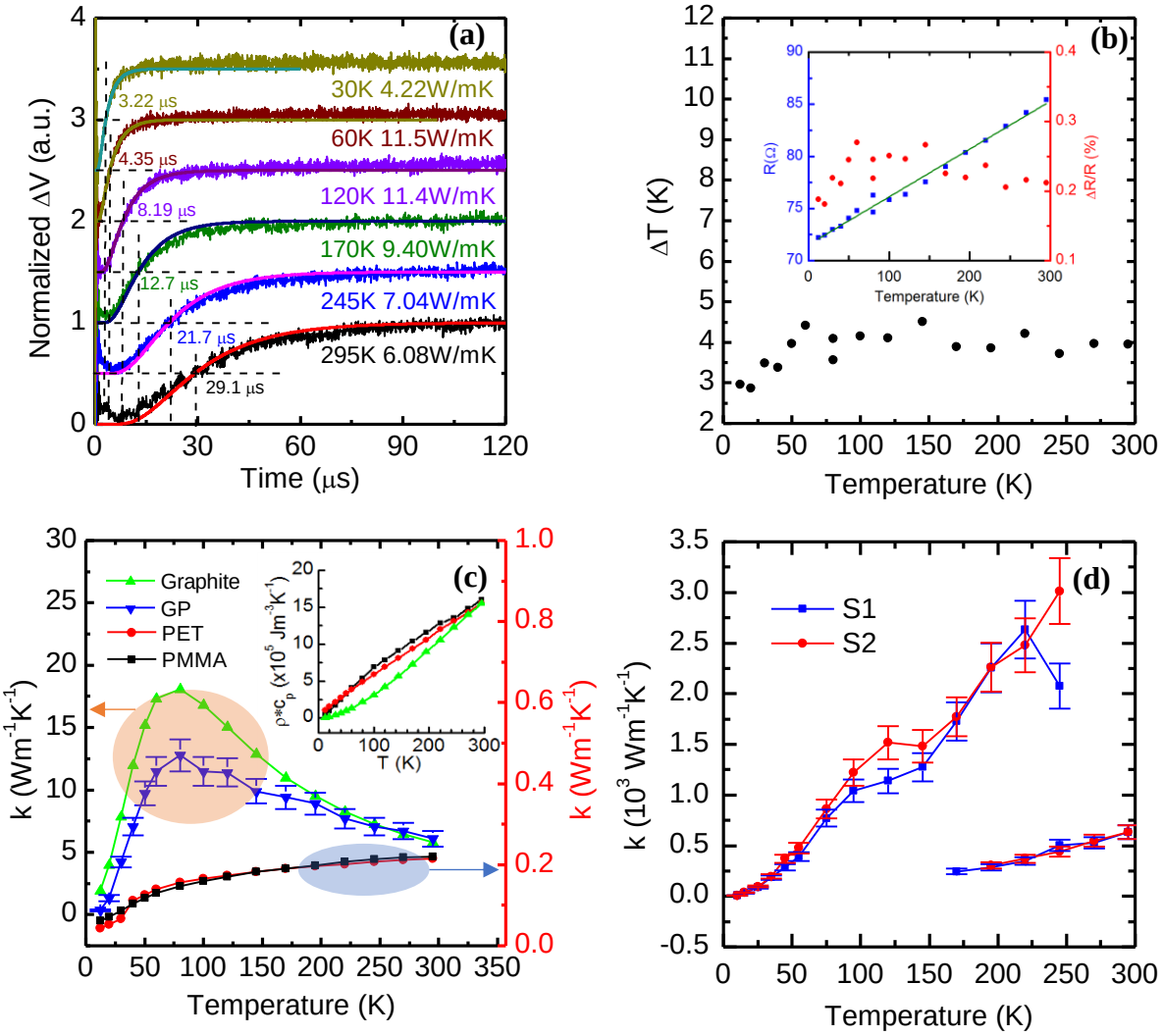

Figure 3.4 PLTR2 measurement results. (a) Normalized rising curves and the half rise time at several of our environmental temperatures. Also shown are the best fitting curves from the numerical calculations and the fitted k_c at these temperatures. (b) The maximum temperature rises at the back surface after the laser pulse irradiation. The inset shows the initial electrical resistances and the maximum relative electrical resistance rises of the Ir coating against temperature. (c) The fitted k_c of GP against temperature. Also shown are the thermal conductivities of PMMA,

PET and Graphite from literatures. The inset shows the volumetric heat capacity of PMMA, PET and graphite used in the fitting process. (d) In-plane thermal conductivity of GP characterized in our recent work [66].

Figure 3.4 (d) shows the measured k_a of GP against temperature in our recent work [66]. From Fig. 3.4 (c) and (d) we can see when the temperature is not too low, k_a is more than two orders of magnitude larger than k_c, which is consistent with the large anisotropy of pristine graphite. When temperature is getting lower from 80 K to 0 K, both k_a and k_c continue decreasing and follow similar trend with that of the specific heat [123]. This indicates that in this temperature range the dominating scattering mechanisms are the boundary and defect scattering, but the thermal transport ability is mainly controlled by the density of phonon modes occupation.

To confirm the accuracy of the PLTR2 measurement results, k_c of GP is studied by using the PT technique at RT. The experimental setup is the same as that on the β-W/Gr samples as shown in Fig. 2.4 (a). Figure 3.5 (a) shows a brief schematic of how the PT measurement works on the GP sample. The sample is heated by a modulated laser beam and thermal radiation occurs at the front surface of the sample. The thermal radiation signal is collected by an infrared detector and pre-amplified and directed to a lock-in amplifier. The phase shifts between the incident laser beam and the thermal radiation signals are then extracted. The thermal transport properties of the sample strongly affect the thermal radiation signals and thus can be determined through the fitting process of the extracted phase shifts. In this work, the modulated laser frequency ranges from 200 Hz to 4000 Hz. The lateral dimension of the sample for the PT measurement is about 1×1 mm^2, much smaller than the laser spot size (about 4×8 mm^2). In this case, we can safely assume that the front surface of the

sample is uniformly heated and thermal transport in the sample is 1D in the cross-plane direction. Details of the PT technique and the 1D heat transfer model is detailed in Chapter 2.

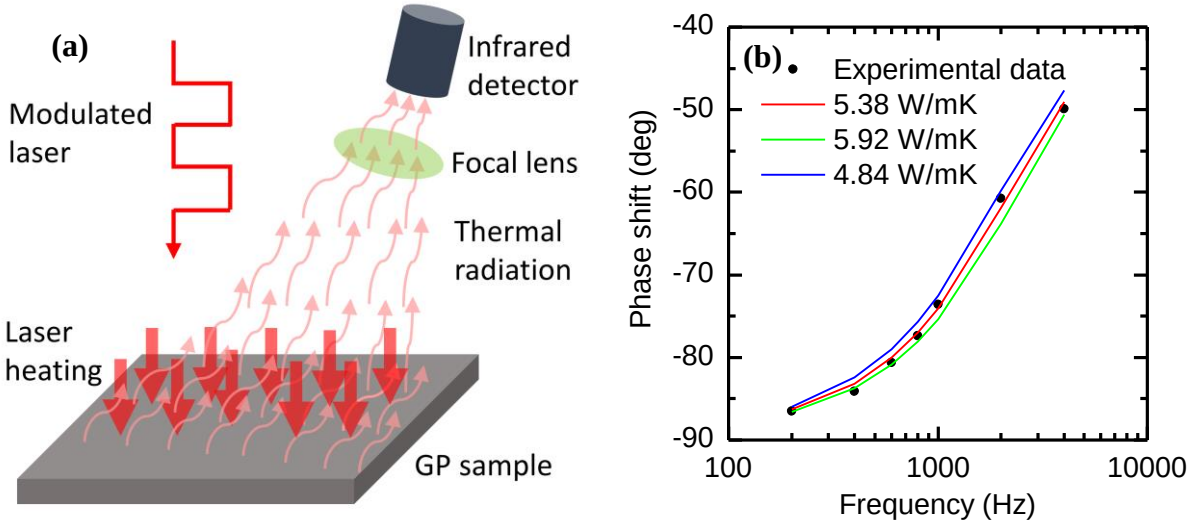

Figure 3.5 k_c measurement by the PT technique (a) schematic of the PT technique (b) phase shifts fitting to extract k_c of GP at RT

Not like the study on the β-W/Gr samples in Chapter 2, the physical model here is much simpler, only one layer of GP, with no interface resistance from substrate or between different films. The fitting process is conducted by using the program described in Chapter 2. The thickness of the sample for the PT measurement is 21.9 μm, consistent with that in the PLTR2 measurement, considering the uncertainty in the thickness measurement. The density and heat capacity are taken from that of graphite as in the PLTR2 measurement. The only unknown parameter is k_c of GP, which is what we are interested in and is extracted from the least square fitting process of the phase shifts. Figure 3.5 (b) shows the fitting results, from which we can see the best fitting curve (red) and the experimental data (black circles) match well with each other. Also shown in Fig. 3.5 (b) are the calculated theoretical phase shifts when k_c changes by 10% (green and blue curves). We can see these two curves deviate clearly from the best fitting

one and the experimental data. Therefore, we can conclude that, k_c of GP is 5.38 ± 0.54 $Wm^{-1}K^{-1}$ at RT, with an uncertainty of 10%. This value is close to 6.08 ± 0.6 $Wm^{-1}K^{-1}$ determined by the PLTR2 technique. This PT measurement on GP at RT helps verify the accuracy of the PLTR2 measurements. Like the classical laser flash method described before, the PT technique also cannot be used for cryogenic measurement since at very low temperatures, the thermal radiation from the sample surface has a very long wavelength (sub-mm) while our thermal radiation detector only detects radiations at a few μm wavelength. So, the PLTR2 technique is adopted for the cryogenic measurement.

3.3 Thermal reffusivity and structure domain size

3.3.1 Low-frequency phonons-dominated thermal transport along the *c*-axis

It is well accepted that thermal transport in graphene and graphene-based materials is dominated by phonons. [124, 125] This also holds true for GP. According to the structure study by XRD, XPS, SEM and Raman technique, the GP sample is composed of highly purified and highly ordered graphene flakes. Figure 3.6 (a) shows the schematically cross-plane view of GP, where the graphene flakes are highly ordered. The interlayer spacing is determined at 3.35 Å from the XRD study, the same as that of pristine graphite. Figure 3.6 (b) shows a schematic of the graphene flakes in our sample, which contains 5-6 layers of graphene as determined by the Raman study. In this case, thermal transport in GP is studied with reference to the phonon transport in graphite.

Phonon dispersion of monolayer graphene has been extensively studied and can provide the most information about phonon transport behaviors in graphene [126-130]. For monolayer graphene, as there is only one layer of carbon atoms connected with strong sp^2

bonds, thermal transport is two-dimensional (2D) from contribution of the whole phonon branches. While for graphite, the phonon dispersion is kind of different [17, 131-133], considering the weak Van der Waals force among layers. Figure 3.7 (a) shows the reproduced phonon dispersion of graphite from Nichlow's work [17], both in the Γ-A and Γ-M directions. The phonon modes are doubly degenerate at relatively high frequencies due to weak coupling among layers. The 'prime' (LO′ or ZO′) indicates that the two equivalent atoms in a layer vibrate in phase, but with a phase difference of 180° with respect to the two atoms in the neighboring layer [131]. Compared with phonon dispersion in monolayer graphene, the 2D thermal transport in graphite is only valid till some low-bound cut-off frequency. Below this frequency, strong energy coupling with the cross-plane phonon modes appears and heat starts to propagate in all directions, which reduces the contribution from these low-frequency phonon modes to heat transport along basal planes to negligible values [15].

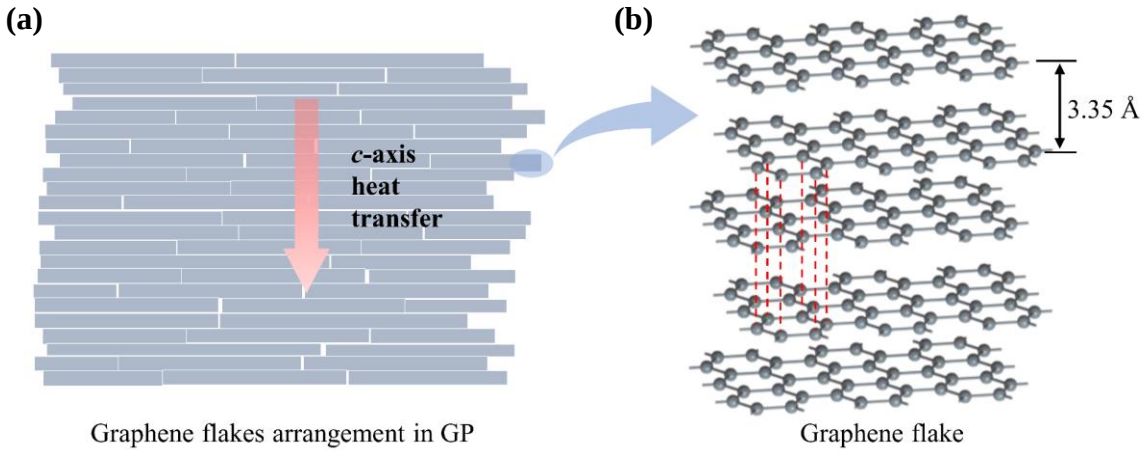

Figure 3.6 Schematic of our GP sample (not to scale). (a) Graphene flakes arrangement in the GP sample. (b) AB stacking of graphene sheets in the graphene flakes.

From the phonon dispersion in Fig. 3.7 (a), there is a physically reasonable reference frequency for the on-set of cross-plane coupling (4 THz), which is the ZO′ phonon branches at the Γ point. Figure 3.7 (a) also shows that most of the phonon branches in the (001) plane are all long-wavelength phonons with frequencies under 4 THz. There are also optical phonon branches at about 41 THz and 47 THz. However, these high-frequency phonons have small phonon group velocities with very narrow frequency ranges. Besides, phonons obey the Bosons-Einstein distribution as $\langle n \rangle = 1/\left[\exp\left(\hbar\omega / k_B T\right) - 1\right]$, where $\langle n \rangle$ is the particle numbers in the quantum state, $\hbar$ the Planck's constant, k_B the Boltzmann constant and ω the phonon frequency. From this equation we can see that the phonon numbers are much smaller at high phonon frequencies. For example, at 41 and 47 THz, $\langle n \rangle$ correspond to values of 1.27×10^{-3} and 4.78×10^{-4}, respectively, about three orders of magnitude smaller than 1.09 at 4 THz. In this case, the contribution of these high frequency phonons to thermal transport can be negligible. Thus, we can approximately claim that the thermal transport along the *c*-axis is only from contribution of low-frequency phonons under 4 THz.

The phonon thermal conductivity (k_p) can be written as [15]:

$$k_p = \sum_j \int C_j(\omega) \upsilon_j^2(\omega) \tau_j(\omega) d\omega \tag{3.2}$$

where C_j is the contribution to heat capacity from the *j*th branch; $\upsilon_j = d\omega_j / dq$ the phonon group velocity of the *j*th branch; τ_j the phonon relaxation time. The summation is performed over phonon branches *j*, which includes one LA and two TA in *c*-axis.

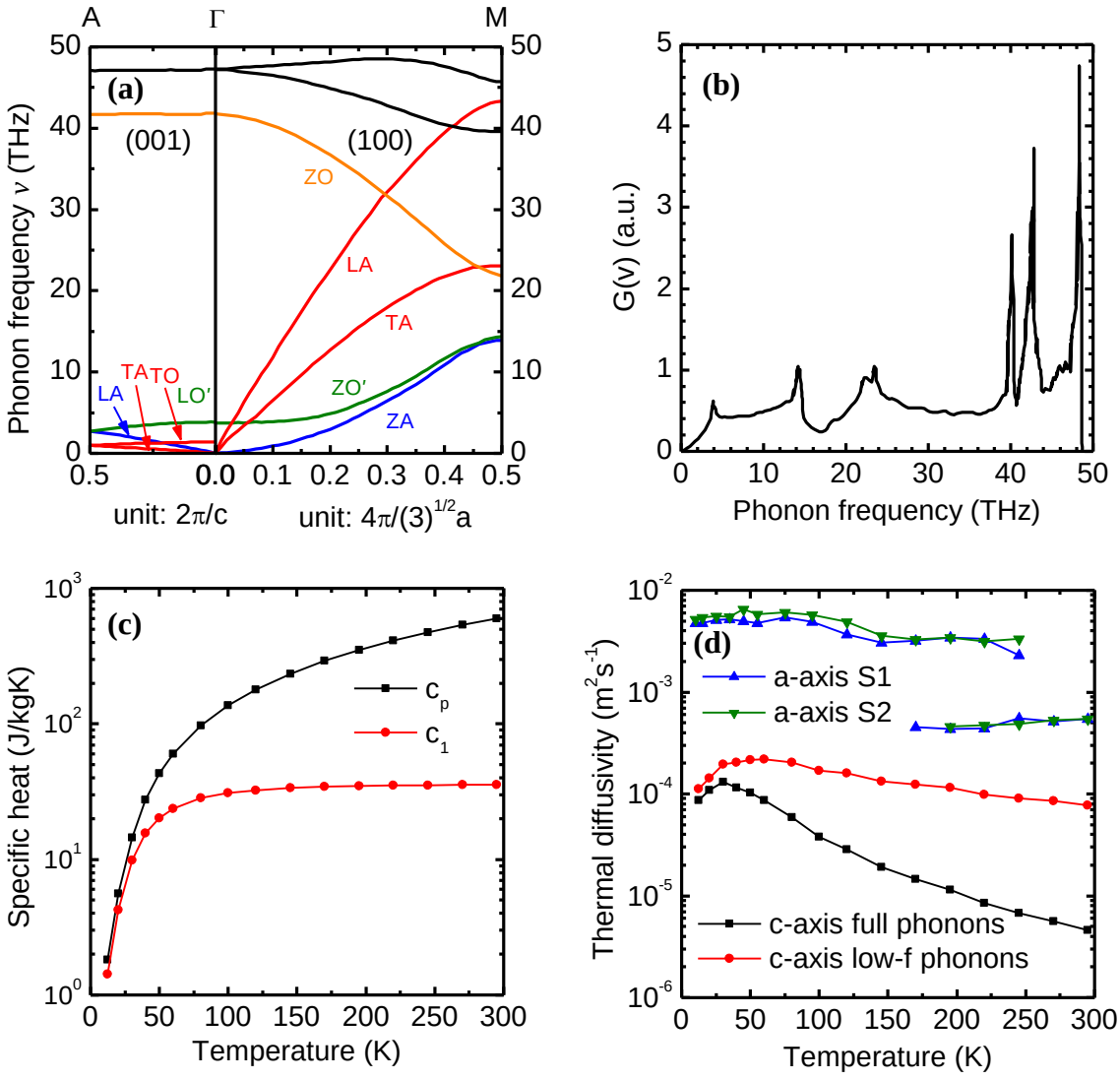

Figure 3.7 Calculation from phonon dispersions. (a) Phonon dispersions of graphite in the (001) and (100) directions [17]. (b) Density of state of phonons of graphite [17]. (c) Specific heat (c_1) calculated from only low-frequency phonons that sustain *c*-axis heat conduction and specific heat (c_p) calculated from the whole phonon branches. (d) Cross-plane and in-plane thermal diffusivities of GP against temperature calculated in this work and in our previous work, respectively [66].

From the (001) plane in Fig. 3.7 (a) the phonon group velocities $\underline{\upsilon_{LA}}$ and υ_{TA} are calculated at 1960 m/s and 700 m/s, respectively. The average phonon group velocity (υ) can be calculated as $3/\upsilon = 1/\upsilon_{LA} + 2/\upsilon_{TA}$ [134]. Thus, we have υ = 890 m/s along the *c*-axis. The

phonon MFP (l) is related to the relaxation time as $l = \upsilon\tau$. As mentioned before, the phonon relaxation time is from various scattering mechanisms including U-scattering, phonon-boundary scattering and phonon-defect scattering. According to the Matthiessen's rule, the limitation of thermal transport from these scattering mechanisms are additive, which can be expressed as the following equation:

$$\frac{1}{\tau} = \frac{1}{\tau_U} + \frac{1}{\tau_{boundary}} + \frac{1}{\tau_{defects}}, \qquad or \qquad \frac{1}{l} = \frac{1}{l_U} + \frac{1}{l_{boundary}} + \frac{1}{l_{defects}}. \tag{3.3}$$

As temperature decreases, U-scattering weakens which leads to the increase of τ_U. As temperature approaches 0 K, the $1/\tau_U$ or $1/l_U$ term vanishes, leaving only the boundary and defect scattering terms.

Phonons are quantized particles representing lattice vibrations. Lattice vibrations are directly related to atomic interactions. Strictly speaking, the cross-plane atomic interactions directly lead to *c*-axis heat conduction. This heat conduction will directly exchange energies of the phonons involving cross-plane atomic interactions. Here we introduce the anisotropic phonon heat capacity concept: C_1 and C_2. C_1 is the volumetric heat capacity of phonons involving cross-plane atomic interactions and is termed *c*-axis heat capacity, although it is a scalar. C_2 is the volumetric heat capacity of phonons involving in-plane atomic interactions, which should be close to that of monolayer graphene. Under this theory, in our experiment the thermal transport along the *c*-axis can be interpreted as a two-step process. As the cross-plane only supports energy coupling among low frequency phonons, energy absorbed by the large part of high-frequency phonons in the upper layers should first be transferred to the low-frequency phonons through in-plane atomic interactions in the same layer and then to the down

layers through cross-plane atomic interactions. This two-step process can be described by the following equations:

$$\frac{\partial C_1 T_1}{\partial t} = k_c \cdot \frac{\partial^2 T_1}{\partial z^2} + \dot{Q} - G \cdot (T_1 - T_2), \tag{3.4a}$$

$$\frac{\partial C_2 T_2}{\partial t} = G \cdot (T_1 - T_2). \tag{3.4b}$$

Here T_1 and T_2 are the temperatures of cross-plane and in-plane phonons, G in-plane and cross-plane phonon energy coupling coefficient. The energy exchange among C_1 and C_2 is very fast, so most of the time C_1 and C_2 are in equilibrium. But in fact they are involved in heat conduction in two different directions.

The volumetric heat capacity can be calculated by using the following equation:

$$C = \sum_j \int_0^{\omega_D} g(\omega) k_B \left(\frac{\hbar\omega}{k_B T} \right)^2 \frac{e^{\hbar\omega/k_B T}}{\left(e^{\hbar\omega/k_B T} - 1 \right)^2} d\omega \tag{3.5}$$

among which, ω_D is the upper cut-off frequency for each phonon branch; $g(\omega)$ the density of state of the phonon branches. Figure 3.7 (b) shows the reproduced density of state of phonon branches in graphite from Nichlow's work [17]. As described before, the upper cut-off frequencies for the phonon branches are no higher than 4 THz along the *c*-axis. Here, we take ω_D=4 THz and calculate the heat capacity from contribution of low-frequency phonons along with temperature from 12.3 K to 295 K. However, this calculated heat capacity (C) does not involve in *c*-axis heat conduction all the way as it has an acoustic phonon branch that contributes almost equally in three directions. As shown in Fig. 3.7 (a), the LA branch in the (001) direction corresponds to the ZA branch in the (100) direction in terms of lattice vibration direction. The wavevectors of this phonon branch have comparable components in the (100)

and (001) directions under 4 THz. This means this phonon branch contributes equally in the 3D structure and lead to a factor of 1/3×1/3=1/9 in the heat capacity for cross-plane heat conduction. The two TA phonon branches in the (001) direction correspond to the LA and TA branches in the (100) direction in terms of lattice vibration direction. The wavevectors of these two branches have negligible components in the (100) direction under 4 THz, meaning the phonons will mainly propagate in the *c*-axis direction. This leads to a factor of 2/3 in the heat capacity for cross-plane heat conduction. Thus, we have a factor of 7/9 in the heat capacity that contributes to the thermal transport in the cross-plane direction which can be expressed as $C_1=7/9 \cdot C$. In this case, a modified 1D kinetic theory ($k_c=C_1vl$) is used for the *c*-axis thermal conductivity of GP.

The calculation results of the specific heat are shown in Fig. 3.7 (c), from which we can see the *c*-axis specific heat (c_1, corresponding to C_1) increases from 1.42 $Jkg^{-1}K^{-1}$ at 12.3 K and reach the maximum value of 35.7 $Jkg^{-1}K^{-1}$ at near 180 K (corresponding to the cut-off frequency of 4 THz) and then stay almost constant as temperature increases. For comparison, the total specific heat (c_p: black rectangles) are also calculated by using Eq. 3.5 with the cut-off frequency of about 48 THz from the in-plane LA phonon branches, which corresponds to a Debye temperature of about 2300 K. The calculated total specific heat increases from 1.83 $Jkg^{-1}K^{-1}$ at 12.3 K to 601 $Jkg^{-1}K^{-1}$ at 295 K and will keep increasing until the temperature reaches the Debye temperature. This calculated total specific heat is close to the well-accepted specific heat of graphite [118], which in other words proves the accuracy of the calculation. The discrepancies come from the ignorance of contribution from optical phonon branches and the errors during reproducing the density of state of phonons [as shown in Fig. 3.7 (b)].

According to the recent MD simulations of Wei *et al*. [25], the defect-free k_c of bulk graphite is 11.6 $Wm^{-1}K^{-1}$ at 300 K. With the calculated specific heat and average phonon group velocity, the *c*-MFP is calculated as 165 nm at RT based on our modified 1D kinetic theory. The calculated *c*-MFP is a little larger than 146 nm determined by Wei *et al*. [25] in the MD simulations, but still proves the accuracy of our treatment of the phonon modes contribution to thermal transport along the *c*-axis. With the fitted k_c from the PLTR2 measurements, the cross-plane thermal diffusivity (α_c) of GP is calculated by $\alpha_c = k_c / C_1$. The red circles in Fig. 3.7 (d) shows the calculation results based on the *c*-axis heat capacity (C_1) while the black rectangles (macroscale thermal diffusivity) show those with the total heat capacity. Also shown in Fig. 3.7 (d) is α_a of GP from our recent work [66]. We can see that α_c calculated by using C_1 is much larger than those calculated with the total heat capacity, indicating the thermal transport response rate is larger than we used to think. Another interesting observation in Fig. 3.7 (d) is that the red curve is parallel to the blue and olive ones at not-too-low temperatures, meaning thermal diffusivities of GP in the in-plane direction have a relatively constant ratio (about 30) to those in the cross-plane direction against temperature. This anisotropy of thermal diffusivity is one order of magnitude smaller than that of thermal conductivity (around 300).

3.3.2 Defect-free *c*-MFP uncovered by the thermal reffusivity theory

The thermal conductivity defines how well a material conducts heat while the thermal diffusivity defines how fast the material responds to thermal impulse. Here we use another parameter, the thermal reffusivity, reciprocal of the thermal diffusivity, to study the phonons contribution to thermal transport in GP along the *c*-axis. The thermal reffusivity was first defined by Xu *et al*. [135] in our lab to characterize the phonon thermal resistivity of DNA and

has been successfully used in investigating the defect level and structure domain size in other materials including graphene foam [136] and ultrahigh molecular weight polyethylene (UHMWPE) [137]. Like thermal diffusivity, thermal reffusivity eliminates the temperature-dependent heat capacity involved in thermal conductivity and is solely determined by the phonon propagation and scattering in the material. With the modified kinetic theory described before, thermal reffusivity of cross-plane phonons is simply expressed as the following equation:

$$\Theta = \frac{C_1}{k_c} = \frac{1}{\upsilon l} \ . \tag{3.6}$$

Combing with Eq. 3.3, we have $\Theta = \upsilon^{-1}(l_U^{-1} + l_{boundary}^{-1} + l_{defects}^{-1}) = \Theta_0 + \Theta_i$ where Θ_0 is the boundary and defect scattering induced thermal reffusivity and Θ_i is the U-scattering induced thermal reffusivity. As described before, when temperature goes down and approaches 0 K, U-scattering vanishes and Θ_i goes to zero. Therefore, the residual thermal reffusivity (Θ_0) at the 0 K limit can help reveal the structural domain size and defect level of the material.

The role of Θ in thermal transport is similar to that of electric resistivity in metals. If there is no defect, Θ and ρ should approach zero as temperature goes down to 0 K. If the defects in the materials have scattering effect, when temperature goes to 0 K, Θ and ρ will have finite residual values. The black circles in Fig. 3.8 (a) show the calculated Θ of GP in the cross-plane direction against temperature. We can see Θ decreases as temperature goes down and reaches almost a specific value at lower temperature, just as predicted by the thermal reffusivity theory. The mechanism behind the two to three rising values at very low temperature are mainly due to the nonlinear ρ of Ir coating along with temperature at very low temperatures. This

nonlinearity is induced by the very low phonon population and its strong nonlinear correlation with temperature in Ir coating. This dominates the electron scattering behavior at low temperatures and how ρ varies with temperature. In this case, the temperature coefficient of ρ of Ir coating at temperature lower than 50 K is getting smaller. Especially at temperature lower than 30 K, this coefficient is much smaller than that at high temperatures. This means the real temperature rise is indeed much faster than the voltage or electrical resistance rise observed in the experiment. Therefore, k_c of GP is underestimated in the fitting process, which will finally lead to the overestimation of thermal reffusivity. Note that, this overestimation is getting more remarkable at extremely low temperatures due to the continuing decrease of the temperature coefficient of ρ. In addition, at very low temperatures, the ratio of Θ of GP in the total Θ of the GP/PMMA/PET multilayered films will get much smaller where small differences in the experimental data or the known parameters would lead to much larger deviations in the fitting results. Our numerical calculations show that the fitting curves in this temperature range are not sensitive to the trial values of k_c and the uncertainties of k_c in this range may be as large as 50%.

From the exponential fitting [red curve in Fig. 3.8 (a)], Θ_0 of GP is determined at 4809 sm^{-2}, taking 37% of Θ at RT. Using Eq. 3.6, with v=890 m/s, c-MFP is calculated as 234 nm at the 0 K limit, which is only induced by the defect and boundary scattering and should be smaller than the crystallite sizes of GP in the cross-plane direction. The blue triangles and the green curve in Fig. 3.8 (a) show the thermal reffusivity and corresponding exponential fitting of the well-annealed pyrolytic graphite from literature [121]. Here, Θ_0 of this graphite is determined at 2994 sm^{-2}, taking only 22% of Θ at RT. This proves the better structure and low

defect level in the graphite than in our GP sample. Accordingly, *c*-MFP is calculated as 375 nm at the 0 K limit, which is close to the 404 nm grain size calculated from the TEM images in the most recent experimental work by Zhang *et al*. [27], and is also consistent with the estimated *c*-MFP spectrum (100~600 nm) at very low temperature in the same work. The magenta and olive rectangles in Fig. 3.8 (a) shows the experimental results of the in-plane thermal reffusivity of GP measured in our recent work for comparison purpose. The in-plane MFP limited by defects and boundaries or the crystallite size is estimated as 1.68 μm [66]. The estimated *c*-MFP or cross-plane crystallite size is less than one order of magnitude smaller than that in the in-plane direction, which is seemingly inconsistent with the large anisotropy in thermal conductivity of graphite (around 300). This comparison, however, indicates that the large anisotropy in thermal conductivity is not mainly due to the strong scattering mechanisms induced by small cross-plane crystallite size. Based on Eq. 3.6, the sample *c*-MFP of GP is calculated against temperature. Also by subtracting Θ_0 from Θ, Θ_i is obtained, from which the defect-free k_c and *c*-MFP of GP are calculated. The defect-free k_c of GP is calculated at 9.67 $Wm^{-1}K^{-1}$ at RT, close to 11.6 $Wm^{-1}K^{-1}$ of graphite from the previous MD simulations [25]. The defect-free *c*-MFP is 138 nm at RT and would increases to infinite values as temperature decreases and approaches 0 K as shown in Fig. 3.8 (b). This is because we eliminate the extrinsic scattering from defects and boundaries and the U-scattering will also vanish at extremely low temperatures. Also shown in Fig. 3.8 (b) is the sample *c*-MFP which increases as temperature decreases but reach a relatively constant value at extremely low temperatures due to the defect and boundary scattering.

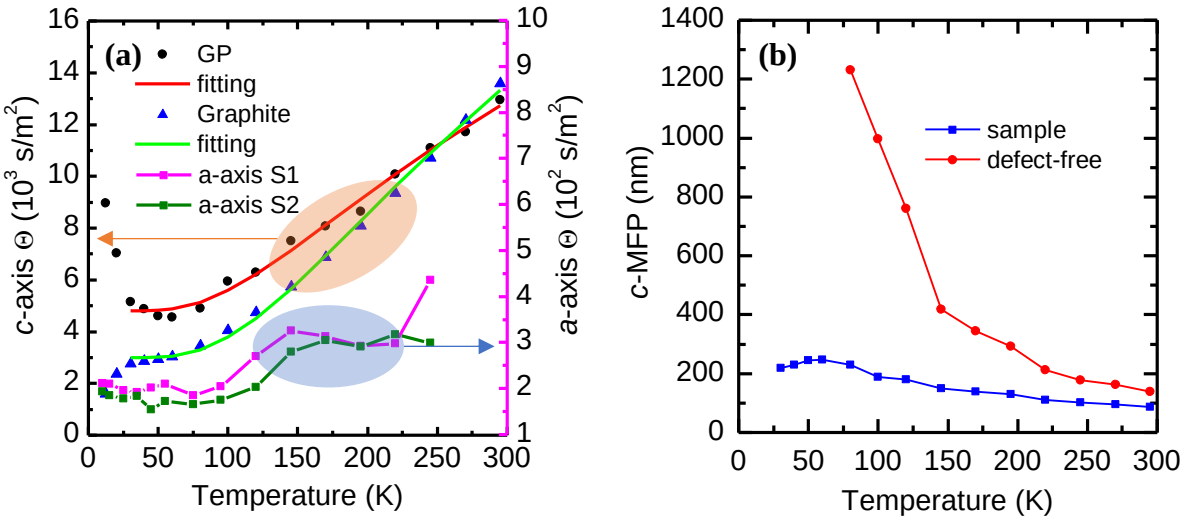

Figure 3.8 Thermal reffusivity and *c*-MFP. (a) *c*-axis thermal reffusivity of GP and graphite calculated in this work and *a*-axis thermal reffusivity of GP calculated in our previous work [66]. Also shown are the exponential fitting curves to the *c*-axis thermal reffusivity that are used to extract the residual thermal reffusivity. (b) Sample and defect-free *c*-MFPs of GP.

The determined sample and defect-free *c*-MFPs of GP (86.7 and 138 nm, respectively) at RT are orders of magnitude larger than those derived from the classic kinetic theory [21]. The problem with the classic kinetic theory is that the expression is based on the isotropic model and assume that the heat capacity is contributed equally by phonon modes over the entire Brillouin zone. While in fact only low-frequency phonons under 4 THz are supported in the cross-plane direction and contribute to heat capacity and thermal transport in that direction [138]. Our modification of the kinetic theory takes into account the high anisotropy of phonon dispersions and calculates only the contributions of cross-plane phonon modes to the heat capacity. This simple treatment can help explain the long phonon propagation distances yet small thermal conductivity of GP along the *c*-axis. Our extracted defect-free *c*-MFP at RT (138 nm) is consistent with the long *c*-MFP of graphite, which is estimated as 146 nm in the recent MD simulations by Wei *et al*. [25] Following experimental work by Fu *et al*. [26] even reported

a longer average *c*-MFP (204 nm) at RT by employing the 3ω measurement on graphite films of varying thicknesses. Most recent experimental work by Zhang *et al*. [27] performed the TDTR measurement on graphite films and reported a *c*-MFP in the range of 100~200 nm at RT. The extracted *c*-MFP at 0 K limit (234 nm) also serves as a good estimation of the crystallite size of GP along the *c*-axis. As mentioned in the sample characterization section, the crystallite size cannot be directly determined from the XRD measurement. This, in other words, proves that the crystallite size is in the order of several hundred nanometers which is beyond the instrument measurement range. Note the Raman spectra show that the graphene flakes contain 5~6 layers graphene, corresponding to a thickness of 1.68~2.01 nm. The determined *c*-axis structure size (234 nm) is much larger than the flake thickness, uncovering the excellent *c*-axis atomic structure order. Also, this *c*-axis structure size is much larger than the defect-free *c*-MFP (138 nm) at RT. Therefore, the effective *c*-MFP at RT is not significantly reduced but stays at a quite high level of 86.7 nm.

CHAPTER 4. *c*-AXIS THERMAL DIFFUSIVITY OF PARTIALLY REDUCED GRAPHENE PAPER AND GRAPHENE OXIDE PAPER

In this chapter, the cross-plane thermal conductivity of PRGP and GOP was first characterized from 295 K down to 12 K by employing the PLTR2 technique. Compared to GP studied in Chapter 3, both PRGP and GOP show much low cross-plane thermal conductivity. To eliminate the influence of heat capacity of different structures, the thermal diffusivity was further studied. By employing the TGA, XRD, EDS and Raman spectroscopy techniques, the chemical composition, and the layered structure of the two sample was characterized. The low thermal diffusivity of PRGP was attributed to the strong phonon scattering at the grain boundaries and defect centers, due to the small grain size and the high-level defects. For GOP, the determined interlayer spacing is very large, where direct energy coupling between graphene layers is negligible. The cross-plane thermal transport was related to the high density of functional groups between layers, which can provide weak thermal transport tunnels across the layers.

4.1 Experimental details

The PLTR2 technique is used to investigate the thermal transport properties of PRGP and GOP in the cross-plane direction. As described in Chapter 3, our PLTR2 technique is designed to overcome the challenges involved in the classic laser flash method, especially for samples with very thin thicknesses and for measurements performed under very low temperatures. In this work, An Ir coating is also used and acts as the temperature sensor. For PRGP, as a good conductor (conductivity ~ 5×10^3 Sm^{-1}) [66], we need to insert an insulting layer to isolate it from the Ir coating, just like we do for GP in Chapter 3. While for GOP, as a good isolator with extremely high electrical resistivity, there is no need to be insulated from

the Ir coating. The Ir film will be directly coated on the back surface of GOP for temperature sensing.

4.1.1 Sample preparation

The PRGP and GOP samples are purchased from ACS materials. Briefly, GOP is composed of graphene oxide flakes stacking layer by layer. PRGP is obtained by partially reducing GOP, and GP is obtained by highly reducing GOP. Thus, the structure difference among the three materials represents three typical stages in the reduction process. According to the technical data sheet, they are produced in the following process. First, the graphite oxide is prepared from graphite by using the modified Hummer's Method [52, 53]. Then a suspension of graphene oxide (GO) sheets is obtained through the sonication and exfoliation of the prepared graphite oxide [51]. The free-standing GOP is assembled in direct flow (typically by vacuum assisted flow-filtration), which can be chemically reduced to produce PRGP.

Here in the PLTR2 measurement, we use a 0.5 μm-thick PET film to separate the PRGP sample from the Ir coating. The sample preparation process is the same as that of GP described in Chapter 3. As shown in Fig. 4.1, the PRGP sample is attached to the PET film by using PMMA and the backside of PET is coated with Ir film. By feeding DC current through the Ir coating, the temperature evolution at the back surface of the multilayered sample can be detected. Silver paste is also used to enhance the electrical and thermal contacts between the Ir coating and the electrodes. The most important and challenging thing is to make sure the PRGP is well isolated from the Ir coating, which means only the Ir coating is in the electric circuit. For GOP, the sample preparation is similar but much easier. The Ir is directly coated on the back surface of the sample, no PET or PMMA film is needed.

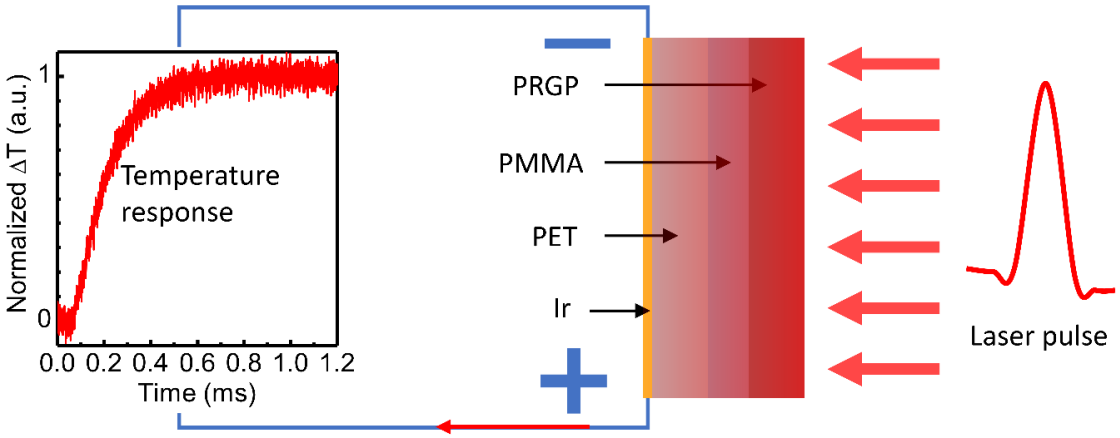

Figure 4.1 Schematic of the sample. The multilayered sample is prepared by attaching PRGP to PET films by the PMMA/toluene solution. The Ir coating is first sputtering coated on the other side of the PET film before the attachment. The Ir coating is fed with a DC current and the temperature response of the back surface of the multilayered sample after the laser pulse is detected by the electrical resistance or voltage variation of the Ir coating.

4.1.2 Structure characterization

The alignment and orientation of graphene and GO flakes in PRGP and GOP are first studied by SEM. Figure 4.2 (a) and (b) shows the cross-plane views of the two samples under 15000× magnification, respectively. The layered structure is clear, and no significant evidence of air pockets is found, ensuring that both PRGP and GOP are close to full dense. The quality and thermal stability are then investigated by using the TGA technique. Figure 4.2 (c) shows the weight loss curve (TGA: blue) and the DTG curve (red) of GOP. The mass loss up to 100 ^{o}C is due to the desorption of physically adsorbed water. The following sharp drop from about 100 ^{o}C to 300 ^{o}C with a peak at about 200 ^{o}C takes more than 30% of the original mass. This is attributed to the decomposition of labile functional groups, which have also been found in the TGA characterization of GO in the literature [55, 59, 139]. The small differences in the peak positions (200 ^{o}C, 220 ^{o}C and 230 ^{o}C, respectively) may be due to different methods in

obtaining GO from graphite. Figure 4.2 (d) shows the TGA results of the PRGP. The weight loss up to 100 ^{o}C is much less than that of GOP, indicating the PRGP contains much less water. There is also a similar sharp weight loss around 200 ^{o}C, due to the removing of the residual labile functional groups.

The structure of PRGP and GOP are then characterized by using XRD and Raman spectroscopy. Figure 4.2 (e) shows the XRD spectra of the samples. From the blue curve we can see that the major peak of GOP is at 10.52^{o}. This peak corresponds to the (002) crystal plane of GOP, from which the interlayer spacing is determined at 8.4 Å. This value is consistent with 8.32 Å at 10.6^{o} for graphene oxide from literature [140, 141]. The large interlayer spacing has been attributed to the formation of hydroxyl, epoxy, and carboxyl groups [54], especially the hydroxyl and epoxy form on the basal plane. The crystallite size is calculated at 7.1 nm, much smaller than that of GP described in Chapter 3. From the red curve of PRGP, we can see a relatively lower peak at 24.15^{o}, corresponding to the (002) plane of reduced graphene materials. The interlayer spacing is determined at 3.68 Å, about 10% percent larger than 3.35 Å of GP and graphite. This indicates that there are just a few remaining functional groups on the basal plane or among the interlayers. The crystallite size is calculated at 4.8 nm, even smaller than that of GOP. The relatively wider and lower peak of PRGP than GOP also indicates that the crystalline structure of PRGP is not as good as that of GOP.

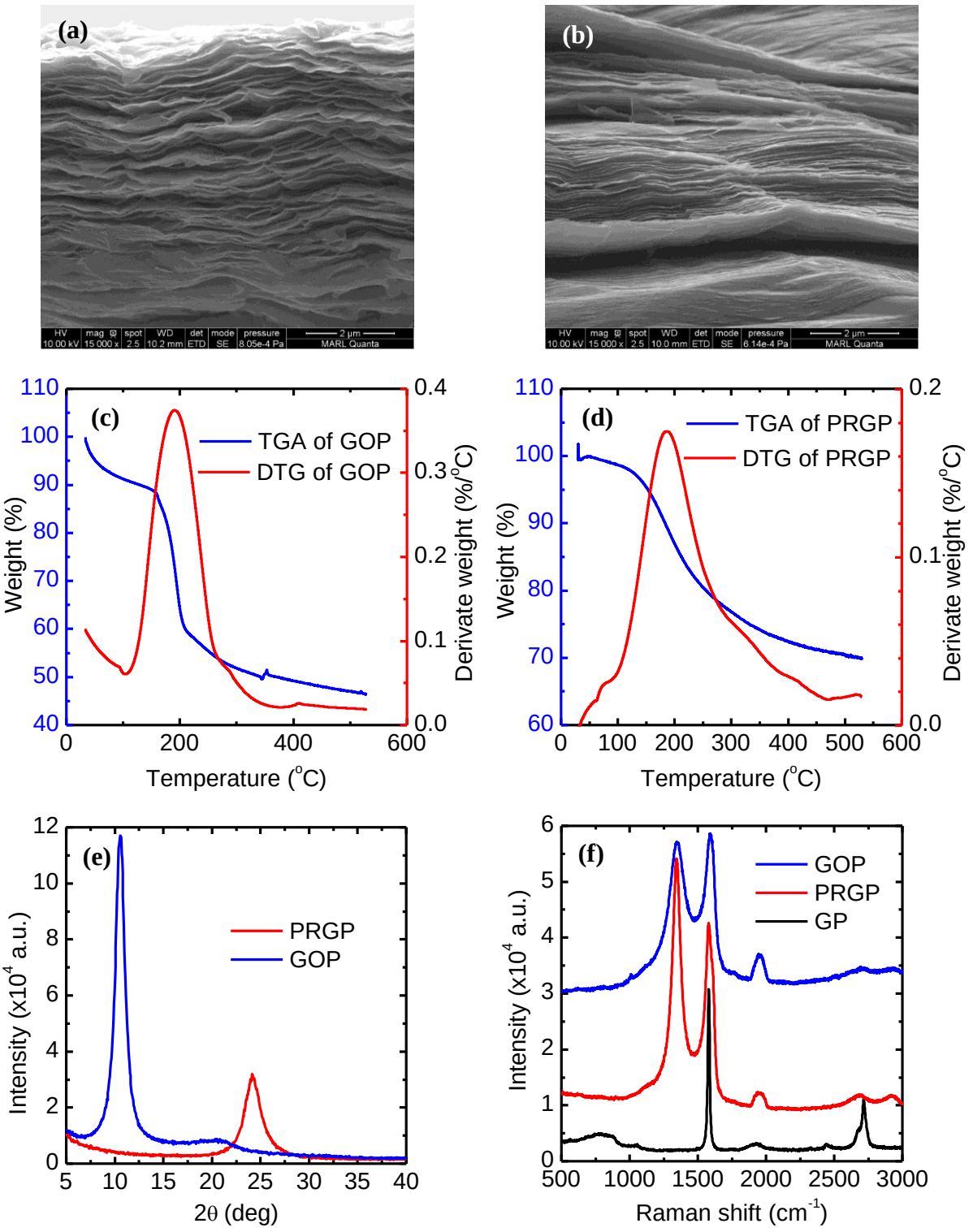

Figure 4.2 Sample characterization (a) and (b) SEM images of the cross-plane view of PRGP and GOP, respectively. (c) TGA and DTG signals of GOP; (d) TGA and DTG signals of PRGP; (e) XRD signal of PRGP and GOP; (f) Raman spectra of GP, PRGP and GOP.

Figure 4.2 (f) shows the Raman spectra of PRGP and GOP, as well as that of GP studied in Chapter 3 for comparison. We can see two intense peaks from the red curve of PRGP, where the D-band around 1345 cm^{-1} corresponds to the defects or edges scattering and the G-band around 1579 cm^{-1} corresponds to the first-order scattering of the E_{2g} mode. There are two similar peaks at 1347 cm^{-1} and 1591 cm^{-1} on the blue curve of GOP. The band intensity ratio I_D/I_G of PRGP is larger than that of GOP, which has been commonly reported for chemical reduction of GOP [54, 61, 64]. This increase of I_D/I_G ratio from GOP to PRGP suggests a further decrease in the size of sp^2 domains upon chemical reduction of GOP [64, 142]. This can be explained as the loss of carbon atoms from the graphene lattice which results in formation of defects such as vacancies and distortions, where the integrated sp^2 domains are further separated into smaller ones [59]. Further reduction is likely to induce the decrease of the I_D/I_G, due to the recovery of the sp^2-hybridized C-C bonds [55, 143, 144]. This recovery is apparent in the highly reduced GP structure studied in Chapter 3. The 2D peak of GP at about 2700 cm^{-1} is relatively sharp and intense, which is consistent with that of high-quality multilayered graphene and graphite [145]. While in GOP, this peak is very weak and is highly broadened, indicating the high defect level. In PRGP the 2D peak is still weak, but relatively higher than that of GOP, due to the better graphitization after chemical reduction. The S3 band at 2900 cm^{-1} is invisible in GP, and is getting higher from GOP to PRGP, also an indicator of better graphitization of PRGP [60].

The chemical compositions of GP, PRGP, and GOP are studied by the energy-dispersive x-ray spectroscopy (EDS), from which the atomic fractions of existing elements in these materials are determined. For GP, the atomic fraction is C (99.81%) and O (0.19%). For

PRGP, the atomic fraction is C (86.43%), O (9.93%) and I (3.65), shows relatively high ratio of O. For GOP, the atomic fraction is C (63.74%), O (35.12%), S (1.01%), and K (0.14%), indicates large amount of O in it. The EDS results are consistent with the XPS study in our previous work [66]. The different O fractions will highly influence the layered structures and thermal transport properties in the three samples.

4.1.3 Experimental setup and physical model

The PLTR2 technique is performed on PRGP and GOP in a vacuum chamber with a pressure lower than 0.6 mTorr. The experimental setup is similar to that in Chapter 3 and is shown in Fig. 4.3. The sample is held vertically on the copper substrate which is designed specifically for horizontal laser irradiation from outside. The experimental temperature is controlled by the Janis CCR system. The sample is connected to a current source and an oscilloscope, where a close circuit forms through the Ir coating. A DC current is fed through the sample and the electrical resistance and voltage variations of the Ir coating are monitored by the oscilloscope. A nanosecond laser irradiates the front surface of the sample and thermal transport occurs in the sample. The temperature evolution of the Ir coating is reflected on the variation of its electrical resistance or voltage. As shown in the inset of Fig. 4.3, the laser pulse width is about 8 ns, which is more than four orders of magnitude smaller than the thermal relaxation time of our sample in the cross-plane direction. Thus, the infinite pulse duration effect is negligible. A silicon photodiode is connected to the oscilloscope to capture the laser pulse and the position of the laser pulse in the time scale is taken as the beginning time of the thermal relaxation which is of importance in the PLTR2 model. The original laser spot size is about 3.5 cm, much larger than the lateral dimensions of the PRGP and GOP sample (with length shorter than 3 mm). Thus, we can also safely assume a uniform laser energy distribution

absorbed by the sample at the front surface (taking an optical absorption depth of 31 nm from that of graphite). Details of the experimental setup is described in Chapter 3.

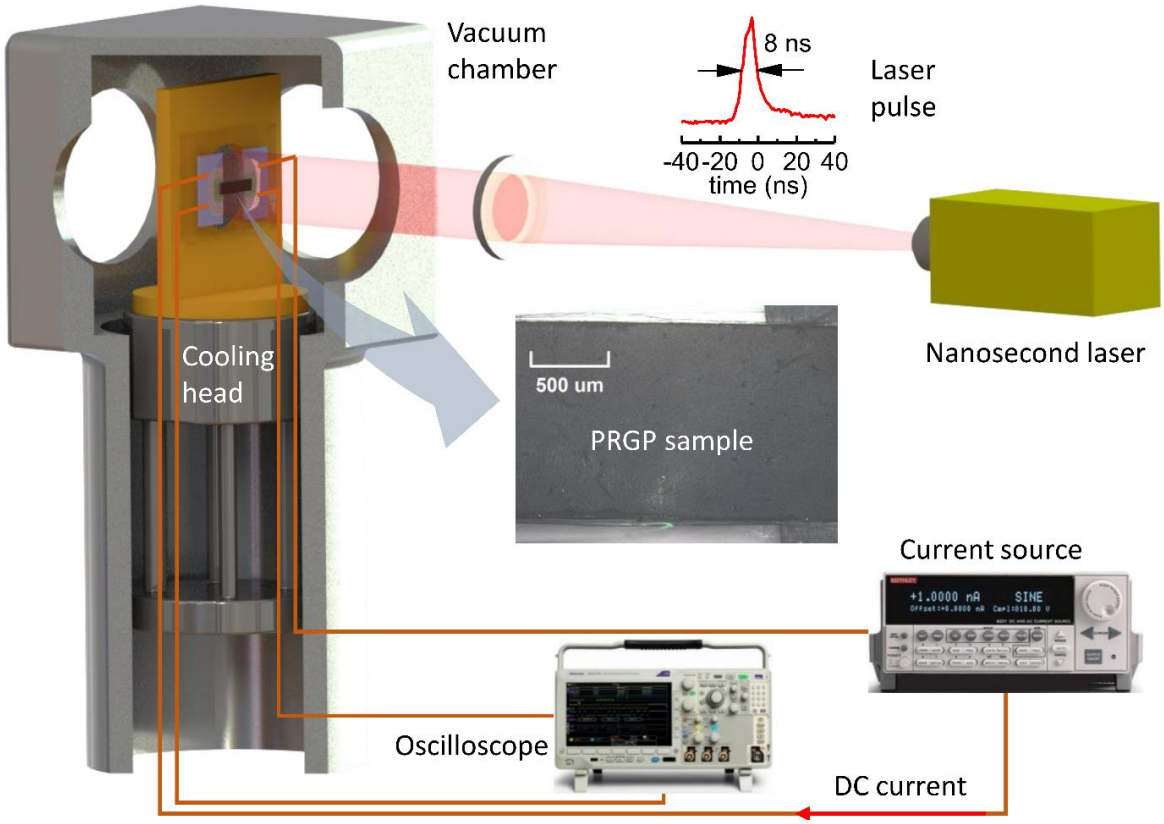

Figure 4.3 Schematic of the experimental setup (not to scale). The insets show the pulse laser duration (left-up) and the microscope image of the multilayered PRGP/PMMA/PET/Ir sample (central).

The 1D thermal transport simplification also holds true for PRGP and GOP, due to the large difference of characteristic times or characteristic lengths in the in-plane and cross-plane directions. According to our recent work [66], α_a of PRGP is no larger than 2.5×10^{-6} m^2s^{-1}, which corresponds to a characteristic thermal relaxation time t_c larger than 2.5 s. While in the cross-plane direction, t_c is no larger than 2 ms [shown in Fig. 4.4 (a)], more than 3 orders magnitude smaller than that in the in-plane direction. As for GOP, k_a and α_a has also been

characterized in our recent work [66]. The corresponding in-plane t_c is larger than 0.5 s even at very low temperatures. While in the cross-plane direction, t_c is no larger than 2 ms, still orders of magnitude smaller than that in the in-plane direction.

As described in Chapter 3, the governing equation for the 1D thermal transport in a multilayered film can be expressed as follows: [108]

$$\frac{\partial T_i(x,t)}{\partial t} = \alpha_i \frac{\partial^2 T_i(x,t)}{\partial x^2}, \text{ i = 1, 2, 3, …} \tag{4.1}$$

For GOP, as a single-layered film with no PMMA or PET attached and the thickness of Ir coating can be neglected, the governing equation can be solved by using the green's function and expressed as the following equation:

$$T(x,t) = \frac{Q}{\rho c_p L}\left[1 + 2\sum_{m=1}^{\infty} \frac{\sin(m\pi\tau_{opt}/L)}{m\pi\tau_{opt}/L} \times \cos\left(\frac{m\pi x}{L}\right) \times \exp\left(\frac{-m^2\pi^2}{L^2}\alpha t\right)\right]. \tag{4.2a}$$

At the back surface where $x=L$, the temperature evolution can be expressed by:

$$T(L,t) = \frac{Q}{\rho c_p L}\left[1 + 2\sum_{m=1}^{\infty} (-1)^m \frac{\sin(m\pi\tau_{opt}/L)}{m\pi\tau_{opt}/L} \times \exp\left(\frac{-m^2\pi^2}{L^2}\alpha t\right)\right]. \tag{4.2b}$$

When normalizing from the initial temperature to the maximum temperature, we have the normalized temperature response of the back surface of the sample as:

$$T^*(L,t) = 1 + 2\sum_{m=1}^{\infty} (-1)^m \frac{\sin(m\pi\tau_{opt}/L)}{m\pi\tau_{opt}/L} \times \exp\left(\frac{-m^2\pi^2}{L^2}\alpha t\right). \tag{4.2c}$$

As described in Chapter 3, the electrical resistance of Ir is linearly proportional to the temperature and can be expressed as $R = (\rho_0 + \gamma \cdot \Delta T)(l / A_c)$, especially in a small temperature range. Here R is the electrical resistance of the Ir coating, ρ_0 initial electrical

resistivity at the environmental temperature, ΔT temperature rise from the environmental temperature, l length of the sample, A_c cross-section area of the Ir coating. When normalizing R from the initial value (R_0) before the laser pulse to the maximum value (R_m) after the laser pulse, we have

$$R^* = \frac{R - R_0}{R_m - R_0} = \frac{\Delta R}{\Delta R_m} = \frac{\Delta T}{\Delta T_m} = T^*. \tag{4.3}$$

This means the temperature response of the back surface of the sample is mimicked by the electrical resistance or voltage evolution, both after normalization. In the experiment, the electrical resistance or voltage evolution curve can be obtained by the oscilloscope (as shown in Fig 4.1). Thus for a single-layered sample (GOP), α_c can be directly calculated from the half rise time of the response curve as $\alpha = 1.37L^2/\pi^2 t_{1/2}$, according to Eq. 4.2 (c) [106]. Then k_c can be calculated by $k = \alpha \cdot \rho \cdot c_p$ with the given density and specific heat of the material.

For multilayered PRGP/PMMA/PET sample, analytical solution is very complicated. The half rise time is related to the thermal properties of all the layers in the sample. In this case, we use the numerical method developed in Chapter 3 to simulate the 1D thermal transport and fit the extracted back surface temperature response curves with that from the experimental data, both after normalization. As described in Chapter 3, the thicknesses of the layers are key parameters in the simulation and should be determined before the PLTR2 measurement. The thickness of PRGP is 11.5 ± 0.5 μm determined by a micrometer. Also, the weight of a piece of PRGP with a lateral dimension of 3.366 × 1.895 mm^2 is measured at 142 μg with a microbalance. Thus, the density of PRGP is calculated at 1.936 ± 0.085 g/cm^3, a little smaller than the full density of pristine graphite (2.21 g/cm^3). This relatively lower density is mainly

due to the larger interlayer spacing than graphite as determined by the XRD in the last section. Another reason is the disordered alignments of the rGO flakes, which leads to large spacing among flakes and hence reduces the density of the structure. Therefore, we can conclude that the PRGP is to some extent a full density graphene-based structure. The thickness of our multilayered PRGP/PMMA/PET/Ir sample is measured at 12 ± 0.5 μm with the micrometer. The thickness of PET is taken as 0.5 μm (the production description which is also confirmed in our recent work [146]). The microbalance is used to measure the weight of the multilayered sample after the PLTR2 measurement. The total weight of the multilayered sample is determined at 102 μg. With the lateral dimensions of the multilayered sample and the Ir coating determined at 2.95×1.47 mm^2 and 2.95× 1.20 mm^2 under the microscope, the thickness of the PMMA is calculated at 0.2 μm. Similarly, the thickness and density of GOP are determined with the help of the micrometer and microbalance, which are 28.5± 0.5 μm and 1.465±0.027 g/cm^3, respectively.

The densities, heat capacities of the PMMA and PET are taken from literature. [116, 117] The heat capacity of PRGP is taken from that of graphite [118], which is always an assumption in the literature [147, 148]. To confirm this, the specific heat of our PRGP and GOP samples is measured within a Netzsch STA449F1 TDA/DSC system. The measurement is taken from 35 ^oC to 75 ^oC, which is the lowest available range in our TDA/DSC system and makes sure that the PRGP and GOP are not destructed or further reduced. The DSC results are shown in Fig. 4.4 (a), from which we can see c_p of PRGP increases linearly along with the temperature in the measurement temperature range, consistent with that of graphite [149]. Thus, we can safely extract c_p of PRGP at RT (22 ^oC), which is 776 J/g·K, and is about 10% higher

than that of graphite. Considering the uncertainty of the TGA/DSC measurement, this difference is not significant. Also shown in Fig. 4(a) is c_p of GOP determined from the DSC measurement, which also has no significant difference from that of PRGP and graphite. Thus, during the data processing in this work, c_p of PRGP and GOP are taken from that of graphite. The influence of the deviations of c_p on k_c and α_c will be discussed later. k_c of PMMA and PET are also taken from literature [119, 120, 150]. Thus, in the 1D heat transfer model of the multilayered PRGP/PMMA/PET sample, the only unknown parameter is k_c of PRGP. With these known parameters and trial values of k_c, different temperature response curves of the sample backside can be obtained. Then the least square method is used to extract the one that gives the best fit to the experimental data. For GOP, the thermal diffusivity can be directly extracted from the half rise time as described before.

4.2 Results and discussion

4.2.1 Thermal conductivity variation against temperature

The PLTR2 measurements are performed every 25 K from 295 K to 100 K, then every 20 K from 100 K to 60 K and finally every 10 K from 60 K to nearly 10 K. Denser data points collected at low temperatures is to monitor the low-temperature effects on the sample structure. For PRGP, the measurement is taken from 295 K to 12 K (down-round) and then back to 295 K (up-round) to study the influence of the low-temperature on the structure and thermal properties. Figure 4.4 (b) shows the normalized back surface temperature response curves at several of our experimental temperatures. The normalized temperature rises to the maximum value and keeps for a while before decreasing as heat dissipates in the in-plane direction. Also shown in Fig. 4.4 (b) are the corresponding best fitting curves and half rise time at the specified environmental temperatures. The theoretical curves fit the experimental ones very well. $t_{1/2}$ is

a direct indicator of how fast heat transfer is in the cross-plane direction, although it cannot be used directly to calculate thermal diffusivity of multilayered sample. Figure 4.4 (c) shows the variation of $t_{1/2}$ versus temperature, which has no significant difference from the down-round to the up-round at a given temperature, indicating the small structure change induced by the low-temperature process. $t_{1/2}$ does not decrease too much from RT to 12 K, not like the rapid decrease of GP studied in Chapter 3. This reveals the different cross-plane heat transfer behavior of PRGP and GP along with temperature, which will be detailed later in the following sections.

As described in the last section, $R = (\rho_0 + \gamma \cdot \Delta T)(l / A_c) = R_0 + \beta \cdot \Delta T$, with β the local temperature coefficient of the electrical resistance, shows a linear relationship, especially in a small environmental temperature range, as shown in the inset of Fig. 4.4 (d). Also shown in the inset of Fig. 4.4 (d) is the maximum electrical resistance (ΔR_{max}) after the laser pulse. Therefore, with β and ΔR_{max} during a single measurement, the corresponding maximum back surface temperature rise (ΔT_{max}) can be calculated. Figure 4.4 (d) shows ΔT_{max} during a single measurement of the experimental temperature, which increases gradually as temperature decreases, especially after 50 K. This is due to the decrease of β at lower temperatures (lower than 50 K) as shown in the inset of Fig. 4.4 (d). In the measurement process, to keep the lowest temperature rise while providing sufficient signal to noise ratio, ΔR_{max} is controlled at around 0.5Ω. In this case, as β is getting smaller at lower temperatures, the temperature rises should be larger. Even though, ΔT_{max} is no larger than 7 K, especially at a temperature higher than 50 K, it is smaller than 4 K. With such small temperature rises, the physical properties change during a single measurement is negligible.

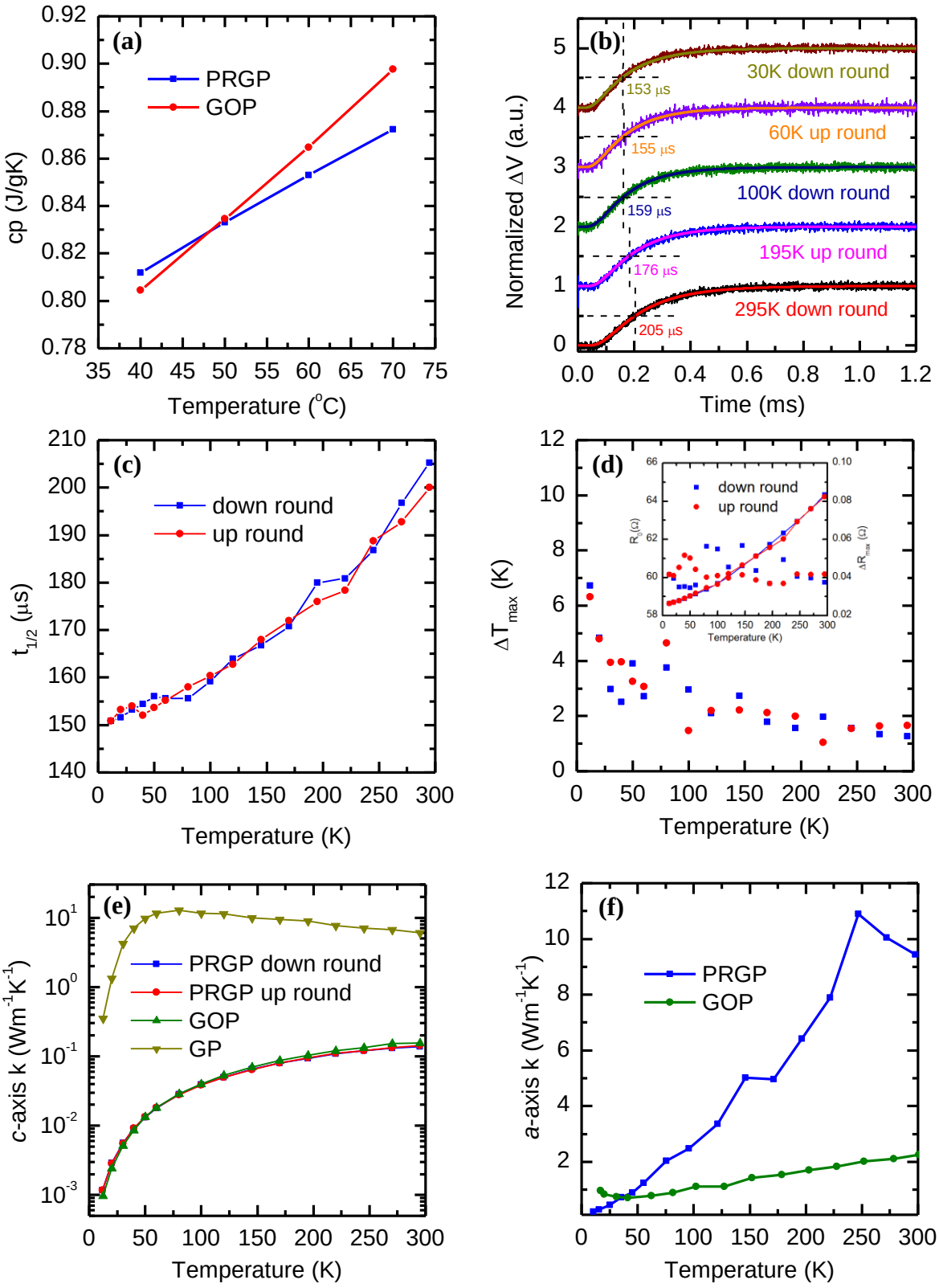

Figure 4.4 Thermal transport characterization. (a) DSC of the c_p of PRGP and GOP at near RT. (b) Normalized voltage variations and the best fitting curves at several of our

environmental temperatures for PRGP. Also shown are the half rise times at these temperatures. (c) $t_{1/2}$ versus temperature of PRGP. (d) Maximum temperature rises during a single measurement against the environmental temperature. The inset shows the initial electrical resistance and the accordingly maximum resistance change against the environmental temperature. (e) *c*-axis thermal conductivity of PRGP and GOP, as well as GP studied in Chapter 3. (f) *a*-axis thermal conductivity of PRGP and GOP determined in our previous work [66].

By least square fitting of the simulation curves to the experimental ones, k_c of PRGP is obtained at all the experimental temperatures. Figure 4.4 (e) shows the extracted k_c of PRGP from RT down to 12 K. Also shown in Fig. 4.4 (e) is k_c of GOP calculated from half rise time in the PLTR2 measurement results. For PRGP, k_c decreases from 0.14 $Wm^{-1}K^{-1}$ at 295 K to 1.2×10^{-3} $Wm^{-1}K^{-1}$ at 12 K. This k_c and temperature relationship shows kind of amorphous-like behavior and is much different from that of GP studied in Chapter 3 [also shown in Fig. 4.4(e)]. As studied in Chapter 3, k_c of GP increases from 6.08 $Wm^{-1}K^{-1}$ at 295 K to 12.8 $Wm^{-1}K^{-1}$at 80 K and then decrease rapidly to 0.35 $Wm^{-1}K^{-1}$ at 12.3K, showing a peak at around 80 K. This difference of k_c evolution with temperature is attributed to the high-level defects and structure disorders in PRGP where the thermal transport ability is mainly limited by the defect and grain boundary scattering in the full experimental temperature range. while for GP, with low-level defects, the Umklapp phonon-phonon scattering dominates at high temperatures which are overridden by the structure defects and related phonon scattering at low temperatures. For GOP, k_c decreases from 0.16 $Wm^{-1}K^{-1}$ at 295K to 9.7×10^{-4} $Wm^{-1}K^{-1}$ at 12.5 K, very close to those of PRGP.

For comparison, k_a of PRGP and GOP studied in our previous work [66] is shown in Fig. 4.4 (f). k_a of PRGP changes from 9.4 $Wm^{-1}K^{-1}$ at 300 K to 0.14 $Wm^{-1}K^{-1}$ at 15K, showing kind of decrease trend, despite the small increase from 300 K to 250 K. This small increase at

relatively high temperatures may be due to the U-scattering which will get weaker and will be overridden by the high-level defect scattering as temperature goes down. Not like the U-scattering mechanism, the defect induced phonon scattering changes little with temperature. The decrease of k_a at low temperatures is mainly due to the reduction of occupied phonon modes, which are less active at low temperatures. This reduction of occupied phonon modes is reflected on the rapid decrease of heat capacity as temperature goes down. k_a of GOP decreases from 2.15 $Wm^{-1}K^{-1}$ at 306 K to 0.73 $Wm^{-1}K^{-1}$ at 37 K which stays almost stable after 69 K with a smaller increase from 25 K.

Recent work by Renteria *et al* [71] reported a much low k_c (0.09 $Wm^{-1}K^{-1}$) of rGOP after thermal annealing treatment at 1000 ^oC, only half of its corresponding original GOP (0.18 $Wm^{-1}K^{-1}$) before annealing. Their low k_c of rGOP was attributed to the air pockets formed during the annealing treatment, by assuming that the intrinsic k_c has no change from their GOP to rGOP, which is however not usually the case. Besides, due to the large anisotropy of thermal conductivity of this rGOP (60 $Wm^{-1}K^{-1}$ in the in-plane), the Maxwell-Garnet's approximation used in their calculation could introduce large errors in the results. Not like the rGOP sample studied in Renteria's work, the PRGP in the present work is of full density. The SEM images of the cross-section view in Fig. 4.2 (a) also shows a fully layered structure with no significant evidence of air pockets involved in the material. Thus, we believe that the determined k_c is an intrinsic property of the PRGP. This k_c value exceeds the low bound of the amorphous limit (about 1~2 $Wm^{-1}K^{-1}$) [151, 152]. Such unprecedented low cross-plane thermal conductivity has been reported by Chiritescu *et al* [153]. In their work, Chiritescu reported a thermal conductivity of 0.05 $Wm^{-1}K^{-1}$ at RT for a fully dense disordered and layered thin WSe_2 film.

This value is 30 times smaller than k_c of single-crystallite WSe_2 layered structure and 6 times smaller than the predicted minimum thermal conductivity for this material. The author attributed the extremely low k_c to the localization of lattice vibrations induced by the random stacking 2D WSe_2 sheets. This may also be a reason for the low k_c in our PRGP and GOP which are also assembled by layered, disordered graphene oxide flakes.

4.2.2 Thermal diffusivity analysis

Note that, c_p is a key parameter in the calculation or fitting of k_c, as the PLTR2 technique is based on the thermal diffusivity measurement. As described before, c_p of PRGP and GOP are taken from that of graphite, while the discrepancy from graphite is unclear. Although we have performed direct DSC measurement of c_p, the available data is only at near RT. The discrepancy of c_p is mainly from different interlayer coupling strength and different chemical bonds other than the C-C sp^2 bonds in pristine graphite. The interlayer coupling strength is directly related to the interlayer spacing which will get weaker as the interlayer spacing increases. Thus, the discrepancy of the GOP from graphite may be relatively larger due to the large interlayer spacing (8.4 Å). This discrepancy is weak at high temperature as the heat capacity is mainly from the contribution of high-frequency phonons in the in-plane direction. However, as temperature decrease, the high-frequency phonons will get frozen and the long wavelength phonons with strong interlayer coupling will be more significant. Different chemical bonds other than the C-C sp^2 bonds are more likely to induce significant discrepancy in c_p. The bonding energy introduced by the other bonds like the C-O is different from that of the C-C sp^2 bonds. Moreover, the oxygen atoms attached to the C atoms will convert the C-C sp^2 bonds to sp^3 bonds. This conversion has been confirmed by Mkhoyan [154], where a 1:5 oxygen to carbon atoms ratio could lead to 40% of the sp^2 bonds into sp^3

bonds. Thus, c_p of PRGP and GOP may have significant discrepancy from those of graphite, especially for GOP with much higher oxygen component and much larger interlayer spacing.

Therefore, with the unknown discrepancy of c_p and the difference in density, the uncertainty of k_c may be large. In this case, we will mainly focus on α_c in interpreting the thermal transport in PRGP and GOP in the following sections. For GOP, α_c can be directly derived from the half rise time $t_{1/2}$, as described before. The derived α_c is shown in Fig. 4.5 (a), which varies from (1.51± 0.05) × 10^{-7} m^2/s at 295 K to (2.28 ± 0.08) × 10^{-7} m^2/s at 12.5 K. For PRGP, the measurement is performed on the multilayered PRGP/PMMA/PET/Ir film, and the thermal conductivity is first derived from the least square fitting. Then the thermal diffusivity is calculated as $k = \alpha \cdot \rho \cdot c_p$. Additional fitting processes are performed with c_p varies around the value of graphite. The results show that the fitted k_c changes proportionally to the variation of c_p. In contrast, the calculated α_c varies no larger than 10% even the deviation of c_p reaches 100%. This is, however, expected for the PLTR2 model as it is based on the thermal diffusivity measurement. Therefore, the measured thermal diffusivity has a low uncertainty and can be used to better analyze the thermal transport in the sample in this work. From Fig. 4.5 (a) we can see α_c of PRGP ranges from (1.02 ± 0.09) × 10^{-7} m^2/s at 295 K to (2.31 ±0.18) × 10^{-7} m^2/s at 12 K, showing an increasing trend as temperature decreases, like those of GOP and GP. α_c of PRGP have no significant difference for the down round and up round measurements at a given experimental temperature. This means the low temperature has negligible influence on the structure of PRGP, or at least the PRGP has no irreversible structure changes during the low-temperature process. The uncertainties in the determined α_c of PRGP and GOP come from the errors in the determination of the thicknesses and the fitting process.

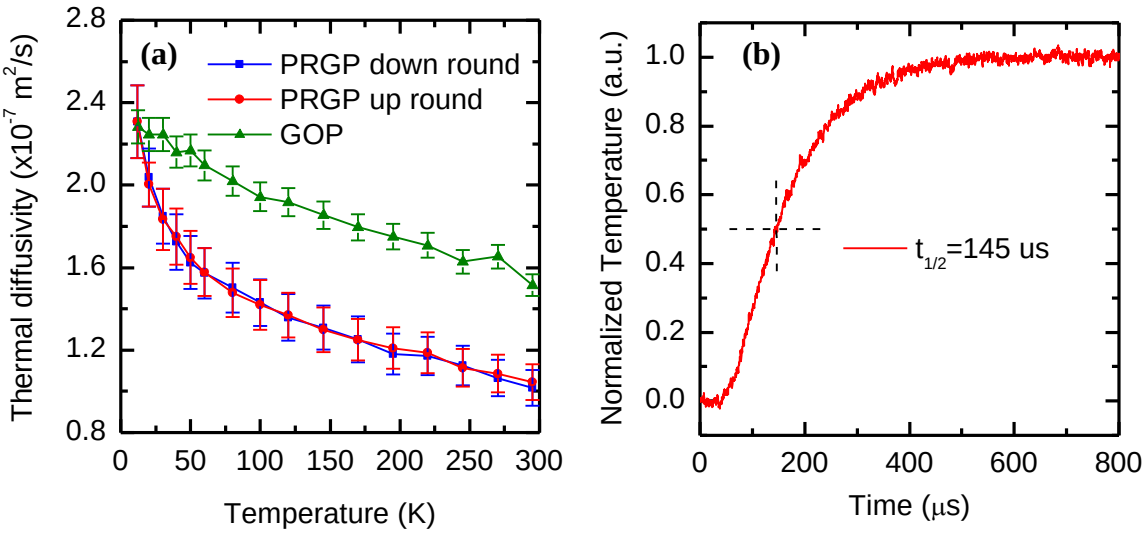

Figure 4.5 (a) *c*-axis thermal diffusivity of PRGP and GOP. (b) Classic laser flash study of PRGP at RT.

To confirm the measurement accuracy of the PLTR2 technique on the multilayered sample, the classical laser flash method is applied on PRGP at RT. In this measurement, the PRGP is suspended, with no PET or PMMA films attached, no Ir coating. The same nanosecond pulsed laser is used to heat the front surface of the sample. The temperature at the back surface is detected by an infrared detector, which is connected to a pre-amplifier and then to the oscilloscope. Figure 4.5 (b) shows the temperature evolution curve at the front surface. The half rise time is 145 μs, from which the thermal diffusivity at RT is calculated at 1.27 × 10^{-7} m^2/s according to the equation $\alpha = 1.37L^2/\pi^2 t_{1/2}$. This value is about 25% larger than that determined from the PLTR2 measurement, but still proves the measurement accuracy of the PLTR2 technique on the multilayered sample, considering some sample-to-sample structure difference. The difference may come from the uncertainty in the thicknesses of the PMMA and PET. The different environments may be another reason. Not like the PLTR2 technique, this laser flash measurement is performed in the atmosphere with no vacuum or temperature control.

In this case, the convection may also lead to errors in the results. In this classic laser flash method, the thermal diffusivity can be directly derived, without additional process of the sample or fitting of the experimental. However, the infrared detector cannot work well at very low temperatures and cannot be put into our vacuum chamber. Therefore, we developed the PLTR2 technique and performed the measurement from RT down to very low temperatures in a well temperature and vacuum controlled system to uncover the structure and thermal transport properties evolution against temperature.

4.2.3 Physical interpretation of the low thermal diffusivity

As described in Chapter 3, thermal transport in graphene-based materials are dominated by phonons from lattice vibrations and the effect of electrons is negligible [149, 155]. This also hold true for PRGP and GOP. The phonon thermal conductivity can be expressed as the following equation: [15]

$$k_p = \sum_j \int C_j(\omega) \upsilon_j^2(\omega) \tau_j(\omega) d\omega \tag{4.3}$$

For 1D thermal transport, this equation can be simplified as $k_p = C\upsilon l$, taking the average phonon group velocity (v) and phonon MFP (noted as l) for all the phonon branches. The thermal diffusivity is defined as $\alpha = k/C$, so we have $\alpha = \upsilon l$. In general, we can see that the thermal diffusivity is proportional the phonon group velocity and the phonon MFP. For PRGP, the phonon MFP is limited by phonon scattering from the defects and the grain boundaries as described in the last section. Thus, the phonon MFP should be smaller than the crystallite size. From the XRD characterization, the crystallite size is determined at 4.8 nm for PRGP in the cross-plane direction. This value is more than one order of magnificent smaller

than that of GP (234 nm) determined in Chapter 3 and is also tens of times smaller than that of graphite (at hundreds nm scale) reported in other work. [25-27] This small crystallite size will induce highly dense phonon scattering at the grain boundaries and defect spots which is the main reason for the extremely low α_c of PRGP comparing with GP or graphite.

The relatively larger interlayer spacing of PRGP (3.68 Å) comparing with GP and highly ordered graphite (3.35 Å) may be another factor that suppresses α_c of PRGP. The enlargement of interlayer spacing changes the phonon dispersion and the interlayer binding energy where the energy coupling of interlayer atoms through Van der Waals force will get weaker [156, 157]. In this case, fewer phonon modes will be activated and occupied in the thermal transport in the cross-plane direction. Besides, as the interlayer spacing gets larger, the cross-plane phonon group velocity will also be reduced and lead to the decrease of α_c, according to the equation $\alpha = \upsilon l$. The functional groups may also play a role in the reduction of α_c in PRGP. However, the interlayer spacing is 3.68 Å from the XRD results, only 10% larger than that of highly ordered graphite. This mean few atoms or oxygen-contained functional groups (mostly hydroxyl and epoxy groups) exist on the basal plane and most of the functional groups (mostly carboxylic acid and other groups like ketones) are located at the edges of the graphene sheets [62, 139]. Figure 4.6 (a) shows a schematic illustration of the layered structure of the PRGP flakes where most functional groups such as carboxylic acids or single ketones are located at the edges of the graphene sheets. The accumulated functional groups at the sheet edges may enhance the boundary scattering which will also suppress the thermal transport in the cross-plane direction. The existence of Iodine (I) atoms may be another reason. According to the EDS results, the atomic fraction of I in the PRGP is about 3.65%.

These I atoms may come from the reduction process which uses HI acid to perform the chemical reduction to produce rGO from GO. The I atom can provide significant scattering sources due to its heavy mass. Also, there may exist some vacancies and distortions in the basal plane, due to the remove of carbon atoms upon chemical reduction [59]. This kind of defects also serve as scattering sources and weakens the energy coupling in the cross-plane direction.

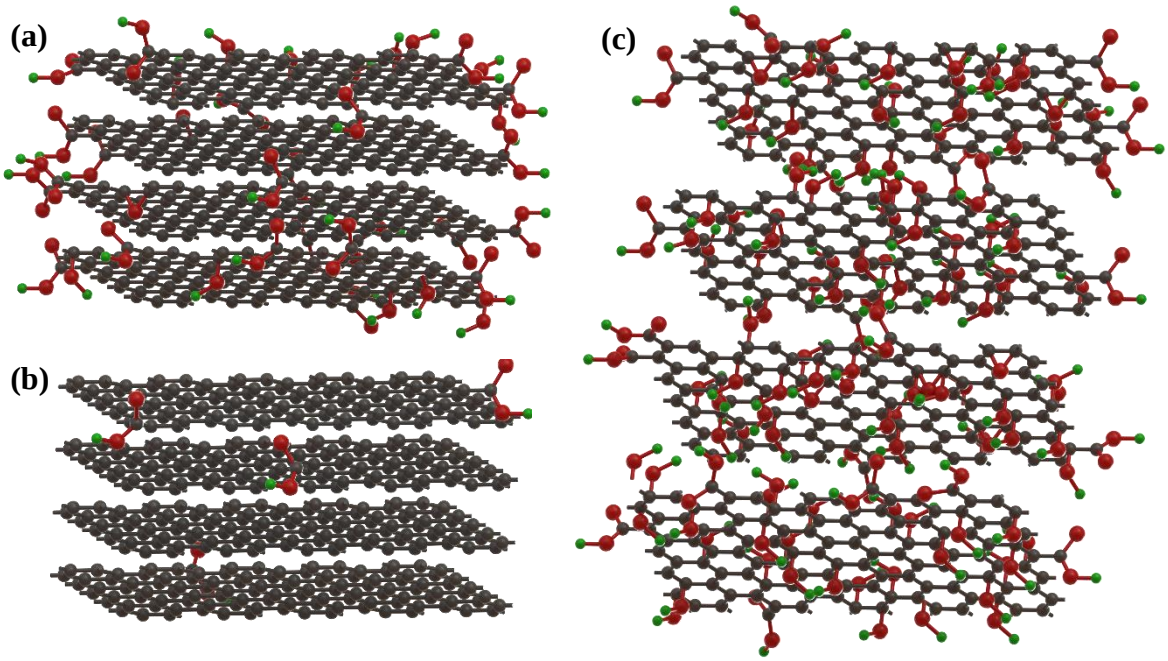

Figure 4.6 Schematic illustration of the samples (not to scale). Gray: carbon atoms; red: oxygen atoms; green: hydrogen atoms. (a) PRGP with an interlayer spacing of 3.68 Å. (b) GP with an interlayer spacing of 3.35 Å. (c) GOP with an interlayer spacing of 8.4 Å.

For GOP, α_c is also much smaller than that of GP and graphite. The crystallite size of GOP is determined at 7.1 nm from XRD, tens of times smaller than that of GP and highly ordered graphite as described before. Like in the PRGP, the small crystallite size also suppresses α_c of GOP significantly. The interlayer spacing is determined at 8.4 Å from the XRD study, much larger than that in GP, PRGP and graphite. In this case, direct energy

coupling between carbon layers through van der Waals force is reduced to a negligible level. This has been confirmed by previous studies on binding energy of graphite by Spanu *et al*. [156] and Chen *et al*. [157] In spanu's work, an *ab initio* many-body theory was used to compute the interlayer bonding properties of graphite. The results showed that the binding energy rises when interlayer spacing is larger than 3.35 Å and approaches zero when it is larger than 7 Å. Similarly, in Chen's work, the interlayer potentials and interlayer banding energy of graphite as a function of the interlayer spacing was calculated by using a modified Mobius method based on *ab initio* calculations. The results shows that when the interlayer spacing is larger than 8 Å, the interlayer potentials and the interlayer banding energy are negligible. [157] Nevertheless, α_c of GOP is comparable or even larger than that of PRGP. This means other mechanism should exist and support the thermal transport in the cross-plane direction. The existence of functional groups on the basal plane is probably one of the major reason. Not like the PRGP with smaller interlayer spacing and hold few atoms or functional groups in the basal plane, the GOP has an interlayer spacing of 8.4 Å, large enough to hold those functional groups like epoxy and hydroxyl among layers [55], and even functional chains that connect the graphene layers. The EDS study also shows that the GOP contains more Oxygen than PRGP (atomic fraction of 35.12% and 9.93% for GOP and PRGP, respectively). Previous work by Gao *et al.* [50] shows that the oxygen-contained functional groups in the basal plane are easier to remove upon chemical reduction, as expected for PRGP. Compared with PRGP, the existence of functional groups on the basal plane provides additional exfoliation energy which helps keep the PRGP stable. In other words, these functional groups or even chains can serve as weak thermal transport tunnels across the carbon layers upon the absence of direct energy coupling through van der Waals force. Figure 4.6 (c) shows a schematic illustration of the GOP

structure. Compared with Fig. 4.6 (a), we can see there are many functional groups hold on the basal plane in GOP.

For comparison, a schematic illustration of the GP structure studied in Chapter 3 is also shown in Fig. 4.6 (b), where few functional groups exist on the basal plane or at the sheet edges. From the EDS study, the atomic fraction of the existing elements in GP is carbon (99.81%), oxygen (0.19%), indicating a high purified carbon material. In addition, the XRD characterization also showed that, the interlayer spacing of GP is 3.35 Å, the same as highly ordered graphite. Thus, we believe that, GP has almost the same structure as that of highly ordered graphite, where few defects exist in the basal plane or at the edges of graphene sheet [as shown in Fig. 4.6 (b)]. The thermal transport properties of GP have also been characterized in our previous work [66] and in Chapter 3. The results show that, k_a is about 600 $Wm^{-1}K^{-1}$ at RT and switch to 3200 $Wm^{-1}K^{-1}$ at about 245 K and k_c is about 6 $Wm^{-1}K^{-1}$, close to those of highly ordered graphite. This also proves that GP is composed of highly purified and ordered graphene sheets. As a result, we can conclude that the low k_c and α_c of PRGP is due to its unique structure compared with the GP. The combined effects from the small grain size, the large interlayer spacings and the high-level defects such as functional groups, vacancies, and distortions lead to the significant reduction of α_c in PRGP. As detailed before, for GOP, a large number of functional groups are located on the basal plane, while for PRGP, the remaining functional groups are at the edges of the graphene flakes. The different locations of functional groups also have strong effects on the thermal transport properties of those graphene-based materials.

CHAPTER 5. CONCLUSION AND FUTURE WORK

5.1 Conclusion on graphene induced thermal resistance

In this work, the thermal resistance and conductance of the β-W/Gr interfaces were studied by using the PT technique. Single-layered, multilayered β-W films and multilayered β-W films sandwiched with graphene layers were deposited on the 100-nm-SiO_2/Si substrate by using the magnetron sputtering method. With a differential technology, we are able to distinguish the thermal resistance induced by the β-W films and the β-W/Gr interfaces. The crystallite size in the β-W films was determined at 11 nm from the β(200) peak at the XRD pattern. The pole-figure XRD showed that the β(200) plane is parallel to the surface of the films. The graphene samples were determined to be 1~2 layers from the ratio of the integrated G peak and 2D peak in the Raman spectra. The thermal conductivity of β-W films is very low (1.69~2.41 $Wm^{-1}K^{-1}$) compared to that of the bulk α-W (174 $Wm^{-1}K^{-1}$). This low k is mainly due to the strong electron scattering from defects. The $R_{W/W}$ was determined at (3.57 ± 2.67) $\times 10^{-9}$ Km^2W^{-1}, indicating excellent bonding and energy coupling. $R_{W/Gr}$ vary from sample to sample, which is largely due to the inconsistency in sample preparation and the unknown graphene structure damage and alternation. Taking into consideration of the uncertainties, the largest $R_{W/Gr}$ is 11.9×10^{-9} Km^2W^{-1}, corresponding to a lower bound of thermal conductance of 84 $MWm^{-2}K^{-1}$. Compared with the up-to-date reported graphene interface thermal conductance, this β-W/Gr interface thermal conductance is at the high end. The cross-plane thermal conductivity of β-W is smaller but still comparable to that in the in-plane direction derived from the four-probe measurements based on Wiedemann-Franz law.

5.2 Conclusion on cross-plane thermal conductivity of GP

By employing the PLTR2 technique, the thermal transport properties of GP in the cross-plane direction were investigated within a temperature range from 295K to 12.3K. The determined k_c is 6.08 ± 0.6 $Wm^{-1}K^{-1}$ at RT, close to the values (5.7~6.8 $Wm^{-1}K^{-1}$) of graphite along the *c*-axis. The measurement accuracy was verified by the PT technique on the same GP, which gave a value of 5.38 ± 0.54 $Wm^{-1}K^{-1}$ at RT. Taking into account the large anisotropy of phonon dispersions, we developed a model and identified the phonons and their specific heat that sustain the heat conduction in the *c*-axis. The validity of our model was verified by predicting the *c*-MFP of graphite. Our model predicted a *c*-MFP of 165 nm for ideal graphite at RT, very close to the value of 146 nm by MD modeling. For widely studied graphite samples, our model predicted a structural domain size of 375 nm, close to the 404 nm grain size calculated from the TEM images. By studying the thermal reffusivity variation against temperature, we suppressed the measurement uncertainties and calculated the *c*-MFP induced by the defect and boundary scattering at 0 K limit. This determined *c*-MFP is about 234 nm, a good estimation of the structural domain size and defect levels in our GP sample as the Umklapp phonon-phonon scattering vanishes at the 0 K limit. This structure domain size is much smaller than the in-plane one (1.68 μm), but still significantly exceeds the graphene flake thickness (1.68~2.01 nm) in our GP, uncovering quite long-range structural order among graphene flakes. By subtracting the effect of the extrinsic scattering from defects and grain boundaries, we calculated the defect-free k_c and *c*-MFP of GP with the modified kinetic theory. At RT, the defect-free k_c is 9.67 $Wm^{-1}K^{-1}$, close to 11.6 $Wm^{-1}K^{-1}$ of graphite from the recent MD simulations. The defect-free *c*-MFP is 138 nm at RT, just a little smaller than 146 nm of graphite from MD simulations, consistent with the recent accepted theory of long *c*-MFP. This

work gives a full picture of the thermal transport properties of GP which is of great importance in its industrial applications.

5.3 Conclusion on cross-plane thermal diffusivity of PRGP and GOP

In this work, the thermal transport properties of PRGP and GOP in the cross-plane direction were characterized using the PLTR2 technique. For PRGP, the measurement was taken within a cycled temperature variation, including a down-round from 295 K down to 12 K and an up-round from 12 K back to 295 K. k_c varies from 0.14 $Wm^{-1}K^{-1}$ at 295 K to 1.2 × 10^{-3} $Wm^{-1}K^{-1}$ at 12 K, with no significant difference between the two rounds. For GOP, k_c decreases from 0.16 $Wm^{-1}K^{-1}$ at 295 K down to 9.7 × 10^{-4} $Wm^{-1}K^{-1}$ at 12.5 K, very similar to those of PRGP. To eliminate the influence of heat capacity of different structures, the thermal diffusivity was further studied. In contrary to k_c, α_c of PRGP increases from (1.02 ± 0.09) × 10^{-7} m^2/s at 295 K to (2.31 ±0.18) × 10^{-7} m^2/s at 12 K. Such small α_c is mainly attributed to the small crystallite size (4.8 nm from XRD) in the cross-plane direction. The larger interlayer spacing (3.68 Å compared with 3.35Å of GP) is another reason. For GOP, α_c varies from (1.52 ± 0.05) × 10^{-7} m^2/s at 295 K to (2.28 ±0.08) × 10^{-7} m^2/s at 12.5 K, also tens of times smaller than those of GP or graphite. Different from PRGP, GOP has a much larger interlayer spacing (8.4 Å), which makes direct energy coupling between layers negligible. The high density of functional groups like hydroxyl and epoxy on the basal plane provide additional forces that hold the material stable and serve as weak thermal transport tunnels across the carbon layers. The result of this work provides fundamental guidance for graphene-based paper structure control and thermal design toward novel thermal interface applications.

5.4 Future work

The PLTR2 technique used in the current work for GP, PRGP and GOP can be extended to most other paper-like materials. Given the laser source with an 8-10 ns pulse width, our PLTR2 system works very well for samples with a thickness ranging from hundreds of nm to tens of μm, especially for samples with a thickness of 1 to 10 μm. One thing to note is that, the laser absorption depth should be much smaller than the sample thickness. For transparent materials like polymers, this issue can be resolved by adding another layer of Ir coating on the front surface of the sample. This Ir coating will absorb the laser energy and acts as heat source to the sample. With different laser sources, this method can be further extended to much thicker or thinner samples. For example, with longer laser pulse of μs scale, the measurement can be performed on bulk samples with hundred μm to several mm thicknesses. This is also the typical working range of commercial laser flash instruments. While with shorter laser pulses of ps or even fs scale, this method can be theoretically used for films with nm thickness. However, in this case, the difficulties lie in the preparation of suspended samples and in the fact that the laser absorption depth is larger than the sample thickness.

In GP study, we developed an anisotropic heat capacity model to explain the large anisotropy in the thermal conductivity of GP and graphite and the very long phonon MFP in the *c*-axis. This model can be extended to other layered structures, including transient metal dichalcogenides (like MoS_2, $MoSe_2$ and WS_2), h-BN, and black phosphorous, *et al*. Combined with the phonon dispersion and phonon distribution study through first-principle calculations or MD simulations, the different contributions of phonon modes in different directions and the anisotropic phonon group velocities can be extracted and the anisotropic phonon MFPs can be evaluated further.

In the study of PRGP and GOP, the oxygen-contained functional groups are claimed to play an important role in the thermal transport properties of these graphene-based structures. While the effect of the type and quantity of these functional groups is an interesting and challenging aspect which is worth for further and deeper study. Through modifying the graphene flakes with different chemicals, we may be able to control the formation of the functional groups and specify the type and quantity of the functional groups. This can help us better understand the influence of different functional groups on the structure change and the thermal transport properties evolution. In other aspects, we may be able to tune the thermal and electrical transport properties of graphene-based materials through these controlled chemical modifications.

REFERENCES

[1] K.S. Novoselov, A.K. Geim, S.V. Morozov, D. Jiang, Y. Zhang, S.V. Dubonos, et al., Electric field effect in atomically thin carbon films, Sci 306(5696) (2004) 666-669.

[2] F. Xia, T. Mueller, Y.-m. Lin, A. Valdes-Garcia, P. Avouris, Ultrafast graphene photodetector, Nat. Nanotechnol. 4(12) (2009) 839-843.

[3] X. Wang, L. Zhi, K. Müllen, Transparent, conductive graphene electrodes for dye-sensitized solar cells, Nano Lett. 8(1) (2008) 323-327.

[4] F. Bonaccorso, Z. Sun, T. Hasan, A. Ferrari, Graphene photonics and optoelectronics, Nat. Photon. 4(9) (2010) 611-622.

[5] D. Cohen-Tanugi, J.C. Grossman, Water desalination across nanoporous graphene, Nano Lett. 12(7) (2012) 3602-3608.

[6] F. Liu, S. Song, D. Xue, H. Zhang, Folded structured graphene paper for high performance electrode materials, Adv. Mater. 24(8) (2012) 1089-1094.

[7] J.K. Lee, K.B. Smith, C.M. Hayner, H.H. Kung, Silicon nanoparticles–graphene paper composites for Li ion battery anodes, Chem. Commun. 46(12) (2010) 2025-2027.

[8] K.M. Shahil, A.A. Balandin, Thermal properties of graphene and multilayer graphene: Applications in thermal interface materials, Solid State Commun. 152(15) (2012) 1331-1340.

[9] M.A. Worsley, P.J. Pauzauskie, T.Y. Olson, J. Biener, J.H. Satcher Jr, T.F. Baumann, Synthesis of graphene aerogel with high electrical conductivity, J. Am. Chem. Soc. 132(40) (2010) 14067-14069.

[10] A.A. Balandin, S. Ghosh, W.Z. Bao, I. Calizo, D. Teweldebrhan, F. Miao, et al., Superior thermal conductivity of single-layer graphene, Nano Lett. 8(3) (2008) 902-907.

[11] C. Wang, L. Zhang, Z. Guo, J. Xu, H. Wang, K. Zhai, et al., A novel hydrazine electrochemical sensor based on the high specific surface area graphene, Microchimica Acta 169(1-2) (2010) 1-6.

[12] H. Sun, Z. Xu, C. Gao, Multifunctional, ultra-flyweight, synergistically assembled carbon aerogels, Adv. Mater. 25(18) (2013) 2554-2560.

[13] A.A. Balandin, Thermal properties of graphene and nanostructured carbon materials, Nature materials 10(8) (2011) 569.

[14] P. Klemens, Theory of the a-plane thermal conductivity of graphite, Journal of Wide Bandgap Materials 7(4) (2000) 332-339.

[15] D.L. Nika, A.A. Balandin, Two-dimensional phonon transport in graphene, J. Phys.: Condens. Matter 24(23) (2012) 233203.

[16] S. Ghosh, D. Nika, E. Pokatilov, A. Balandin, Heat conduction in graphene: experimental study and theoretical interpretation, NJPh 11(9) (2009) 095012.

[17] R. Nicklow, N. Wakabayashi, H. Smith, Lattice dynamics of pyrolytic graphite, PhRvB 5(12) (1972) 4951.

[18] G.A. Slack, Anisotropic thermal conductivity of pyrolytic graphite, PhRv 127(3) (1962) 694.

[19] R. Taylor, The thermal conductivity of pyrolytic graphite, PMag 13(121) (1966) 157-166.

[20] F.P. Incropera, A.S. Lavine, T.L. Bergman, D.P. DeWitt, Fundamentals of heat and mass transfer, Wiley2007.

[21] T. Tanaka, H. Suzuki, The thermal diffusivity of pyrolytic graphite at high temperatures, Carbon 10(3) (1972) 253-257.

[22] Z. Wei, Z. Ni, K. Bi, M. Chen, Y. Chen, Interfacial thermal resistance in multilayer graphene structures, Phys. Lett. A 375(8) (2011) 1195-1199.

[23] M. Harb, C. von Korff Schmising, H. Enquist, A. Jurgilaitis, I. Maximov, P. Shvets, et al., The c-axis thermal conductivity of graphite film of nanometer thickness measured by time resolved X-ray diffraction, Appl. Phys. Lett. 101(23) (2012) 233108.

[24] M.M. Sadeghi, I. Jo, L. Shi, Phonon-interface scattering in multilayer graphene on an amorphous support, Proc. Natl. Acad. Sci. 110(41) (2013) 16321-16326.

[25] Z. Wei, J. Yang, W. Chen, K. Bi, D. Li, Y. Chen, Phonon mean free path of graphite along the c-axis, Appl. Phys. Lett. 104(8) (2014) 081903.

[26] Q. Fu, J. Yang, Y. Chen, D. Li, D. Xu, Experimental evidence of very long intrinsic phonon mean free path along the c-axis of graphite, Appl. Phys. Lett. 106(3) (2015) 031905.

[27] H. Zhang, X. Chen, Y.-D. Jho, A.J. Minnich, Temperature-Dependent Mean Free Path Spectra of Thermal Phonons Along the c-Axis of Graphite, Nano Lett. 16(3) (2016) 1643-1649.

[28] S. Ghosh, I. Calizo, D. Teweldebrhan, E.P. Pokatilov, D.L. Nika, A.A. Balandin, et al., Extremely high thermal conductivity of graphene: Prospects for thermal management applications in nanoelectronic circuits, Appl. Phys. Lett. 92(15) (2008) 151911.

[29] S. Ghosh, W. Bao, D.L. Nika, S. Subrina, E.P. Pokatilov, C.N. Lau, et al., Dimensional crossover of thermal transport in few-layer graphene, Nat. Mater. 9(7) (2010) 555-558.

[30] P. Klemens, D. Pedraza, Thermal conductivity of graphite in the basal plane, Carbon 32(4) (1994) 735-741.

[31] C. Faugeras, B. Faugeras, M. Orlita, M. Potemski, R.R. Nair, A. Geim, Thermal conductivity of graphene in corbino membrane geometry, ACS nano 4(4) (2010) 1889-1892.

[32] J.-U. Lee, D. Yoon, H. Kim, S.W. Lee, H. Cheong, Thermal conductivity of suspended pristine graphene measured by Raman spectroscopy, PhRvB 83(8) (2011) 081419.

[33] S. Chen, Q. Wu, C. Mishra, J. Kang, H. Zhang, K. Cho, et al., Thermal conductivity of isotopically modified graphene, Nat. Mater. 11(3) (2012) 203-207.

[34] M. Freitag, M. Steiner, Y. Martin, V. Perebeinos, Z.H. Chen, J.C. Tsang, et al., Energy Dissipation in Graphene Field-Effect Transistors, Nano Lett. 9(5) (2009) 1883-1888.

[35] Z. Chen, W. Jang, W. Bao, C. Lau, C. Dames, Thermal contact resistance between graphene and silicon dioxide, Appl. Phys. Lett. 95(16) (2009) 161910.

[36] K.F. Mak, C.H. Lui, T.F. Heinz, Measurement of the thermal conductance of the graphene/SiO2 interface, Appl. Phys. Lett. 97(22) (2010) 221904.

[37] Y.K. Koh, M.-H. Bae, D.G. Cahill, E. Pop, Heat conduction across monolayer and few-layer graphenes, Nano Lett. 10(11) (2010) 4363-4368.

[38] P.A.V. Guzman, A. Sood, M.J. Mleczko, B. Wang, H.S.P. Wong, Y. Nishi, et al., Cross Plane Thermal Conductance of Graphene-Metal Interfaces, Ieee Intersociety Conference on Thermal and Thermomechanical Phenomena in Electronic Systems (2014) 1385-1389.

[39] P.E. Hopkins, M. Baraket, E.V. Barnat, T.E. Beechem, S.P. Kearney, J.C. Duda, et al., Manipulating Thermal Conductance at Metal-Graphene Contacts via Chemical Functionalization, Nano Lett. 12(2) (2012) 590-595.

[40] K. Jagannadham, Effect of interfacial interactions on the thermal conductivity and interfacial thermal conductance in tungsten-graphene layered structure, J. Vac. Sci. Technol. A 32(5) (2014) 051101.

[41] B. Huang, Y.K. Koh, Improved topological conformity enhances heat conduction across metal contacts on transferred graphene, Carbon 105 (2016) 268-274.

[42] B. Huang, Y.K. Koh, Negligible electronic contribution to heat transfer across intrinsic metal/graphene interfaces, Advanced Materials Interfaces 4(20) (2017).

[43] Y. Gao, T. Yang, J. Xue, S. Yan, S. Zhou, Y. Wang, et al., Radiation tolerance of Cu/W multilayered nanocomposites, J. Nucl. Mater. 413(1) (2011) 11-15.

[44] L. Pentecoste, P. Brault, A.-L. Thomann, P. Desgardin, T. Lecas, T. Belhabib, et al., Low Energy and low fluence helium implantations in tungsten: Molecular dynamics simulations and experiments, J. Nucl. Mater. 470 (2016) 44-54.

[45] A. Hasegawa, M. Fukuda, K. Yabuuchi, S. Nogami, Neutron irradiation effects on the microstructural development of tungsten and tungsten alloys, J. Nucl. Mater. 471 (2016) 175-183.

[46] J.S. Bunch, S.S. Verbridge, J.S. Alden, A.M. Van Der Zande, J.M. Parpia, H.G. Craighead, et al., Impermeable atomic membranes from graphene sheets, Nano Lett. 8(8) (2008) 2458-2462.

[47] Y. Kim, J. Baek, S. Kim, S. Kim, S. Ryu, S. Jeon, et al., Radiation resistant vanadium-graphene nanolayered composite, Scientific reports 6 (2016) 24785.

[48] S. Si, W. Li, X. Zhao, M. Han, Y. Yue, W. Wu, et al., Significant Radiation Tolerance and Moderate Reduction in Thermal Transport of a Tungsten Nanofilm by Inserting Monolayer Graphene, Adv. Mater. 29(3) (2017).

[49] M. Han, P. Yuan, J. Liu, S. Si, X. Zhao, Y. Yue, et al., Interface Energy Coupling between β-tungsten Nanofilm and Few-layered Graphene, Scientific Reports 7(1) (2017) 12213.

[50] X. Gao, J. Jang, S. Nagase, Hydrazine and thermal reduction of graphene oxide: reaction mechanisms, product structures, and reaction design, J. Phys. Chem. C 114(2) (2009) 832-842.

[51] H. Chen, M.B. Müller, K.J. Gilmore, G.G. Wallace, D. Li, Mechanically strong, electrically conductive, and biocompatible graphene paper, Adv. Mater. 20(18) (2008) 3557-3561.

[52] M. Hirata, T. Gotou, S. Horiuchi, M. Fujiwara, M. Ohba, Thin-film particles of graphite oxide 1:: High-yield synthesis and flexibility of the particles, Carbon 42(14) (2004) 2929-2937.

[53] W.S. Hummers Jr, R.E. Offeman, Preparation of graphitic oxide, J. Am. Chem. Soc. 80(6) (1958) 1339-1339.

[54] H.J. Shin, K.K. Kim, A. Benayad, S.M. Yoon, H.K. Park, I.S. Jung, et al., Efficient reduction of graphite oxide by sodium borohydride and its effect on electrical conductance, Adv. Funct. Mater. 19(12) (2009) 1987-1992.

[55] C. Botas, P. Álvarez, C. Blanco, R. Santamaría, M. Granda, M.D. Gutiérrez, et al., Critical temperatures in the synthesis of graphene-like materials by thermal exfoliation–reduction of graphite oxide, Carbon 52 (2013) 476-485.

[56] D.A. Dikin, S. Stankovich, E.J. Zimney, R.D. Piner, G.H. Dommett, G. Evmenenko, et al., Preparation and characterization of graphene oxide paper, Natur 448(7152) (2007) 457.

[57] J. Xiang, L.T. Drzal, Thermal conductivity of exfoliated graphite nanoplatelet paper, Carbon 49(3) (2011) 773-778.

[58] C. Chen, Q.H. Yang, Y. Yang, W. Lv, Y. Wen, P.X. Hou, et al., Self-Assembled Free-Standing Graphite Oxide Membrane, Adv. Mater. 21(29) (2009) 3007-3011.

[59] C.-M. Chen, J.-Q. Huang, Q. Zhang, W.-Z. Gong, Q.-H. Yang, M.-Z. Wang, et al., Annealing a graphene oxide film to produce a free standing high conductive graphene film, Carbon 50(2) (2012) 659-667.

[60] I.K. Moon, J. Lee, R.S. Ruoff, H. Lee, Reduced graphene oxide by chemical graphitization, Nat. Commun. 1(6) (2010) 73.

[61] S. Pei, J. Zhao, J. Du, W. Ren, H.-M. Cheng, Direct reduction of graphene oxide films into highly conductive and flexible graphene films by hydrohalic acids, Carbon 48(15) (2010) 4466-4474.

[62] N.-J. Song, C.-M. Chen, C. Lu, Z. Liu, Q.-Q. Kong, R. Cai, Thermally reduced graphene oxide films as flexible lateral heat spreaders, J. Mater. Chem. A 2(39) (2014) 16563-16568.

[63] G. Xin, H. Sun, T. Hu, H.R. Fard, X. Sun, N. Koratkar, et al., Large-Area Freestanding Graphene Paper for Superior Thermal Management, Adv. Mater. 26(26) (2014) 4521-4526.

[64] S. Stankovich, D.A. Dikin, R.D. Piner, K.A. Kohlhaas, A. Kleinhammes, Y. Jia, et al., Synthesis of graphene-based nanosheets via chemical reduction of exfoliated graphite oxide, carbon 45(7) (2007) 1558-1565.

[65] W. Gao, L.B. Alemany, L. Ci, P.M. Ajayan, New insights into the structure and reduction of graphite oxide, Nature chemistry 1(5) (2009) 403-408.

[66] Y. Xie, P. Yuan, T. Wang, N. Hashemi, X. Wang, Switch on the high thermal conductivity of graphene paper, Nanoscale 8(40) (2016) 17581-17597.

[67] M. Aunkor, I. Mahbubul, R. Saidur, H. Metselaar, The green reduction of graphene oxide, Rsc Advances 6(33) (2016) 27807-27828.

[68] H. Wu, L.T. Drzal, Graphene nanoplatelet paper as a light-weight composite with excellent electrical and thermal conductivity and good gas barrier properties, Carbon 50(3) (2012) 1135-1145.

[69] W. Yu, H. Xie, L. Chen, J. Zhao, F. Li, Modified graphene papers with alkaline earth metal ions endowed with high heat transfer properties, Thin Solid Films 597 (2015) 77-82.

[70] H. Malekpour, K.-H. Chang, J.-C. Chen, C.-Y. Lu, D. Nika, K. Novoselov, et al., Thermal conductivity of graphene laminate, Nano Lett. 14(9) (2014) 5155-5161.

[71] J.D. Renteria, S. Ramirez, H. Malekpour, B. Alonso, A. Centeno, A. Zurutuza, et al., Strongly anisotropic thermal conductivity of free-standing reduced graphene oxide films annealed at high temperature, Adv. Funct. Mater. 25(29) (2015) 4664-4672.

[72] A. Warren, A. Nylund, I. Olefjord, Oxidation of tungsten and tungsten carbide in dry and humid atmospheres, International Journal of Refractory Metals & Hard Materials 14(5-6) (1996) 345-353.

[73] Y.G. Shen, Y.W. Mai, Structure and properties of stacking faulted A15 tungsten thin films, JMatS 36(1) (2001) 93-98.

[74] M.J. OKeefe, J.T. Grant, Phase transformation of sputter deposited tungsten thin films with A-15 structure, J. Appl. Phys. 79(12) (1996) 9134-9141.

[75] N. Radic, A. Tonejc, J. Ivkov, P. Dubcek, S. Bernstorff, Z. Medunic, Sputter-deposited amorphous-like tungsten, Surf. Coat. Tech. 180 (2004) 66-70.

[76] I.C. Noyan, T.M. Shaw, C.C. Goldsmith, Inhomogeneous strain states in sputter deposited tungsten thin films, J. Appl. Phys. 82(9) (1997) 4300-4302.

[77] J.S. Lee, J. Cho, C.Y. You, Growth and characterization of alpha and beta-phase tungsten films on various substrates, J. Vac. Sci. Technol. A 34(2) (2016) 021502.

[78] I. Djerdj, A.M. Tonejc, A. Tonejc, N. Radic, XRD line profile analysis of tungsten thin films, Vacuu 80(1-3) (2005) 151-158.

[79] Y.G. Shen, Y.W. Mai, Q.C. Zhang, D.R. McKenzie, W.D. McFall, W.E. McBride, Residual stress, microstructure, and structure of tungsten thin films deposited by magnetron sputtering, J. Appl. Phys. 87(1) (2000) 177-187.

[80] A. KOBAYASHI, J. PURIC, Microstructure and hardness of tungsten coating for high heat resistant material produced by means of gas tunnel type plasma spraying, Trans. JWRI 38(1) (2009) 57-62.

[81] A.L. Patterson, The Scherrer formula for x-ray particle size determination, PhRv 56(10) (1939) 978-982.

[82] D. Graf, F. Molitor, K. Ensslin, C. Stampfer, A. Jungen, C. Hierold, et al., Spatially resolved raman spectroscopy of single- and few-layer graphene, Nano Lett. 7(2) (2007) 238-242.

[83] X.W. Wang, Z.R. Zhong, J. Xu, Noncontact thermal characterization of multiwall carbon nanotubes, J. Appl. Phys. 97(6) (2005) 064302.

[84] X.W. Chen, Y.P. He, Y.P. Zhao, X.W. Wang, Thermophysical properties of hydrogenated vanadium-doped magnesium porous nanostructures, Nanot 21(5) (2010) 055707.

[85] T. Wang, X.W. Wang, Y.W. Zhang, L.Y. Liu, L. Xu, Y. Liu, et al., Effect of zirconium(IV) propoxide concentration on the thermophysical properties of hybrid organic-inorganic films, J. Appl. Phys. 104(1) (2008) 013528.

[86] H.P. Hu, X.W. Wang, X.F. Xu, Generalized theory of the photoacoustic effect in a multilayer material, J. Appl. Phys. 86(7) (1999) 3953-3958.

[87] C. Kittel, P. McEuen, Introduction to Solid State Physics, 8th ed.2005.

[88] D. Choi, B.C. Wang, S. Chung, X. Liu, A. Darbal, A. Wise, et al., Phase, grain structure, stress, and resistivity of sputter-deposited tungsten films, J. Vac. Sci. Technol., A 29(5) (2011) 051512.

[89] C.F. Pai, L.Q. Liu, Y. Li, H.W. Tseng, D.C. Ralph, R.A. Buhrman, Spin transfer torque devices utilizing the giant spin Hall effect of tungsten, Appl. Phys. Lett. 101(12) (2012) 122404.

[90] Q. Hao, W.Z. Chen, G. Xiao, Beta (beta) tungsten thin films: Structure, electron transport, and giant spin Hall effect, Appl. Phys. Lett. 106(18) (2015) 182403.

[91] P. Petroff, T.T. Sheng, A.K. Sinha, G.A. Rozgonyi, F.B. Alexander, Microstructure, Growth, Resistivity, and Stresses in Thin Tungsten Films Deposited by Rf Sputtering, J. Appl. Phys. 44(6) (1973) 2545-2554.

[92] N. Bowler, Y.Q. Huang, Model-based characterization of homogeneous metal plates by four-point alternating current potential drop measurements, Ieee. T. Magn. 41(6) (2005) 2102-2110.

[93] N. Bowler, Y.Q. Huang, Electrical conductivity measurement of metal plates using broadband eddy-current and four-point methods, Meas. Sci. Technol. 16(11) (2005) 2193-2200.

[94] F. Smits, Measurement of sheet resistivities with the four-point probe, BELL. SYST. TECH. J. 37(3) (1958) 711-718.

[95] K. Fuchs, The conductivity of thin metallic films according to the electron theory of metals, Proceedings of the Cambridge Philosophical Society 34 (1938) 100-108.

[96] E.H. Sondheimer, The Mean Free Path of Electrons in Metals, AdPhy 1(1) (1952) 1-42.

[97] A.F. Mayadas, M. Shatzkes, J.F. Janak, Electrical Resistivity Model for Polycrystalline Films - Case of Specular Reflection at External Surfaces, Appl. Phys. Lett. 14(11) (1969) 345-347.

[98] A.F. Mayadas, M. Shatzkes, Electrical-Resistivity Model for Polycrystalline Films - Case of Arbitrary Reflection at External Surfaces, Phys. Rev. B 1(4) (1970) 1382-1389.

[99] S. Yoneoka, J. Lee, M. Liger, G. Yama, T. Kodama, M. Gunji, et al., Electrical and thermal conduction in atomic layer deposition nanobridges down to 7 nm thickness, Nano Lett. 12(2) (2012) 683-686.

[100] Q. Zhang, B. Cao, X. Zhang, M. Fujii, K. Takahashi, Influence of grain boundary scattering on the electrical and thermal conductivities of polycrystalline gold nanofilms, PhRvB 74(13) (2006) 134109.

[101] H.-D. Wang, J.-H. Liu, X. Zhang, Z.-Y. Guo, K. Takahashi, Experimental study on the influences of grain boundary scattering on the charge and heat transport in gold and platinum nanofilms, Heat Mass Transfer. 47(8) (2011) 893-898.

[102] M. Ou, T. Yang, S. Harutyunyan, Y. Chen, C. Chen, S. Lai, Electrical and thermal transport in single nickel nanowire, Appl. Phys. Lett. 92(6) (2008) 063101.

[103] H. Lin, S. Xu, X.W. Wang, N. Mei, Thermal and Electrical Conduction in Ultrathin Metallic Films: 7 nm down to Sub-Nanometer Thickness, Small 9(15) (2013) 2585-2594.

[104] C.Y. Ho, R.W. Powell, P.E. Liley, Thermal conductivity of the elements, J. Phys. Chem. Ref. Data 1(2) (1972) 279-421.

[105] Y.N. Yue, J.C. Zhang, X.W. Wang, Micro/Nanoscale Spatial Resolution Temperature Probing for the Interfacial Thermal Characterization of Epitaxial Graphene on 4H-SiC, Small 7(23) (2011) 3324-3333.

[106] W. Parker, R. Jenkins, C. Butler, G. Abbott, Flash method of determining thermal diffusivity, heat capacity, and thermal conductivity, J. Appl. Phys. 32(9) (1961) 1679-1684.

[107] S. Min, J. Blumm, A. Lindemann, A new laser flash system for measurement of the thermophysical properties, Thermochim. Acta 455(1) (2007) 46-49.

[108] W. Hohenauer, L. Vozár, An Estimation of thermophysical properties of layered materials by the laser-flash method, High Temperatures-High Pressures 33(1) (2001) 17-26.

[109] J. Guo, X. Wang, D.B. Geohegan, G. Eres, C. Vincent, Development of pulsed laser-assisted thermal relaxation technique for thermal characterization of microscale wires, J. Appl. Phys. 103(11) (2008) 113505.

[110] W. Yu, G. Liu, J. Wang, X. Huang, H. Xie, X. Wang, Significantly reduced anisotropic phonon thermal transport in graphene oxide films, Synth. React. Inorg. M. 43(9) (2013) 1197-1205.

[111] X. Feng, G. Liu, S. Xu, H. Lin, X. Wang, 3-dimensional anisotropic thermal transport in microscale poly (3-hexylthiophene) thin films, Poly 54(7) (2013) 1887-1895.

[112] T.A. Pham, J.S. Kim, J.S. Kim, Y.T. Jeong, One-step reduction of graphene oxide with L-glutathione, Colloid Surf., A: Physicochem. Eng. Aspects 384(1) (2011) 543-548.

[113] X. Wang, Y.P. Chen, D.D. Nolte, Strong anomalous optical dispersion of graphene: complex refractive index measured by Picometrology, Opt. Express 16(26) (2008) 22105-22112.

[114] H.J. Lee, Thermal Diffusivity in Layered and Dispersed Composites, Purdue University, Lafayette, 1975.

[115] T. Lee, Thermal Diffusivity of Dispersed and Layered Composites Purdue University, Lafayette, 1977.

[116] T.P. Melia, Thermodynamic Functions of Linear High Polymers .8. Methylmethacrylate and Polymethylmethacrylate, Poly 3(3) (1962) 317-318.

[117] T. Barron, G.K. White, Heat capacity and thermal expansion at low temperatures, Springer Science & Business Media2012.

[118] W. DeSorbo, W. Tyler, The specific heat of graphite from 13 to 300 K, J. Chem. Phys. 21(10) (1953) 1660-1663.

[119] C.L. Choy, Thermal-Conductivity of Polymers, Poly 18(10) (1977) 984-1004.

[120] C. Choy, D. Greig, The low temperature thermal conductivity of isotropic and oriented polymers, Journal of Physics C: Solid State Physics 10(2) (1977) 169.

[121] C.Y. Ho, R.W. Powell, P.E. Liley, Thermal conductivity of the elements: a comprehensive review, DTIC Document, 1974.

[122] M. Shen, P.K. Schelling, P. Keblinski, Heat transfer mechanism across few-layer graphene by molecular dynamics, PhRvB 88(4) (2013) 045444.

[123] W. Jang, Z. Chen, W. Bao, C.N. Lau, C. Dames, Thickness-dependent thermal conductivity of encased graphene and ultrathin graphite, Nano Lett. 10(10) (2010) 3909-3913.

[124] A. Al Taleb, D. Farías, Phonon dynamics of graphene on metals, J. Phys.: Condens. Matter 28(10) (2016) 103005.

[125] A. Politano, Spectroscopic investigations of phonons in epitaxial graphene, Crit. Rev. Solid State Mater. Sci. 42(2) (2017) 99-128.

[126] J.-A. Yan, W. Ruan, M. Chou, Phonon dispersions and vibrational properties of monolayer, bilayer, and trilayer graphene: Density-functional perturbation theory, PhRvB 77(12) (2008) 125401.

[127] C.T. Nai, H. Xu, S.J. Tan, K.P. Loh, Analyzing Dirac Cone and Phonon Dispersion in Highly Oriented Nanocrystalline Graphene, ACS nano 10(1) (2015) 1681-1689.

[128] A. Politano, A.R. Marino, G. Chiarello, Phonon dispersion of quasi-freestanding graphene on Pt (111), J. Phys.: Condens. Matter 24(10) (2012) 104025.

[129] A. Politano, A.R. Marino, D. Campi, D. Farías, R. Miranda, G. Chiarello, Elastic properties of a macroscopic graphene sample from phonon dispersion measurements, Carbon 50(13) (2012) 4903-4910.

[130] A. Allard, L. Wirtz, Graphene on metallic substrates: suppression of the Kohn anomalies in the phonon dispersion, Nano Lett. 10(11) (2010) 4335-4340.

[131] P. Anees, M. Valsakumar, S. Chandra, B. Panigrahi, Ab initio study on stacking sequences, free energy, dynamical stability and potential energy surfaces of graphite structures, Modell. Simul. Mater. Sci. Eng. 22(3) (2014) 035016.

[132] N. Mounet, N. Marzari, First-principles determination of the structural, vibrational and thermodynamic properties of diamond, graphite, and derivatives, PhRvB 71(20) (2005) 205214.

[133] L. Wirtz, A. Rubio, The phonon dispersion of graphite revisited, Solid State Commun. 131(3) (2004) 141-152.

[134] M. Holland, Analysis of lattice thermal conductivity, PhRv 132(6) (1963) 2461.

[135] Z. Xu, X. Wang, H. Xie, Promoted electron transport and sustained phonon transport by DNA down to 10 K, Poly 55(24) (2014) 6373-6380.

[136] Y. Xie, Z. Xu, S. Xu, Z. Cheng, N. Hashemi, C. Deng, et al., The defect level and ideal thermal conductivity of graphene uncovered by residual thermal reffusivity at the 0 K limit, Nanoscale 7(22) (2015) 10101-10110.

[137] J. Liu, Z. Xu, Z. Cheng, S. Xu, X. Wang, Thermal Conductivity of Ultrahigh Molecular Weight Polyethylene Crystal: Defect Effect Uncovered by 0 K Limit Phonon Diffusion, ACS Appl. Mater. Interfaces 7(49) (2015) 27279-27288.

[138] A. Minnich, Exploring the Extremes of Heat Conduction in Anisotropic Materials, NANOSC MICROSC THERM 20(1) (2016) 1-21.

[139] C. Vallés, J.D. Núñez, A.M. Benito, W.K. Maser, Flexible conductive graphene paper obtained by direct and gentle annealing of graphene oxide paper, Carbon 50(3) (2012) 835-844.

[140] S. Park, J. An, J.R. Potts, A. Velamakanni, S. Murali, R.S. Ruoff, Hydrazine-reduction of graphite-and graphene oxide, Carbon 49(9) (2011) 3019-3023.

[141] F.T. Johra, J.-W. Lee, W.-G. Jung, Facile and safe graphene preparation on solution based platform, Journal of Industrial and Engineering Chemistry 20(5) (2014) 2883-2887.

[142] F. Tuinstra, J.L. Koenig, Raman spectrum of graphite, J. Chem. Phys. 53(3) (1970) 1126-1130.

[143] B. Gurzęda, P. Florczak, M. Wiesner, M. Kempiński, S. Jurga, P. Krawczyk, Graphene material prepared by thermal reduction of the electrochemically synthesized graphite oxide, RSC Advances 6(67) (2016) 63058-63063.

[144] C.-M. Chen, Q. Zhang, M.-G. Yang, C.-H. Huang, Y.-G. Yang, M.-Z. Wang, Structural evolution during annealing of thermally reduced graphene nanosheets for application in supercapacitors, Carbon 50(10) (2012) 3572-3584.

[145] A.C. Ferrari, J. Meyer, V. Scardaci, C. Casiraghi, M. Lazzeri, F. Mauri, et al., Raman spectrum of graphene and graphene layers, Phys. Rev. Lett. 97(18) (2006) 187401.

[146] M. Han, J. Liu, Y. Xie, X. Wang, Sub-μm c-axis structural domain size of graphene paper uncovered by low-momentum phonon scattering, Carbon 126 (2018) 532-543.

[147] G. Naik, S. Krishnaswamy, Photoreduction and Thermal Properties of Graphene-Based Flexible Films, Graphene 6(02) (2017) 27.

[148] N.K. Mahanta, A.R. Abramson, Thermal conductivity of graphene and graphene oxide nanoplatelets, Thermal and Thermomechanical Phenomena in Electronic Systems (ITherm), 2012 13th IEEE Intersociety Conference on, IEEE, San Diego, 2012, pp. 1-6.

[149] E. Pop, V. Varshney, A.K. Roy, Thermal properties of graphene: Fundamentals and applications, MRS Bull. 37(12) (2012) 1273-1281.

[150] R.O. Pohl, X. Liu, E. Thompson, Low-temperature thermal conductivity and acoustic attenuation in amorphous solids, RvMP 74(4) (2002) 991-1013.

[151] D.G. Cahill, S.K. Watson, R.O. Pohl, Lower limit to the thermal conductivity of disordered crystals, PhRvB 46(10) (1992) 6131.

[152] A.J. Bullen, K.E. O'Hara, D.G. Cahill, O. Monteiro, A. von Keudell, Thermal conductivity of amorphous carbon thin films, J. Appl. Phys. 88(11) (2000) 6317-6320.

[153] C. Chiritescu, D.G. Cahill, N. Nguyen, D. Johnson, A. Bodapati, P. Keblinski, et al., Ultralow thermal conductivity in disordered, layered WSe2 crystals, Sci 315(5810) (2007) 351-353.

[154] K.A. Mkhoyan, A.W. Contryman, J. Silcox, D.A. Stewart, G. Eda, C. Mattevi, et al., Atomic and electronic structure of graphene-oxide, Nano Lett. 9(3) (2009) 1058-1063.

[155] T. Nihira, T. Iwata, Temperature dependence of lattice vibrations and analysis of the specific heat of graphite, PhRvB 68(13) (2003) 134305.

[156] L. Spanu, S. Sorella, G. Galli, Nature and strength of interlayer binding in graphite, Phys. Rev. Lett. 103(19) (2009) 196401.

[157] X. Chen, F. Tian, C. Persson, W. Duan, N.-x. Chen, Interlayer interactions in graphites, Sci. Rep. 3 (2013) 3046.